



**The effect of microstructure on the susceptibility of pipeline steels to environment-assisted cracking**

By

Alhaji Mustapha, MSc (N'cle)

A thesis submitted for the degree of Doctor of Philosophy

School of Chemical Engineering and Advanced Materials

Newcastle University

2010

## **PREFACE**

This thesis describes original work that has not been submitted for a degree in any university. The investigation was performed in the corrosion laboratories, Herschel Building, School of Chemical Engineering and Advanced Materials, Newcastle University during the period from October 2006 to October 2010, under the supervision of Dr. E. A. Charles with guidance from Prof. D. Hardie.

## **ACKNOWLEDGEMENTS**

I thank God for granting me the will to produce this work.

My gratitude also goes to my supervisor, Dr. E. A. Charles and to Prof. D. Hardie for introducing me to the field of steel microstructure.

I am also grateful to Newcastle University, my sponsor PTDF – Nigeria, technical staff of the Advanced Materials group and to my colleagues.

## ABSTRACT

Little has been reported regarding the susceptibility of grade X100 pipeline steel to environment-assisted cracking (EAC). The relative susceptibility of as-received bulk, welded and simulated heat-affected zone (HAZ) microstructures were compared using slow strain rate techniques and smooth tensile specimens. The susceptibility was also compared with that of X80 steel. Specimens were tested in a 1M sodium hydrogen carbonate / 0.5M sodium carbonate solution with a pH of ~ 9.5 at a temperature of 75°C within an applied potential range of – 500 to – 1100 mV (sce). For comparison a 4M NaNO<sub>3</sub> environment was also used.

The as-received bulk grade X100 was found to be less susceptible than a Widmanstätten microstructure, or a pearlite/ferrite, or a “spheroidised” structure. Welding has a significant effect on the microstructure and hence resistance to EAC. Tests on the as-received steel gave serrated load-extension curves and the serrations occur at particular combinations of strain rate and temperature. The serrations at 75°C and strain rate of  $2 \times 10^{-6}$ /s were removed by annealing at 600°C but this increases the susceptibility to secondary cracking at potentials more negative than – 800 mV (sce). The grade X100 is less susceptible to stress corrosion cracking (SCC) than to hydrogen embrittlement.

The role of carbon and manganese solute atoms in microstructural segregation (banding) was investigated. Banding induced directionality in the growth of stress corrosion cracks and caused fracture surface ovality. EDX microanalysis confirmed that the concentration of manganese is higher in the bands of pearlite. Band removal depends on homogenisation of either carbon or manganese which also depends on temperature, time and diffusion rate. Carbon diffusion may be restricted by cooling austenitised steel at a fast rate. Rapid cooling removes carbon segregation but does not remove manganese segregation. Homogenisation of manganese at 1175°C takes more than five hours.

# CONTENTS

PREFACE.....	I
ACKNOWLEDGEMENTS.....	II
ABSTRACT .....	III
CONTENTS .....	IV
LIST OF FIGURES.....	VII
LIST OF TABLES .....	XIV
Chapter 1 : INTRODUCTION .....	1
Chapter 2 : LITERATURE REVIEW.....	3
2.1 Steel.....	3
2.1.1 Steel manufacture .....	3
2.1.1.1 Pipeline steel manufacture .....	5
2.1.2 Fabrication of pipe.....	8
2.1.2.1 Welding of pipeline .....	8
2.1.2.2 Weld heat affected zone (HAZ) .....	11
2.1.3 Metal crystal structures.....	12
2.1.4 Diffusion .....	14
2.1.5 Dislocation .....	14
2.1.6 The iron-carbon phase diagram.....	15
2.1.6.1 Solubility of carbon and manganese in ferrite and austenite iron .....	18
2.1.7 Strengthening mechanisms in metals .....	18
2.2 As-received pipeline steel.....	20
2.2.1 Development in pipeline steel production .....	23
2.2.2 Development of X100 steel .....	24
2.3 Properties of pipeline steel.....	25
2.3.1 Strength.....	25
2.3.2 Toughness .....	27
2.3.3 Weldability.....	28
2.4 Banding.....	30
2.4.1 Effect of banding on mechanical properties of steel .....	32
2.4.2 Effect of banding on crack propagation.....	32
2.4.3 Removal of banding .....	32
2.5 Environment-assisted cracking .....	33
2.5.1 EAC tests types .....	38
2.5.1.1 Static loading of smooth specimen constant-load and constant-strain tests.....	39

2.5.1.2 Static loading of pre-cracked (fracture mechanics) specimens .....	39
2.5.1.3 Slow strain rate testing .....	42
2.5.2 Mechanisms of EAC.....	45
2.5.3 Effect of microstructure on EAC .....	48
Chapter 3 : EXPERIMENTAL.....	52
3.1 Material specifications .....	52
3.1.1 Chemical compositions and mechanical properties .....	52
3.1.2 Microstructures of the as-received steels.....	52
3.1.2.1 Microstructure of as-received seam-weld heat-affected zone (HAZ) .....	55
3.1.2.2 Grain size and crack frequency measurement.....	55
3.2 Hardness measurement .....	56
3.3 Cracking environment .....	57
3.3.1 Test solutions .....	57
3.3.2 Applied potential .....	57
3.4 Electrochemical test .....	58
3.5 Heat treatment.....	58
3.5.1 Heating of rectangular bars .....	59
3.5.2 Heat treatment of blocks and rods.....	59
3.5.4 Estimation of transformation temperature .....	61
3.5.5 Estimation of time to remove banding .....	62
3.6 Slow strain rate testing .....	63
3.6.1 Interrupted SSRT.....	64
3.6.2 Metallography .....	65
3.6.3 Ductility measurement.....	66
3.6.4 SSRT data analysis .....	67
3.7 Fractography .....	68
3.7.1 Elemental analysis .....	70
3.8 Film morphology test .....	70
3.8.1 X-ray diffraction.....	70
Chapter 4 : RESULTS.....	73
4.1 Heat treatment.....	73
4.1.1 Grade X65 pipeline steel.....	74
4.1.1.1 Band removal through carbon diffusion .....	77
4.1.1.2 Band removal through manganese diffusion.....	77
4.1.2 Grade X80 and X100.....	80
4.1.2.1 Seam-weld HAZ microstructures .....	84

4.2 Slow strain rate testing .....	85
4.2.1 Electrochemical tests .....	85
4.2.2 SSRT in the carbonate solution for the as-received X100.....	85
4.2.2.1 Types of film associated with the SCC of the grade X100.....	86
4.2.3 Susceptibility of the as-received and heat treated X100 compared.....	86
4.2.4 Effect of serrations on the grade X100 steel .....	105
4.2.5 Susceptibility of the as-received X80 and X100.....	111
4.2.6 Susceptibility of the as-received X80 and its HAZ.....	111
4.2.7 SSRT in sodium nitrate.....	112
Chapter 5 : DISCUSSION.....	117
5.1 Introduction.....	117
5.2 Effect of potential on susceptibility to cracking .....	118
5.3 Effect of microstructure on susceptibility to IG SCC .....	121
5.4 Susceptibility of grade X80 compared with that of X100.....	122
5.5 Effect of carbon and manganese on banding .....	122
5.6 Effect of heat treatment on banding .....	123
5.7 Effect of banding on ductility .....	126
5.8 Effect of banding on stress corrosion cracking.....	127
Chapter 6 : CONCLUSIONS .....	129
FURTHER WORK.....	131
REFERENCES: .....	132

## LIST OF FIGURES

Figure 2-1. Basic oxygen steel-making: primary and secondary processing <sup>15</sup> .....	6
Figure 2-2. Steelmaking technologies to meet property requirements for pipeline steel <sup>16</sup> .....	7
Figure 2-3. Initial stages of pipe production <sup>17</sup> .....	9
Figure 2-4. The final stages: U-O-E process <sup>15</sup> .....	9
Figure 2-5. Schematic of a submerged-arc welding (from: <a href="http://www.twi.co.uk/content/jk5.html">www.twi.co.uk/content/jk5.html</a> , browse on the 30/09/10).....	11
Figure 2-6. Schematic demonstration of HAZ showing regions of banded and non-banded microstructure <sup>11</sup> .....	12
Figure 2-7. Fourteen crystal (Bravais) lattices, the dots indicate the atom positions <sup>19</sup> .....	13
Figure 2-8. Iron-carbon phase diagram <sup>10</sup> .....	16
Figure 2-9. Developments in pipeline steels production <sup>23</sup> .....	24
Figure 2-10. Relationship between 50% transformation temperature and tensile strength of continuously cooled steels <sup>27</sup> .....	26
Figure 2-11. Application of strengthening mechanism to pipeline steels <sup>15</sup> .....	27
Figure 2-12. Micrograph showing bands of pearlite (dark) and ferrite (light) in as-received X65 pipeline steel. Average band centre to centre (c/c) spacing is 19 $\mu\text{m}$ .....	30
Figure 2-13. Schematic showing modes of corrosion including transgranular and intergranular cracking <sup>52</sup> .....	36
Figure 2-14. A compact tension specimen. Also referred to as single edge notch tension (SENT) specimen <sup>60</sup> .....	40
Figure 2-15. Precracked double beam specimen. Also referred to as double cantilever beam (DCB) specimen <sup>60</sup> .....	40
Figure 2-16. single-edge notched beam (SENB) specimen <sup>60</sup> .....	41
Figure 2-17. Effect of strain rate upon the stress corrosion susceptibility of a pipeline steel at 79°C 1M NaHCO <sub>3</sub> /0.5M Na <sub>2</sub> CO <sub>3</sub> solution (Tensile test on plain specimen) <sup>62, 64, 65</sup> .....	43
Figure 2-18. Slow strain rate stress corrosion test results for pipeline steel in 1M NaHCO <sub>3</sub> /0.5M Na <sub>2</sub> CO <sub>3</sub> solution at 75°C and various potentials. Increasing susceptibility to stress corrosion is associated with decreasing reduction in area <sup>5</sup> ...	44



Figure 2-19. Stress corrosion crack velocities from slow strain rate tests on X52 grade pipeline steel in 1M NaHCO <sub>3</sub> /0.5M Na <sub>2</sub> CO <sub>3</sub> solution, with and without Na <sub>2</sub> CrO <sub>4</sub> additions, at 75°C and various potentials <sup>5</sup> .....	44
Figure 2-20. Schematic comparison of (a) anodic SCC and (b) hydrogen embrittlement cracking (HEC) mechanism <sup>56</sup> .....	48
Figure 3-1. Microstructure of grade X65 steel viewed in three dimensions, 360x ....	54
Figure 3-2. Microstructure of grade X80 steel viewed in three dimensions, 360x ....	54
Figure 3-3. Microstructure of grade X100 steel viewed in three dimensions, 360x ..	54
Figure 3-4. Seam-weld and HAZ of a grade X80 pipeline steel .....	55
Figure 3-5. Seam-weld and HAZ of a grade X100 pipeline steel .....	55
Figure 3-6. Schematic of Vickers hardness test method.....	56
Figure 3-7. Schematic representation of the tube furnace used in heat treatment of specimens <sup>88</sup> .....	60
Figure 3-8. Air-cooling curve for 10 mm cube grade X65 steel after 20min at 1000°C .....	61
Figure 3-9. Variation of upper transformation temperature (Ar <sub>3</sub> ) with manganese concentration for 0.1% carbon steel <sup>89</sup> .....	61
Figure 3-10. Estimated minimum time required to remove banding in grade X65 pipeline steel with an average pearlite centre to centre spacing of 19 µm. Note: banding due to carbon segregation is removed in approximately five seconds at 900°C.....	62
Figure 3-11. Slow strain rate testing machine <sup>7</sup> .....	63
Figure 3-12. SSRT specimen, length 90 mm .....	64
Figure 3-13. Cross-section of a fractured specimen polished for crack measurement, 1.5x.....	65
Figure 3-14. SSRT load-time plot of a test conducted on as-received grade X100 pipeline steel in the carbonate solution at 75°C and an applied potential of – 850 mV (sce).....	65
Figure 3-15. % Elongation measured from chart compared with that from the specimen.....	67
Figure 3-16. Schematic of the parts of a scanning electron microscope <sup>94</sup> .....	69
Figure 4-1. Elongated ferrite grains deflect growth of an IG crack in grade X100 steel .....	73

Figure 4-2. Twenty minute line scan showing variation of manganese and silicon across bands of pearlite and ferrite .....	74
Figure 4-3. Micrograph showing longitudinal section through a pipe wall of a heat treated (furnace cooled after 20min. at 1000°C) grade X65 pipeline steel. Pearlite and ferrite etched dark and white, respectively .....	76
Figure 4-4. Micrograph showing the positions of the area and spot analyses, 670x ..	76
Figure 4-5. Energy-dispersive X-ray spectrum by spot analysis for a pearlite band of the heat-treated (furnace cooled after 20 minutes at 1000°C) grade X65 pipeline steel .....	78
Figure 4-6. Elemental mapping showing the difference in the concentration of Mn in the band of pearlite and ferrite,.....	78
Figure 4-7. Effect of heat treatment on average hardness and banding in the ‘LT’ face for the grade X65 pipeline steel. Heating time for each heat treatment was 20 minutes .....	79
Figure 4-8. Effect of soak time on the average centre-to-centre spacing of pearlite bands in the ‘LT’ face of grade X65 steel; the mode of cooling applied is furnace cooling.....	79
Figure 4-9. Microstructure of a heated bar of grade X65 steel, images 1150x .....	80
Figure 4-10. Mid-section hardness of the ‘CT’ face across the seam-weld and HAZ for grades X80 and X100 pipeline steel.....	82
Figure 4-11. Mechanical properties of simulated HAZ of grade X100 line pipe steel. The proof stress and the ductility were measured in silicone oil at 75°C. Average hardness measured from the ‘LT’ face at room temperature .....	83
Figure 4-12. The interface boundary (encircled region) for weld and parent metal ..	87
Figure 4-13. Widmanstätten structure at 5.3 mm from the centre of grade X100 steel seam weld (Figure 4-10) .....	87
Figure 4-14. Microstructure formed at 6 mm from the centre of the grade X100 steel seam weld .....	88
Figure 4-15. Microstructure formed at 8 mm from the centre of the grade X100 steel seam weld .....	88
Figure 4-16. Microstructure formed at 10 mm from the centre of the grade X100 steel seam weld .....	89
Figure 4-17. Microstructure formed at 12 mm from the centre of the grade X100 steel seam weld .....	89

Figure 4-18. Fast and slow sweep rate potentiodynamic polarisation curves for as-received grade X100 steel in carbonate environment at 75°C. ....	90
Figure 4-19. Variation of average secondary crack velocity with potential for the as-received grade X100 in carbonate environment at 75°C.....	90
Figure 4-20. IG cracks in as-received X100 pipeline steel tested in the carbonate solution at an applied potential of – 650 mV and at 75°C. Prior to testing specimen was held for 24h at – 500 mV (sce).....	91
Figure 4-21. TG cracks in as-received X100 pipeline steel tested in the carbonate solution at an applied potential of – 720 mV and at 75°C .....	91
Figure 4-22. Variation of embrittlement index (using % elongation) with potential for the as-received grade X100 steel in the carbonate solution at 75°C.....	93
Figure 4-23. Simulated microstructures in specimens air cooled after 20 minutes at: (a) 1000°C and (b) 1175°C .....	94
Figure 4-24. Variation of average secondary crack velocity with potential for the as-received and heat-treated grade X100 pipeline steel in the carbonate solution at 75°C.....	96
Figure 4-25. Effect of heat treatment on average secondary crack velocity and grain size of grade X100 pipeline steel in carbonate solution at 75°C and a potential of – 600 mV (sce) .....	96
Figure 4-26. Variation of average secondary and primary crack velocities with potential for the heat treated (air cooled after 20min at 1175°C) grade X100 pipeline steel in the carbonate solution at 75°C.....	97
Figure 4-27. IG crack on the fracture surface of the heat treated (air cooled after 20min at 1175°C) grade X100 pipeline steel tested in the carbonate solution at 75°C and an applied potential of – 600 mV.....	98
Figure 4-28. TG crack on the fracture surface of the heat treated (air cooled after 20min at 1175°C) grade X100 pipeline steel tested in the carbonate solution at 75°C and applied potential of – 700 mV.....	98
Figure 4-29. Shallow TG secondary cracks in the heat treated (air cooled after 20min at 1175°C) grade X100 pipeline steel tested in the carbonate solution at 75°C and an applied potential of – 650 mV. ....	99
Figure 4-30. TG secondary cracks in the heat-treated (air cooled after 20min at 1175°C) grade X100 steel in the carbonate solution at 75°C and an applied potential	

of – 650 mV. Test held for two days at a load just before UTS and then loaded to fracture. ....	99
Figure 4-31. Variation of embrittlement index (using % elongation) with potential for the grade X100 pipeline steel in the carbonate solution at 75°C .....	100
Figure 4-32. Variation of embrittlement index (using % reduction in area) with potential for the grade X100 pipeline steel .....	100
Figure 4-33. Variation of % elongation ratio (solution : silicone oil) with potential for the grade X100 steel .....	101
Figure 4-34. Variation of % reduction in area ratio (solution : silicone oil) with potential for the grade X 100 steel.....	101
Figure 4-35. Effect of heat treatment on fracture surface ovality .....	102
Figure 4-36. Fracture surface of an as-received grade X100 specimen tested in the carbonate solution at 75°C and at an applied potential of – 720 mV (sce) .....	103
Figure 4-37. A typical ‘LT’ face microstructure before loading .....	103
Figure 4-38. A typical ‘CT’ face microstructure before loading.....	103
Figure 4-39. Secondary cracks in the ‘CL’ face of the as-received X100 pipeline steel specimen tested in the carbonate solution at 75°C and an applied potential of -720 mV (sce).....	104
Figure 4-40. Secondary cracks in the ‘CT’ face of the as-received X100 pipeline steel specimen tested in the carbonate solution at 75°C and an applied potential of -720 mV (sce).....	104
Figure 4-41. Variation of % elongation with potential for the grade X100.....	106
Figure 4-42. Variation of fracture stress with potential for the grade X100 steel ....	106
Figure 4-43. Variation of load (N, in Newton) drop due to serrations with test temperature. All tests in the carbonate solution were at an applied potential of – 900 mV (sce).....	108
Figure 4-44. Effect of strain rate on load drop due to serrations for tests in the carbonate solution at 75°C and an applied potential of – 900 mV (sce).....	108
Figure 4-45. ‘LT’ face microstructure of a grade X100 specimen air cooled after 30 min. at 600°C .....	109
Figure 4-46. ‘LT’ face microstructure of grade X100 specimen air cooled after 30 min at 700°C .....	109
Figure 4-47. Crack velocities of the as-received grade X100 compared with that of specimens air cooled after 30min at 600°C .....	110

Figure 4-48. Variation of embrittlement index (% elongation) with potential of the as-received grade X100 compared with that of specimens air cooled after 30min at 600°C.....	110
Figure 4-49. Variation of primary and secondary crack velocities with potential for the heat treated (air cooled after 30min at 600°C) grade X100 pipeline steel in the carbonate solution at 75°C.....	111
Figure 4-50. Crack velocities of the as-received X80 and X100.....	113
Figure 4-51. Variation of embrittlement index (% elongation) with potential for the as-received X80 and X100 .....	113
Figure 4-52. Variation of embrittlement index (% reduction in area) with potential for the as-received X80 and X100 .....	114
Figure 4-53. Crack velocities of as-received grade X80 compared with that of its seam-weld HAZ.....	114
Figure 4-54. Variation of embrittlement index (% reduction in area) with potential for the as-received grade X80 compared with its seam-weld HAZ.....	115
Figure 4-55. IG secondary cracks in an as-received grade X100 steel tested in 4 M sodium nitrate solution with 1 % $K_2Cr_2O_7$ at 75°C and an applied potential of – 350 mV (sce) .....	115
Figure 4-56. Variation of embrittlement index (% reduction in area) with potential of the as-received grade X100 tested in carbonate solution compared with that of the nitrate solution .....	116
Figure 4-57. Variation of embrittlement index (% elongation) with potential of the as-received grade X100 tested in carbonate solution compared with that of the nitrate solution.....	116
Figure 5-1. Secondary crack frequency on the gauge length at more than 1 mm from the fracture surfaces measured from SSRT on the grade X100 pipeline steel in the 1 M sodium hydrogen carbonate / 0.5 M sodium carbonate solution at 75°C .....	119
Figure 5-2. (a) Banding in the as-received grade X65 steel (b) was removed by furnace cooling after 5 hours at 1175°C and then air cooled after 20 minute at 950°C .....	125
Figure 5-3. Furnace cooled after 5 hours at 1175°C, then air cooled after 20 minute at 950°C and again furnace cooled after 20 minutes at 1000°C.....	126
Figure 5-4. Stress corrosion cracks in the shell of a coal gas liquor recirculating tank <sup>124</sup> .....	127

Figure 5-5. Crack morphology in spirally-welded pipe<sup>125</sup> .....128

## LIST OF TABLES

Table 2-1. Chemical composition of types of iron <sup>13</sup> .....	4
Table 2-2. Percentage effect on strengthening mechanisms <sup>15</sup> .....	27
Table 3-1. Pipe dimensions .....	52
Table 3-2. Chemical compositions in weight % (balance is iron in each grade) of the as-received steels determined previously <sup>6, 76</sup> .....	53
Table 3-3. Calculated weldability for the steels .....	53
Table 3-4. Mechanical properties of the steels in silicone oil at 75°C.....	53
Table 3-5. Bar dimensions and heating times for grade X65.....	59
Table 4-1. Average grain size of the as-received pipeline steels .....	73
Table 4-2. Effect of heat treatment on pearlite bands in the 'LT' face of grade X65 steel .....	81
Table 4-3. Details of the different types of film formed on the surface of the as- received grade X100 steel at different potentials, film growth time (4h) and micrographs were taken at 5000x .....	92

## Chapter 1 : INTRODUCTION

For nearly two decades, a new high strength steel (API 5L, grade X100) has been in development for high pressure and long-distance gas pipelines, to meet future demand. Traditionally, high pressure gas transmission lines are being operated at about 100 bar (10 MPa); and this can be adequately contained by grade X80 (highest grade in the line pipe codes). The operating pressure is expected to increase to 150 bar (15 MPa) in the future<sup>1</sup>. The advantage of such an increase would allow a larger volume of gas to be transported in a given time period. The benefits of using X100 over the lower grades include the use of: smaller diameter and reduced wall thickness with corresponding reduced material cost, lower construction cost, reduced compression cost and overall integrated project savings.

In spite of these advantages of using X100 grade, little has been established regarding susceptibility of the as-received microstructure of the grade X100 and its seam-weld heat-affected zone (HAZ) to environment-assisted cracking (EAC) as the as-received microstructure was carefully designed to give high strength and good toughness. The microstructure is a result of hot rolling low carbon austenite into fine grains and subsequently cooling them at a fast rate from a temperature close to the upper transformation temperature to a temperature just below the lower transformation. Thereafter, the rest of the cooling is in air. This industrial technique of manufacturing steels for pipeline is called thermo-mechanical processing. Steels produced from this method have been suggested<sup>2,3</sup> to offer good resistance to EAC although, the microstructures of such steels are generally designed with emphasis on mechanical property requirements rather than resistance to EAC. High pressure transmission pipelines on land are normally buried in the ground and a cracking environment may be generated as a result of variation or conversion of carbon dioxide containing ground water to high pH solution<sup>4</sup>. Hydrogen carbonate / carbonate solutions with a pH range between 9.0-10.5 have been reported<sup>5,6</sup> to cause cracks and lead to the catastrophic failure of a number of stressed and buried pipelines when associated with poorly applied cathodic-protection systems.



Cathodic protection is a method used to reduce or prevent the corrosion of metals or alloys exposed to aqueous electrolyte. It is a British technology and has been used in the United States for nearly a century in protecting buried steel pipelines transporting petroleum products against general corrosion<sup>7</sup>. Cathodic protection results from cathodic polarization of a corroding metal surface to reduce the corrosion rate. The desirable potential for protection at the pipe surface for buried steel pipes is approximately  $-775$  mV (sce)<sup>8,9</sup>. Pipelines are also coated to protect them from corrosion. Cathodic protection is used to complement the pipe coating and provides protection against corrosion at the sites of coating damage<sup>9</sup>.

The three main purposes of this thesis are to: (1) compare the relative susceptibility of the as-received parent metal, weld and simulated HAZ microstructures of grades X80 and X100 pipeline steels to environment-assisted cracking (EAC). This helps to establish what effect welding has on the susceptibility of as-received microstructures to environment-assisted cracking, (2) compare the susceptibility to EAC of the as-received microstructure of the newly developed grade X100 with existing grades and (3) investigate the role of carbon and manganese in the formation and removal of microstructural banding (segregation) in pipeline steels. This involves an investigation of the effect of banding on EAC. Pipeline steels are heavily hot-worked (controlled-rolling) to refine grain size and thus the average band spacing is reduced. The question here is whether the combined effect of grain refinement and the reduction in inter-band spacing may result in decreasing the time and temperature required to remove segregation through diffusion.

This thesis describes the results of a project which set out to achieve the above stated objectives. The relative susceptibility to EAC in sodium carbonate / sodium hydrogen carbonate solution under applied potential of the as-received and heat-treated microstructures of the alloys was determined using a slow strain rate test technique. This technique is generally accepted as excellent in comparing relative susceptibility and for studying influence of metallurgical variables. A few tests were also conducted in a sodium nitrate solution to get a comparison from a different environment.

## Chapter 2 : LITERATURE REVIEW

### *2.1 Steel*

Steel is an alloy consisting of mainly iron with a carbon content less than 2%. Other elements can be used as alloy in steels but iron and carbon are the only elements found in all steels<sup>10</sup>. The presence of a small concentration of carbon, for example 0.1-0.2 wt% C, has a strengthening effect on iron, a knowledge learnt over 20 centuries ago because iron heated in a charcoal fire can readily absorb carbon by solid-state diffusion<sup>11</sup>. Examples of the other alloying elements include: manganese, nickel, chromium, copper, sulphur, phosphorus and silicon. Based on the chemical composition, steels can be classified into five groups:

1. carbon steels
2. alloy steels
3. stainless steels
4. tool steels and
5. other steels ( for example steels for electrical applications)

#### **2.1.1 Steel manufacture**

The main raw material for steel manufacture is iron ore. The first refining of an iron ore has been reported to have taken place about 1500 B. C. and this symbolised the commencement of the Iron Age. In this period iron was basically used for coinage, cooking utensils, and implements of war<sup>12</sup>.

Pig iron is used in the manufacture of steels. The three main raw materials used in its manufacture are ore, limestone and coke. The ore consisting of iron oxide or carbonate with earthy impurities. The limestone is a substance used to combine with the non-metallic portion of the ore to form a slag, which is a fluid containing the oxides of calcium, aluminium, silicon and sometimes magnesium depending on the composition of the ore and the limestone. The coke is used to reduce the iron oxide to iron and to provide heat for melting the metal and the slag<sup>13</sup>. These three raw materials are smelted in a Blast furnace to produce iron. The structure of a large Blast Furnace used for producing pig iron is cylindrical in shape with an approximate

height of 30 m and is usually built of masonry and lined with a thick layer of fire brick or silica brick. It is surrounded by an outer shell of steel plates welded or riveted together. The furnace generally consists of three parts: an upper conical shaft, a middle part which is called Bosh, and a bottom part (Hearth) where the molten iron accumulates with the slag floating on top of it, both being tapped from time to time. The molten iron is cast into moulds to give pig irons<sup>14</sup>.

A mixture of pig irons, foundry scrap, steel scrap, limestone and coke is again melted in a cupola and cast into moulds to give cast iron. Cast iron usually contains 2-4 % carbon and in the as cast condition is not malleable. In the blast furnace pig iron absorbs carbon, silicon, manganese, sulphur and the whole of the phosphorus in the raw materials. These absorbed elements are considered as impurities in the pig iron, they are removed by fire-refining. The refined product is called wrought iron and other forms of pure irons include ingot iron and electrolytic iron. Table 2-1 shows a typical composition of pig, wrought and ingot iron.

**Table 2-1. Chemical composition of types of iron<sup>13</sup>**

Weight % Analysis	Pig iron	Wrought iron	Ingot iron
carbon	3.50	0.020	0.030
silicon	1.90	0.120	0.030
sulphur	0.06	0.018	0.038
phosphorus	1.00	0.228	0.009
manganese	0.70	0.020	-

There are a number of steel-making processes and these include: Bessemer, Siemens Open Hearth, Basic Oxygen furnace, Electric arc, Electric High-Frequency and crucible process. In the Bessemer process, air is blown through molten pig iron to oxidise the impurities: silicon, manganese, carbon and Phosphorus. Molten pig iron is poured into a converter (an egg-shaped vessel) and a strong blast of air is forced through it as it is rotated back to the vertical position. In a few minutes the silicon and the manganese are oxidised and form a slag. The oxidation process increases the temperature inside the converter. Carbon in the molten pig iron is oxidised to carbon monoxide and the latter burns with a long blue flame. When this flame burns down

the carbon has been reduced to the lowest practical limit and the operation is stopped. The required amounts of molten ferro-manganese alloy with composition (76-78% Mn and 0.6 -7 % C) and or spiegeleisen (also an alloy of iron containing 15-32% Mn and 4.5-5.5 % C) are added to deoxidise the melt and to produce the desired composition of steel, and the molten steel is more hotter than the original pig iron, is then cast.

When the above process is carried out in a furnace lined with siliceous materials the process is commonly known as the acid Bessemer process. In this process the metal used is grey hematite pig iron containing about 2-2.5% silicon. Oxidation of this element provides the heat required to maintain the metal in the fluid state. The metal should be free from sulphur and phosphorus, as these elements are not removed in the acid process. Phosphoric iron are treated by the basic Bessemer process in which the converter is lined with basic refractory materials (e.g calcined dolomite or magnesite) and lime is introduced into the charge. Instead of stopping the blast at the point at which the flame burns down, the blow is continued for some minutes longer to oxidise the phosphorus, which then combines with the lime, forming calcium phosphate, and goes into the slag<sup>14</sup>.

#### **2.1.1.1 Pipeline steel manufacture**

The acid open-hearth process was used for the production of steels for pipeline manufacture in the 1950s. This was the most effective method then available for producing moderately low carbon steels. The molten steel was treated with manganese to remove the bulk of the sulphur and oxygen, and then killed with calcium, silicon and aluminium to remove the residual oxygen and nitrogen before casting into ingots. The ingots would be transferred to the shaping plant to be cut into billets for seamless pipe manufacture or hot rolled into plate for welded pipe production. Pipeline steel is still made by this process, but it is not recommended for higher strength pipes and for those operating in severe service conditions.

Modern high quality pipeline steels are produced by the Basic oxygen process of steel manufacture or by the electric arc smelting. These processes produce steel that is low in carbon and sulphur, Phosphorus, oxygen, hydrogen and nitrogen (termed

SPOHN), manganese and microalloying elements need to be added. The sequence to produce the slab involves primary steel production, secondary or ladle steel production, and casting (Figure 2-1). Intermediate steps include magnetic stirring and degassing. The SPOHN elements are considered as harmful elements in pipeline steel and their recommended limits are shown in Figure 2-2. In the basic oxygen process, the primary furnace (Figure 2-1) to produce the primary steel is lined with a basic material, usually dolomite. The charge of “graded ore”, pig iron, and scrap is treated in the furnace to remove excess carbon by blowing oxygen through the molten steel. Sulphur and dissolved oxygen are removed by sequential addition of manganese, silicon and aluminium.

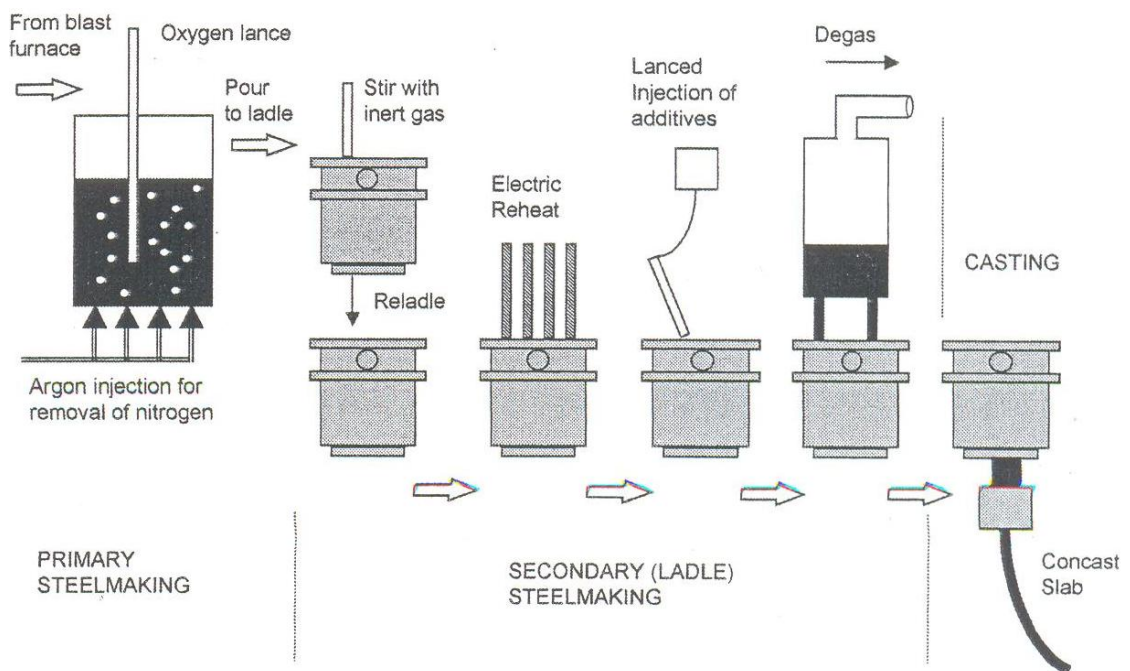


**Figure 2-1. Basic oxygen steel-making: primary and secondary processing<sup>15</sup>**

During production, the steel can absorb various gases. These reduce the fatigue properties of the steel because the small voids in the steel increase localized stresses and may coalesce under cyclic loading to produce micro-voids. For pipelines, the steel must be fully “killed”. Oxygen and nitrogen dissolved in the molten steel may be removed by purging with argon, which also stirs the steel and aids in the decarburization and dephosphorization of the steel, aids floatation of the slag, and reduces the volume of nitrogen absorbed in the steel. Various additives are used to absorb the residual gases, for example, silicon, aluminium and calcium and vacuum degassing are routinely used.

Steelmaking	Application		
	High strength, heavy wall pipe	Low temp. pipe	Corrosive gas transmission pipe
A clean steel			
S ≤ 0.006%	○		
S ≤ 0.002%	△	●	●
P ≤ 0.020%	○		○
P ≤ 0.010%	—	●	△
O ≤ 0.003%	△	●	●
H ≤ 1.5 ppm	●	○	△
N ≤ 40 ppm	○	●	△
B Ca treatment			
Ca 15–35 ppm	△	●	●
C low C steel	●	●	●
D inclusion control	○	○	●
E narrow range control of chemical composition	●	●	●

● indispensable; ○ necessary; △ desirable

**Figure 2-2. Steelmaking technologies to meet property requirements for pipeline steel<sup>16</sup>**

The treated molten steel is poured into ladles for secondary steel making. The first pour is stirred magnetically to aid removal of the residual slag and is transferred to a second ladle usually from the bottom of the first ladle to reduce carry-over of floating slag. After electric arc reheating whilst being magnetically stirred to ensure dispersion, the steel is injected with the relevant microalloying additives and the other major alloying elements to an appropriate level. The steel is then degassed and immediately and continuously cast into slabs instead of ingot<sup>15</sup>. Alloying elements are added to pipeline steels to alter the mechanical properties of the steel but also have an impact on the corrosion behaviour.

## **2.1.2 Fabrication of pipe**

Pipe for the oil and gas industry is made by one of four fabrication routes: seamless, longitudinally welded by electrical resistance welding, helical or spiral welded and longitudinally welded using submerged arc welding<sup>15</sup>. According to API specification 5L, pipes are generally divided into two groups based on the process of manufacture: seamless and welded (with seam). In the seamless process, steel is hot worked to form a tubular product without welding. The process involves piercing of solid billet into a tube and then to pipe. Welded pipes are classified according to the type of welding process used in producing the seam. For example an electric resistance welded pipe is a pipe that has one longitudinal seam produced by an electric welding process, in which heat for welding is generated by a resistance to flow of electric current. Another example is longitudinal seam submerged-arc welded (SAW) pipe. This is defined as pipe that has one longitudinal seam produced by the automatic submerged-arc welding process.

Figure 2-3 and Figure 2-4 demonstrate how U-O-E pipe is formed from a rectangular steel plate. First the plate is turned into a U, then into a tube (O). After longitudinally welding, the pipe is then expanded (E) to ensure circularity. Because the longitudinal weld is produced using a submerged arc welding process, the pipe is sometimes termed ‘SAW pipe’. The weld is inspected by ultrasonic examination and X-ray radiography. If the weld is acceptable, then the pipe is cold expanded to 1-2 %. The O-press leaves a residual 0.2-0.4 % compression in the pipe. Finally, the pipe is hydrostatically tested and then re-inspected using automatic ultrasonic testing and radiography<sup>15</sup>.

### **2.1.2.1 Welding of pipeline**

Welding<sup>15</sup> joins metals by inducing coalescence of the material, by heating to a suitable temperature with or without pressure and with or without the addition of filler metal. Coalescence is the growing together of the grain structure of the metals being welded. There are three critical parameters:

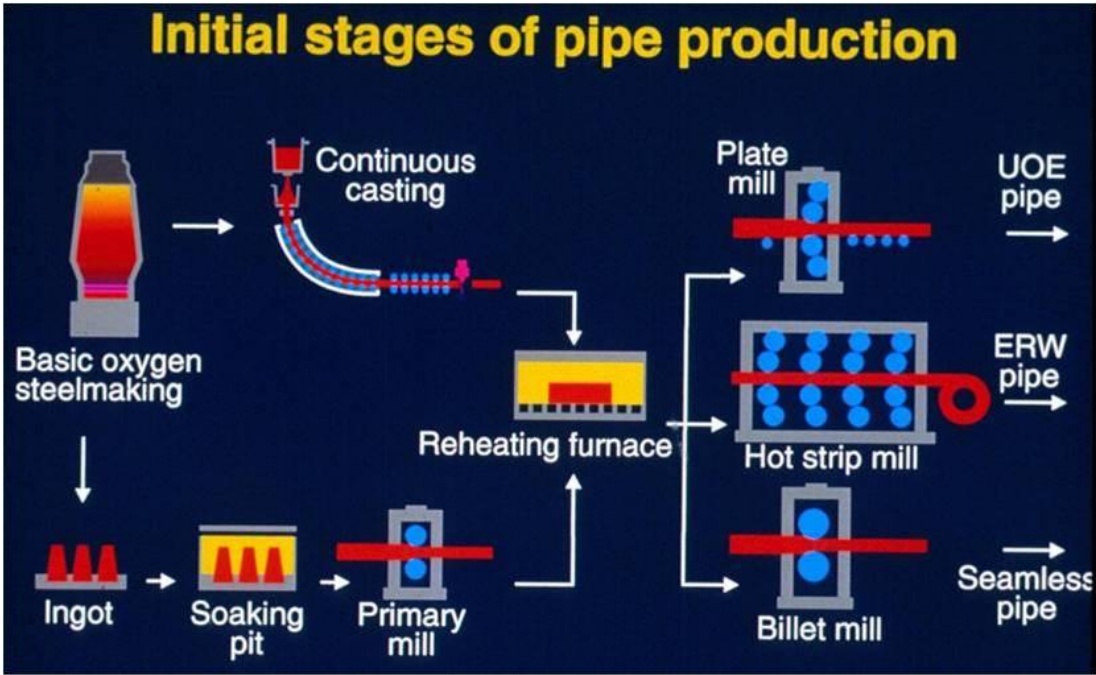


Figure 2-3. Initial stages of pipe production<sup>17</sup>

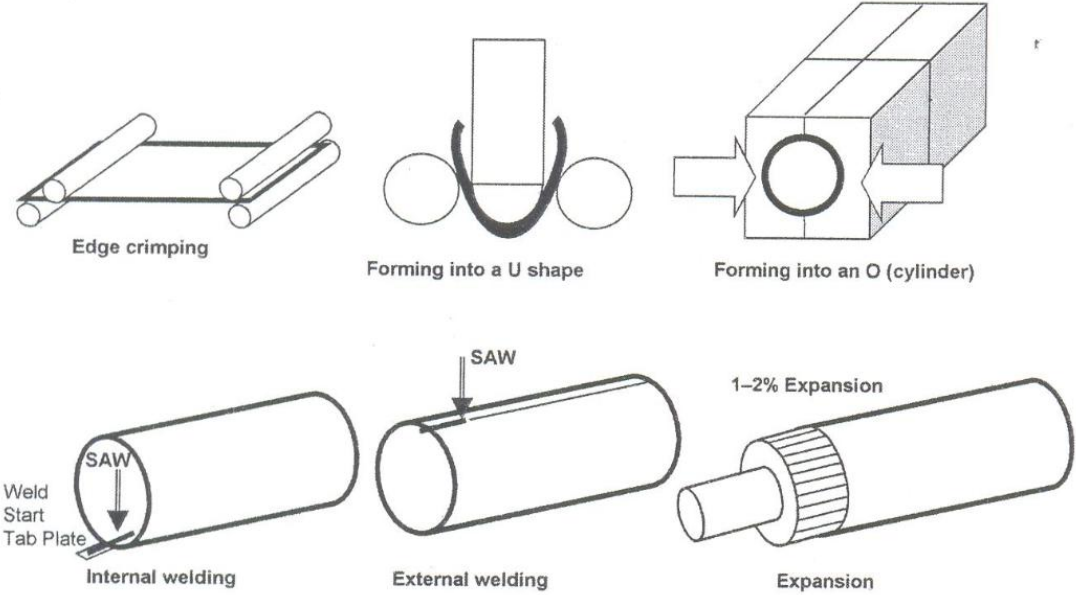


Figure 2-4. The final stages: U-O-E process<sup>15</sup>



1. Heat input: sufficient energy must be provided to melt the metal and consumable ( $\text{W/m}^2$ )
2. Heat input rate: the rate of energy input controls the rate of welding ( $\text{W/m}^2/\text{m/s}$ )
3. Shielding from the atmosphere: prevents oxidation of the molten melt that would produce a weak weldment

The fabrication of welded pipe requires fast welding procedures, and two processes are used: submerged arc welding and electrical resistance welding, the weld of pipe produced by submerged arc welding is generally made in two weld passes, one internal and one external. Electrical resistance welding is a single pass operation. These rapid techniques cannot be used for production of field girth welds. At present the girth welds are made exclusively by a sequence of arc welding processes in which the arc is a plasma discharge of high temperature, and typically four to seven passes are required. The electrical process to generate the plasma arc depends on the welding process. Direct current welding machines with drooping characteristics (drops globules of molten metal and slag) are used for manual arc welding with cellulosic-coated electrodes (coated with cellulose in the form of wood pulp, which decomposes in the heat of welding to protect the molten metal), and the voltages used are between 80-100 V, whereas gas metal arc welding and tungsten inert gas (used for welding corrosion resistance alloy pipelines) welding generally use pulsed alternating current.

Submerged Arc Welding (SAW) is used for producing longitudinally welded pipe formed by the U-O-E process and also for producing double or triple jointed pipe (24-36 m lengths). The metal is joined by fusing with an electric arc or arcs struck between a bare metal wire electrode or electrodes and the pipe. A blanket of granular, fusible material spread in a deep layer over the weld area shields the arc and molten metal<sup>15</sup>. The process is illustrated in Figure 2-5.

In the submerged arc and girth welding processes used for the seam and butt welding of pipelines, complete fusion of the steel occurs and the steel is diluted with a filler metal and cooled quickly. The structure of a weld metal usually consists of acicular ferrite with grain boundary ferrite in varying proportions and ferrite aligned with

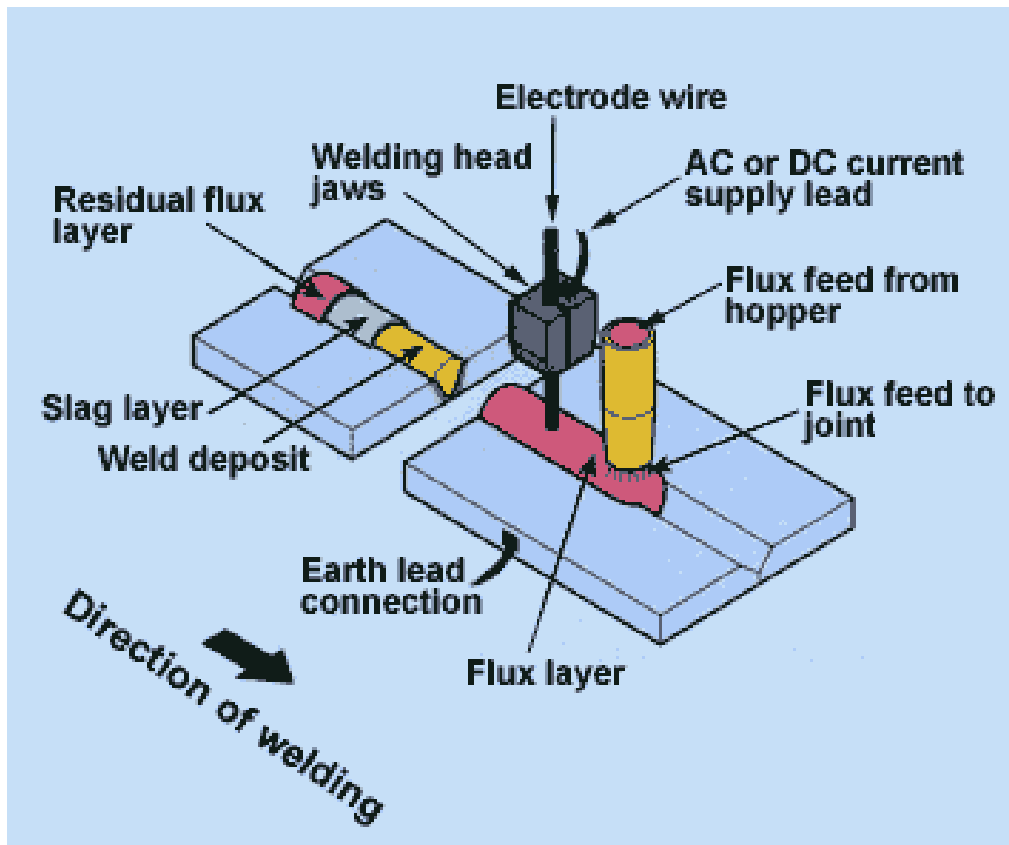


Figure 2-5. Schematic of a submerged-arc welding (from: [www.twi.co.uk/content/jk5.html](http://www.twi.co.uk/content/jk5.html), browse on the 30/09/10)

martensite-austenite-carbide (M-A-C) constituents, but the presence of microalloys, through their effects on hardenability, can modify these structures and through the precipitation of carbonitrides can increase and may lower the toughness of weld metal<sup>18</sup>.

### 2.1.2.2 Weld heat affected zone (HAZ)

The metallurgy of the welded joint can be largely categorized into two major regions:

1. the fusion zone which represents both the deposited metal and the parts of the steel component melted during the process, and is a solidification microstructure; and
2. the HAZ (Figure 2-6), represents those regions in the close proximity of the weld, where the heat input during welding changes the microstructure without melting the steel<sup>11</sup>.

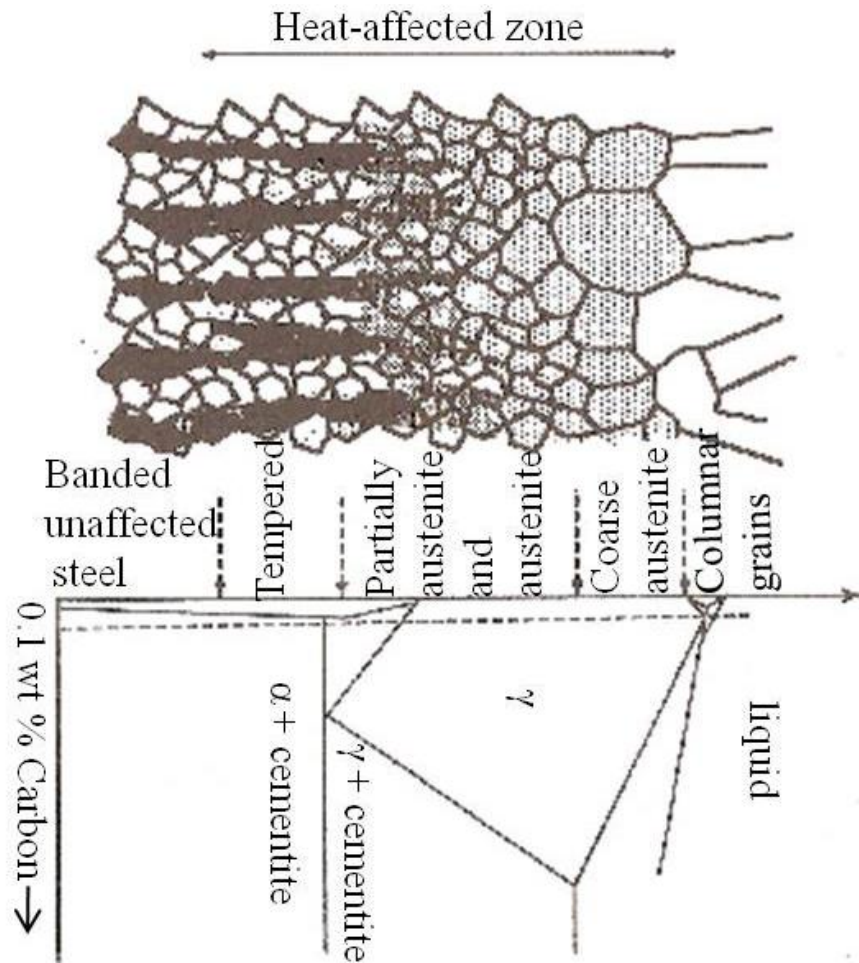
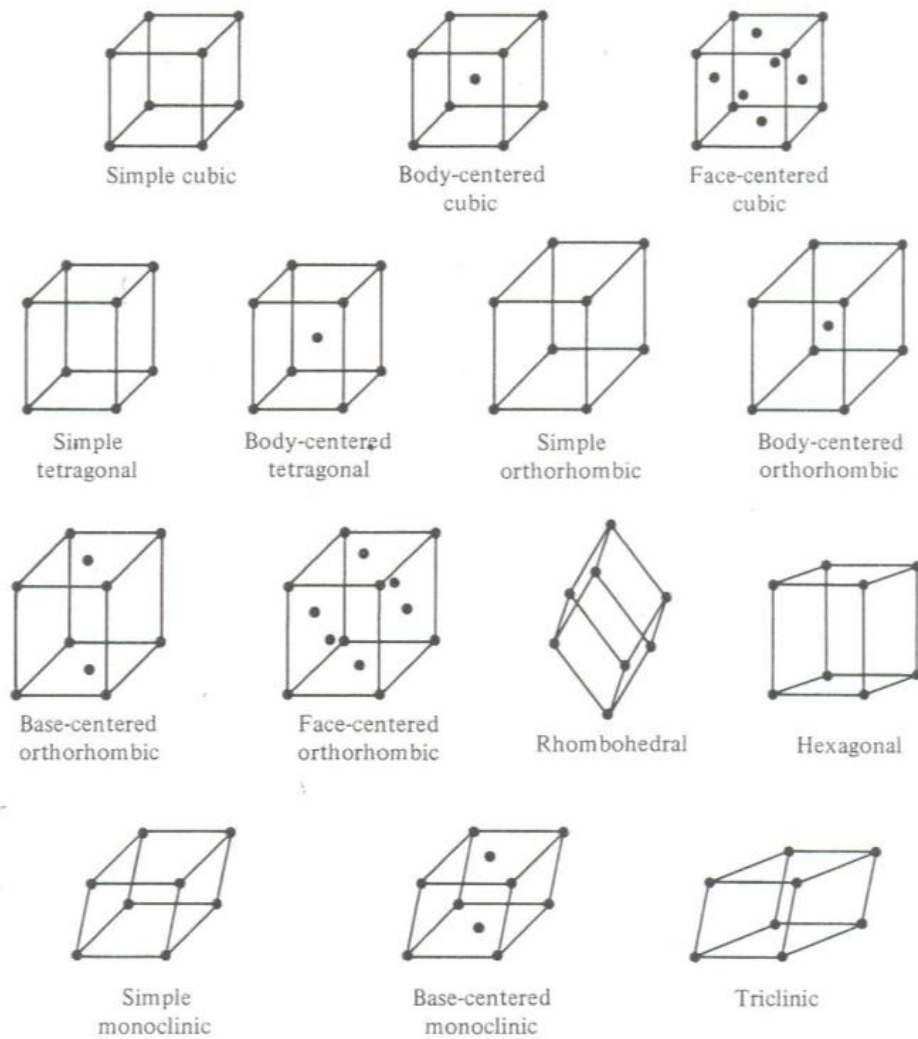


Figure 2-6. Schematic demonstration of HAZ showing regions of banded and non-banded microstructure<sup>11</sup>

### 2.1.3 Metal crystal structures

Metals have a crystalline structure and for this their atoms are arranged in a regular and repeating manner<sup>19</sup>. The unit cell of a metal structure should be one of the fourteen crystal lattices (Figure 2-7). There are three primary crystal structures observed for common metals: body-centred cubic (bcc), face centre cubic (fcc) and hexagonal close-packed (hcp). For example a structure of a ferrite ( $\alpha$ -Fe) is bcc. V, Cr and Mo also have a bcc structure. An alloy in which one of these metals is the predominant constituent will tend to have this structure also. However, the presence of alloying elements diminishes crystalline perfection<sup>19</sup>. The fcc structure is found in austenite ( $\gamma$ -Fe, stable from 912 to 1394°C), Al, Ni, Cu, Ag, Pt and Au. The hcp structure is typically found in Mg,  $\alpha$ -Ti, Zn, Be, and Zr.



**Figure 2-7. Fourteen crystal (Bravais) lattices, the dots indicate the atom positions<sup>19</sup>**

Flaws or imperfections in a regular arrangement of crystal are caused by 1) chemical impurity, 2) point defect (for example missing atom, vacancy or interstitial atom occupying and interstitial site not normally occupied by an atom in the perfect crystal structure or an extra atom inserted into the crystal structure such that two atoms occupy positions close to a singly occupied atomic site in the perfect structure<sup>19</sup>). The concentration of such defect rises exponentially with increasing temperature. Solid-state diffusion occurs by a mechanism of point defect motion, 3) linear defects (dislocation) which play major role in the deformation of crystalline materials and (4) planar defects which represent the boundary between a nearly perfect crystalline region and its surroundings<sup>19</sup>.

### 2.1.4 Diffusion

Diffusion in solid state is the movement of atoms from one lattice site to another. The diffusion of substitutional atoms is thought to be associated with lattice defects of which the most important are the vacant holes not occupied by atoms. Diffusion of vacancies in one direction will be accompanied by diffusion of atoms in the opposite one and this is supported by self-diffusion work using radio-active isotopes. An increase in vacancies in a sample should therefore be associated with an increased diffusion rate. The number of vacancies in a metal increases with temperature and it is also found that the rate of diffusion increases with temperature. Drastic quenching of an alloy can retain a greater number of vacancies in a sample and subsequent changes, such as precipitation hardening, are accelerated. Irradiation and plastic deformation also produce non-equilibrium concentrations of vacancies. Diffusion rates are also higher through a grain boundary region than through the bulk of the metal; are also higher in cold worked metal where there are more imperfections in the lattice. Therefore cold working is an advantage before a homogenising anneal<sup>13</sup>. Diffusivity data are perhaps the best known examples of Arrhenius equation:

$$D = D_0 e^{-Q/RT} \quad 2-1$$

where  $D_0$  being the pre-exponential constant,  $Q$  the activation energy for defect motion,  $R$  gas constant, 8.314 J/mol K and  $T$  absolute temperature in Kelvin.

A comparison of the diffusivities of the C atom (interstitial) with that of Mn (substitutional) in both ferrite and austenite shows that the substitutional atom moves several orders of magnitude more slowly. As a result, 'it should be noted that homogenizing treatments designed to eliminate concentration gradients of solute elements need to be much more prolonged and at higher temperatures when substitutional rather than interstitial solutes are involved<sup>11</sup>'.

### 2.1.5 Dislocation

Linear defects (dislocations) are associated primarily with mechanical deformation whereas point defects are structural imperfections resulting from thermal agitation.

Plastic (permanent) deformation of crystalline solids is difficult without dislocations. Unhindered dislocations move freely along shear slip planes during plastic deformation. Their free movement may be impeded by interaction with each other in cross slip, in which a dislocation changes from one slip planes to another intersecting slip plane and other barriers such as grain boundaries and precipitates<sup>13</sup>. Cold working increases dislocations density to serve as obstacles and so increases resistance to plastic deformation. Foreign atoms can also serve as obstacles to dislocation motion. This is the basis for solid solution hardening of alloys, that is restricting permanent deformation by forming solid solution. Obstacles to dislocation, motion harden metals, but high temperatures can help to overcome these obstacles and thereby soften the metals<sup>19</sup>.

Planar defects include any boundary surface surrounding a crystalline structure. The predominant microstructural feature for many engineering materials is grain structure, where each grain is a region with a characteristic crystal structure orientation. The structure of the region of mismatch between adjacent grains, that is the grain boundary, depends on the relative orientation of the grains<sup>19</sup>.

Basically, dislocation could be an edge or a screw depending on the direction of the Burgers vector (displacement vector necessary to close a stepwise loop around a dislocation). In edge dislocation the vector is perpendicular to the dislocation line whereas in screw dislocation the vector is parallel to the dislocation line<sup>19</sup>.

### **2.1.6 The iron-carbon phase diagram**

A phase is a chemically and structurally homogenous portion of a microstructure. An iron-carbon phase diagram (Figure 2-8) is used to identify the different structures of steel that occur at various temperatures for a given composition. The diagram allows one to determine the phases in the steel at different temperatures that is whether the steel is comprises ferrite, pearlite, cementite, austenite, or any combination of these four phases. Grain refinement occurs when steel with less than or equal to 0.85 percent carbon is heated in a region of about 100°C above the lower austenite transformation temperature that is the lower boundary of the grain refining zone shown in Figure 2-8.

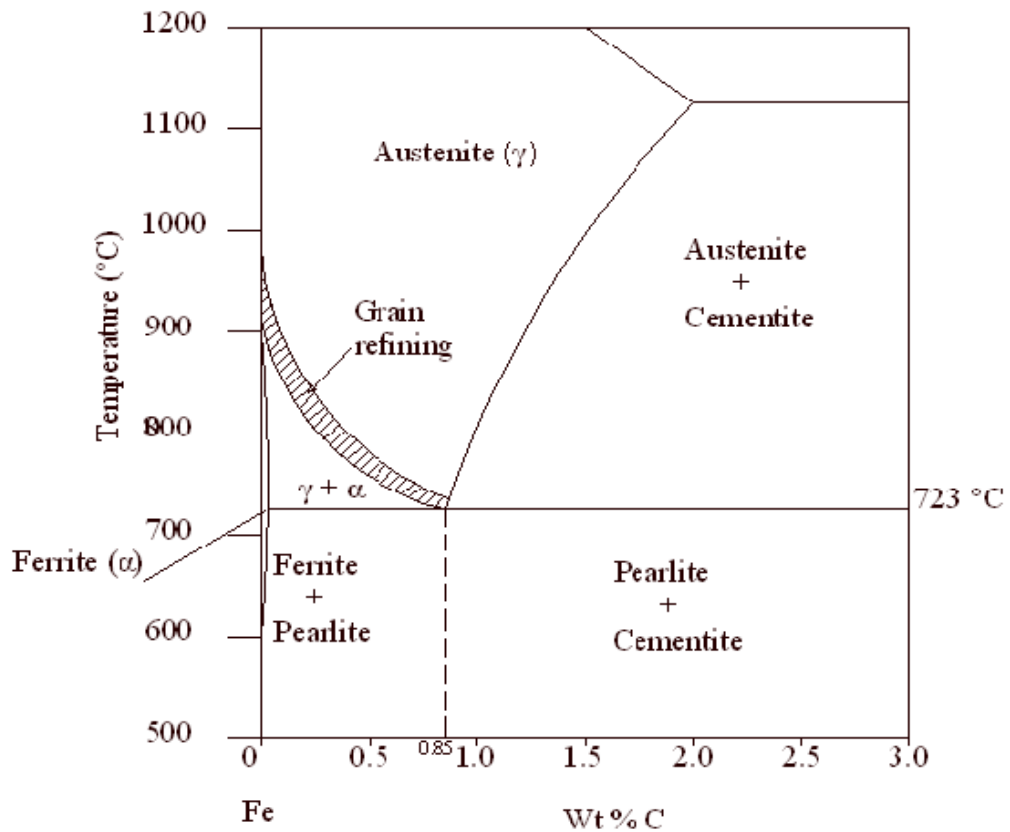


Figure 2-8. Iron-carbon phase diagram<sup>10</sup>

At the eutectoid line (723°C), the transformation of steel to austenite (a solid solution of carbon in face-centred cubic iron) begins and the transformation is complete at a temperature just above the lower austenite transformation temperature line. The eutectoid line and the lower austenite transformation line are called  $A_1$  and  $A_3$  lines, respectively. These lines are easily detected by thermal analysis or dilatometry during cooling or heating cycles, and some hysteresis\* is observed. 'Consequently, three values for each point on the lines can be obtained,  $A_c$  for heating (chauffage<sup>♦</sup>),  $A_r$  for cooling (refroidissement) and  $A_e$  (equilibrium), but it should be emphasised that  $A_c$  and  $A_r$  values will be sensitive to the rates of heating and cooling, as well as to the presence of alloying elements<sup>11</sup>'. For example, an increase in the concentration of Mn lowers the transformation temperatures. The  $A_c$  points are in general from 10 to 30 °C higher than the  $A_r$  points. For pure iron,  $A_{r3}$  would correspond to the heat evolution at about 906 °C and  $A_{c3}$  to the point at which

\* (thermodynamics) A phenomenon sometimes observed in the behaviour of a temperature-dependent property of a body; it is said to occur if the behaviour of such a property is different when the body is heated through a given temperature range from when it is cooled through the same temperature range<sup>11</sup>.

♦ Chauffage and refroidissement are French words mean heating and cooling, respectively.

heat is absorbed on heating. Similarly for pure iron, the  $A_{c3}$  would be found at the range 915 to 935 °C depending on the degree of purity of the iron. The addition of carbon gradually reduces this to 723 °C.

The difference in carbon solubility between austenite ( $\gamma$ ) and ferrite ( $\alpha$ ) iron leads normally to the rejection of carbon as iron carbide at the boundaries of the  $\gamma$  – phase field. The transformation of  $\gamma$  to  $\alpha$ -iron occurs via a eutectoid reaction which plays a dominant role in heat treatment, the eutectoid temperature is 723 °C while the eutectoid composition is about 0.85 weight percent(wt%) carbon (C). On slow cooling of alloys containing less than 0.85 wt% C slowly, hypo-eutectoid ferrite is formed from austenite in the range 910-723 °C with enrichment of the residual austenite in C, until at 723 °C the remaining austenite, now containing 0.85 wt% C, transforms to pearlite, a lamellar mixture of ferrite and iron carbide (cementite). In austenite with 0.85 to 2.06 wt% C, on cooling slowly in the temperature interval from 1147 to 723 °C, cementite first forms, progressively depleting the austenite in carbon until, at 723 °C, the austenite contains 0.85 wt% C and transforms to pearlite.

Steels with less than about 0.85 wt% C are thus hypo-eutectoid alloys with ferrite and pearlite as the prime constituents, the relative volume fractions being determined by the lever rule which in this case indicates that as the carbon content is increased, the volume percentage of pearlite increases, until it is 100 % at the eutectoid composition.

In order to change the microstructure of steel, it must first be austenitic and cooled at different rates to obtain ferrite/pearlite, bainite or martensite. Slow cooling gives a ferrite/pearlite microstructure while quenching gives either bainite or martensite depending on the carbon content. Martensite is a microstructure produced by diffusionless transformation of austenite whereas bainite is produced through diffusion transformation and the resulting microstructure is extremely fine ferrite and cementite. When a semikilled steel, or a steel that has been Si-killed, is heated above the upper transformation temperature, austenite grain growth increases with time and temperature. When Al-killed steel is reheated, the austenite grains grow very little during the periods customarily employed, up to a temperature of about 1100 °C; but if this temperature is exceeded, grain growth is rapid and the final grain size at a



given temperature can be greater than in the Si-killed steel<sup>20</sup>.

### **2.1.6.1 Solubility of carbon and manganese in ferrite and austenite iron**

The addition of carbon to iron is sufficient to form steel. However, steel is a generic term which covers a very large range of complex compositions. The atomic size of carbon is small when compared with that of iron which allows this element to enter the ferrite-iron and austenite-iron lattices as an interstitial solute atom. However an element such as manganese an atom which is nearer in size to that of iron and, as a result, enters into substitutional solid solution<sup>11</sup>.

The solubility of carbon in austenite is greater than that of ferrite because of the larger interstices available. For example the solubility of C in austenite and ferrite at 723 °C are 0.85 and 0.02 wt% C respectively. The marked difference in solubility is of profound importance in the heat treatment of steels.

### **2.1.7 Strengthening mechanisms in metals**

Strengthening in metals<sup>21</sup> relates to processes by which dislocation motion is restricted within the lattice. These include for example: strain hardening involves dislocation interactions with other dislocations, grain boundaries, solute atoms (solid solution strengthening), precipitates (precipitation hardening) and dispersoids (dispersion strengthening).

Strain hardening or cold working increases the number of dislocation to dislocation interactions which reduces dislocation mobility. As a result larger stresses must be applied in order that additional deformation can take place. For strain hardening to occur a dislocation density of at least  $10^{10}/\text{cm}^2$  is required. On the other hand, absence of dislocations also indicates a high level of strength. Metals with very high dislocation density ( $10^{11}$  to  $10^{13}$  dislocation/ $\text{cm}^2$ ), remain stable only when the combination of stored strain energy (related to the dislocation substructure) and thermal energy (determined by the deformation temperature) is below a certain level. If not, the microstructure becomes unstable and new strain-free equiaxed grains are

formed by combined recovery, recrystallization, and grain growth processes. The new grains will have a much lower dislocation density (in the range of  $10^4$  to  $10^6$  dislocations /  $\text{cm}^2$ ). When mechanical deformation at a given temperature causes the microstructure to recrystallize spontaneously, the material is said to have been hot worked<sup>21</sup>.

The presence of grain boundaries has an additional effect on the deformation behaviour of a material by serving as an effective barrier to the movement of glide dislocations. Refinement of the grain size increase the density of grain boundary and is one of the most important ways of strengthening steels. The Hall-Petch equation is generally acceptable for estimating increase in yield strength due to reduction in average grain size. The equation states that yield strength is inversely proportional to the square root of the grain diameter. The equation has since been shown to be valid only for a grain diameter greater than  $20 \text{ nm}^{11}$  although this accounts for the majority of steel alloys.

The yield strength of pipeline steel is determined by several parameters which can be expressed in a modified Hall-Petch relationship given by Morrison and Chapman<sup>18</sup>:

$$\sigma = \sigma_1 + \sigma_{ss} + \sigma_{ppt} + \sigma_{disl} + \sigma_{text} + K_y d^{-1/2} \quad 2-2$$

Where:

$\sigma$  = yield strength

$\sigma_1$  = lattice friction stress (overall resistance of lattice to dislocation movement)

$\sigma_{ss}$  = solid solution strengthening

$\sigma_{ppt}$  = precipitation strengthening

$\sigma_{disl}$  = dislocation strengthening

$\sigma_{text}$  = texture (lattice orientation) strengthening

$d$  = ferrite grain diameter

$K_y$  = constant (“locking parameter,”) which measures relative hardening contribution of grain boundaries

The potential interaction between an edge or screw dislocation with a solute atom depends on the stress field associated with the solute. For example, if an atom of chromium were to substitute for an atom of BCC iron, the host lattice would experience a symmetrical (hydrostatic) misfit stress associated with differences in size between solute and solvent atoms. Lattice distortion would be felt equally in all directions with the strengthening contribution being proportional to the magnitude of the misfit  $\epsilon$  such that

$$\epsilon \propto \frac{da}{dc} \quad 2-3$$

Where  $a$  = lattice parameter and  $c$  = solute concentration.

The relative strengthening potential for a given solute atom is determined by the nature of the stress field associated with the solute atom. When the stress field is symmetrical, the solute atom interacts only with the edge dislocation and solid solution strengthening is limited. When the stress field surrounding the solute atom is nonsymmetrical in character, the solute atom interacts strongly with both edge and screw dislocations; in this instance, the magnitude of solid solution strengthening is much greater. The degree of solid solution strengthening depends on whether the solute atom possesses a symmetrical or nonsymmetrical stress field and not whether it is of the substitutional or interstitial type.

### **Precipitation hardening**

It is only precipitates which occur in ferrite that have a direct influence on steel properties and this occurs in two forms: (i) as interface precipitates, and (ii) as random precipitates in the ferrite forming at lower temperatures after the ferrite transformation has been completed.

## ***2.2 As-received pipeline steel***

Steels for seamed pipelines are cold worked during pipe forming and expansion. This alters the mechanical properties of the steels plates used in forming the pipes. In

some steels it lowers the strength of the pipe compared with the plate and in others it increases the strength; in almost all steels it reduces the steel toughness. The microstructure of a steel pipe controls its properties and it is determined by: (i) the effect of alloying elements on the kinetics of transformation and the formation of intermetallic compounds, i.e the effects on the basic structure (ii) the effect of secondary constituents on the structure, such as inclusions, which are in turn controlled by (iii) steelmaking and casting processes and hence by the plant available for making and treating steel (iv) the properties required by the pipeline engineers.

Pipeline steel microstructures could be broadly classified into three groups based on the mechanisms of deformation<sup>18</sup>:

- (a) the traditional ferrite-pearlite steels, although with low or reduced pearlite content, which exhibit a discontinuous (show upper and lower yield points) stress-strain curve in the tensile test;
- (b) ferrite-pearlite steels containing transformation products (bainite/martensite) to increase the work hardening coefficient and
- (c) Steels containing polygonal ferrite and a major portion of a second phase, such as low carbon bainite (sometimes called acicular ferrite) or islands of martensite and retained austenite which exhibit a continuous stress-strain curve in the tensile test. Steels with such microstructures are strengthened during both pipe forming and expansion processes.

Microalloying elements play a critical part in determining the microstructure and properties of pipeline steels and their effects are influenced by rolling schedules. Most high strength steels for pipelines are given some form of controlled rolling or thermomechanical treatment in order to develop the microstructure required to achieve the desired properties. The functions of the microalloying elements results partly from their effect in solid solution, but mostly from their effects as precipitates. According to Sage<sup>18</sup>, there is little evidence to indicate that their influence is related to precipitate morphology or their composition. Their effect therefore is a function of their size and the temperature at which they exist in relation to the transformation temperature of steel. The temperature at which precipitates form and their rate of growth are influenced by the rate of cooling. The presence of Cr, Cu and Mo in solid solution stifle precipitation and therefore refine the precipitates. Ti, Al,

Nb and V precipitate as either carbide or nitride. The main effects of these elements and Mo are summarised below<sup>18</sup>:

- Ti precipitates in austenite to stabilise austenite grains and thus contributes to ferrite grain refinement which in turn increase both strength and toughness. However, Ti as ferrite precipitates, increases strength but decreases toughness.
- Al also precipitates in austenite and it stabilises austenite and thus contributes to the formation of fine grain ferrite which increases both strength and toughness.
- Nb as austenite precipitates contributes to ferrite grain refinement, whereas as ferrite precipitates increase strength only. It also increases hardenability which decreases weld toughness.
- V as austenite precipitate increases both toughness and strength but as interphase and ferrite precipitate increases only strength. It also increases hardenability and favours formation of martensite.
- Mo increases hardenability, favours formation of martensite and retards precipitation.

Controlled-rolling is a technique which produces strong and tough steel by refining ferrite grains. In this process, re-crystallization during or immediately after hot rolling is controlled by the rolling conditions and by the addition of micro-alloying elements such as niobium, titanium and vanadium. During cooling after controlled-rolling the transformation of austenite produces fine ferrite grains. In addition to controlled-rolling the precipitation of carbonitrides of the alloying elements contributes to strengthening of the steel to some degree<sup>22</sup>. The major purpose of controlled-rolling is to refine the structure of the steels and, thereby, to enhance both strength and toughness.

Controlled rolling could be done in four stages and only two or three stages are involved in many practices:

- (I) High temperature rolling of austenite which may recrystallize if the deformation is sufficient

- (II) Rolling of austenite between a temperature below which it does not re-crystallize or is prevented from re-crystallizing and the  $Ar_3$  temperature
- (III) Rolling between the  $Ar_3$  and  $Ar_1$  temperature when ferrite may recover or re-crystallize and when an irregular grain size may be produced
- (IV) Rolling at a low temperature when ferrite will be cold worked and will not re-crystallize unless heavily deformed.

### **2.2.1 Development in pipeline steel production**

Over three decades of development in the production of pipeline steels is summarised in Figure 2-9. According to the American Petroleum Institute's specification, steel grades are labelled with the letter 'X'. For example, a steel of grade X60 has specified minimum yield strength (SMYS) of 60,000 pounds per square inch (psi) which is equivalent to 413 MPa. The specification has since been converted into an international standard, International Organization of Standardization (ISO) 3183<sup>15</sup>.

The most common grade of pipeline steel before the 1960's was X52 steel which was made from 'semi-killed' steel and bought without toughness requirements. Semi-killed steel has poor toughness and low strength as not all the oxygen was removed in the molten steel. Steels must be fully killed to enable addition of aluminium to refine grain size; giving the steel greater resistance to brittle fracture. Niobium or vanadium could be used to reduce grain size in semi-killed steel but aluminium is more effective for this.

A gas pipeline that experienced a long running brittle fracture in the United States of American (USA) before the 1960's led to the inclusion of a Battelle Drop Weight Tear Test (DWTT) requirement in pipeline steel specifications and this led to a change in steelmaking practice. DWTT is a test used to measure resistance to brittle fracture propagation.

In the 1960's to early 1970's, steels were fully-killed with Si and Al treatment and then cast to either ingot (suitable shape for further processing) or continuously cast into thick slab and subsequently rolled into plate. Pipeline plate was hot-rolled and then normalised at 900°C to give finer grain size with better toughness. Although,

high strength could only be achieved by alloying, this in turn led to high carbon equivalent (CE) and poor weldability.

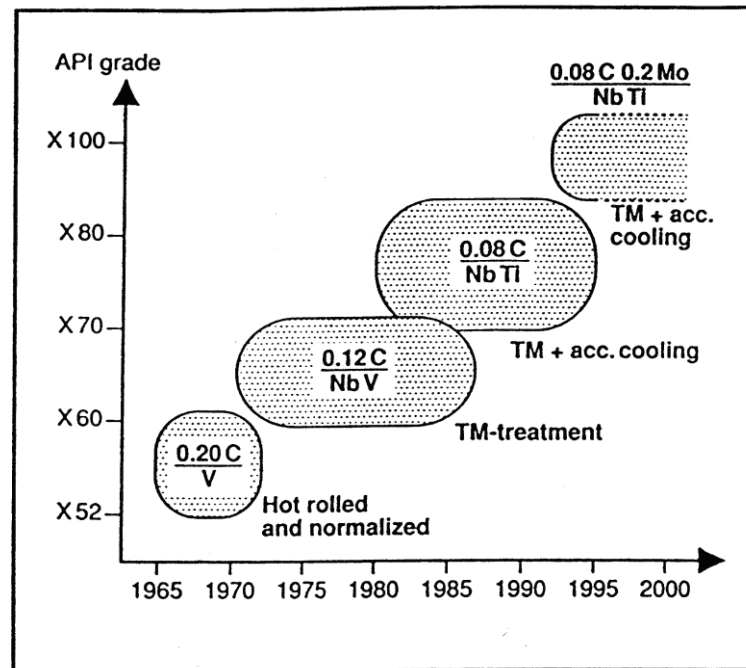


Figure 2-9. Developments in pipeline steels production <sup>23</sup>

Controlled-rolled or thermo-mechanical treated (TM) steels were developed in the 1970's and were Si killed, Al treated, and also micro alloyed with niobium and/or vanadium. Plates are hot-rolled to a finishing temperature down to around 800°C. These steels have high strength, good toughness and low CE (good weldability)

From the 1990's onwards, higher strength (X70–X80) was achieved through controlled-rolling and accelerated-cooling. Steels produced in this way are called thermo-mechanical controlled processed (TMCP) steels

### 2.2.2 Development of X100 steel

X100 is a high strength pipeline steel and it is also a product of the application of thermo-mechanical controlled-rolling and accelerated-cooling<sup>24-26</sup>. The steel plates used to make grade X100 line-pipes are carefully hot rolled from a start temperature of about 1200°C to a finish temperature of 800°C and then rapidly cooled at a rate greater than 10°C/s to obtain a fine-grained microstructure<sup>25</sup>. High strength was

attained through grain refinement, solid solution hardening and precipitation hardening which is an application of the modified Hall-Petch equation. In addition to controlled-rolling and accelerated cooling, the high strength of X100 was partly achieved through optimised addition of certain alloying elements. For instance, niobium, V and Al are added to steels to refine grain size<sup>20</sup> and so yield strength is increased. An optimised amount of Ti was added to prevent grain coarsening in the heat affected zone (HAZ). Carbon content as low as 0.06% was adopted to improve resistance to cold cracking during field welding. Figure 2-10 forms the foundation for the design of microstructures and mechanical properties of most high strength pipeline steels. The figure suggests that the mechanical properties of a grade X100 steel can only be achieved by having a bainitic microstructure<sup>27, 28</sup> According to Hillenbrand et al.<sup>28</sup> the highest grade obtainable with pearlite-ferrite microstructure while maintaining weldability and favourable ductile brittle transition temperature is grade X70 and development of grade X80 steel can only be attained by changing the microstructure of the steel matrix from ferrite-pearlite to ferrite-bainite.

## ***2.3 Properties of pipeline steel***

### **2.3.1 Strength**

A pipeline steel<sup>15</sup> must have high strength while retaining ductility, fracture toughness, and weldability. Strength is the ability of the pipe steel with its associated welds to resist the longitudinal and transverse tensile forces imposed on the pipe in service and during installation. Ductility is the ability of the pipe to absorb overstressing by deformation.

Yield strength is a primary design parameter. As the yield strength increases, the wall thickness requirement decreases. A thinner pipe wall reduces material costs, transportation costs, load on the lay barge ‘stinger’ (an inclined ramp gradually lowers welded pipes into water in an offshore pipeline construction), and welding costs.

Submarine pipelines are generally designed in strength grades up to X65. The reason for this limitation on strength, compared to the highest strengths available, relates to other pipeline design requirements that can mandate the provision of a thicker wall



than that required for pressure containment. These requirements may include on-bottom stability, resistance to buckling during installation and stresses imposed during reeling.

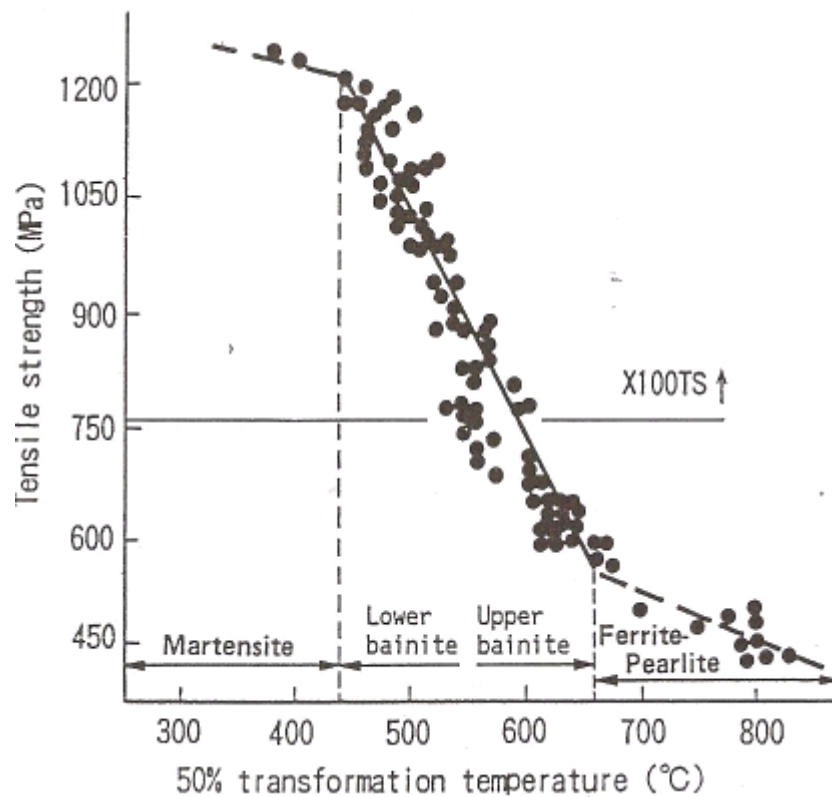


**Figure 2-10. Relationship between 50% transformation temperature and tensile strength of continuously cooled steels<sup>27</sup>**

Over the last decade, many onshore pipelines have been constructed with grade X70 and X80 steels; and confidence has grown in the use and welding of these steels. Consideration is now being given to use of pipe to grade X100. It is expected that higher strength pipes will be more widely used for submarine pipelines in the future. As stated in section 2.1.7 steel strength can be increased by the use of one or a combination of the following mechanisms:

- Solid solution strengthening by addition of alloying elements C, Si, Mn etc
- Grain refining
- Precipitation strengthening by microalloying with Nb, V, Ti
- Transformation strengthening by formation of martensite and bainite
- Dislocation strengthening by work hardening

Steps in the historical use of these mechanisms in pipeline production are illustrated in the Figure 2-11. For API 5L type pipeline steel with 1.5% manganese, the typical percentage effects of the strengthening processes are given in Table 2-2.

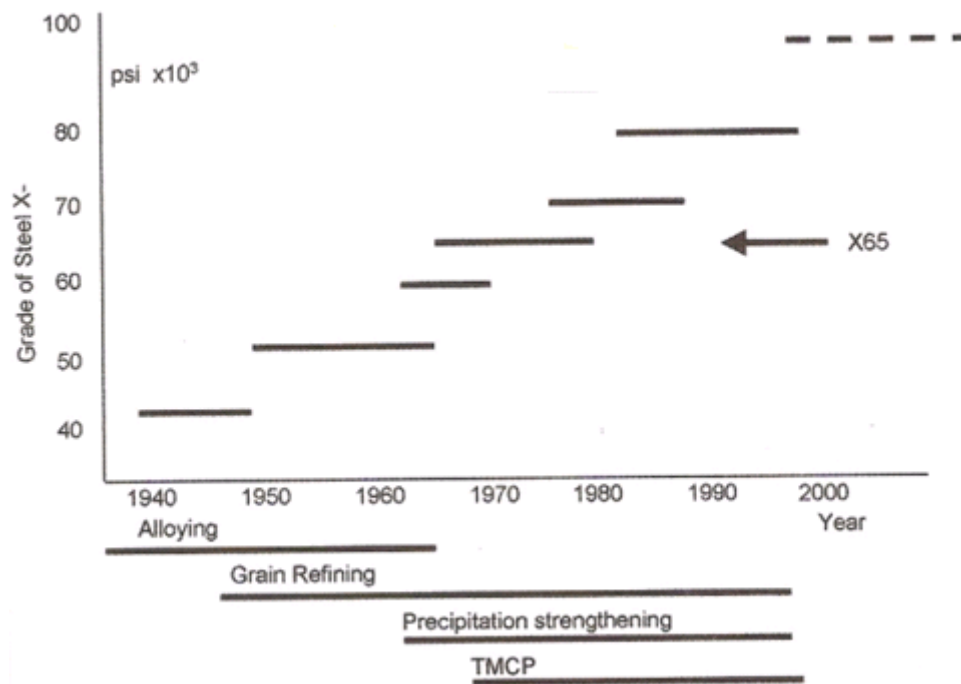


Figure 2-11. Application of strengthening mechanism to pipeline steels<sup>15</sup>

Table 2-2. Percentage effect on strengthening mechanisms<sup>15</sup>

Strengthening option	Mechanism	% Effect on strength
Base line strength		18
Addition of silicon and nitrogen	Solid solution	8
Addition of manganese	Solid solution	12
Ferrite grain size	Grain refining	45
Micro-alloying	precipitation	17

### 2.3.2 Toughness

Toughness is the ability of a line pipe steel to resist crack propagation. Cracks propagate in both brittle and ductile manners. Cracks are initiated on pipeline steel when it comes in contact with an environment that promotes cracking or by third party activities: for example an excavator hitting a pipe during construction. Tests are available to measure the resistance of a line pipe steel to crack initiation and propagation. The Battelle Drop Weight Tear Test (BDWTT) is used to measure the resistance to brittle fracture propagation and the Charpy V notch impact test is used to measure the resistance to ductile and brittle fracture propagation<sup>29</sup>. The BDWTT

test uses a full pipe wall thickness rectangular bar specimen taken in the circumferential direction which is given a pressed notch before being broken by a Drop Weight Tear Testing Machine. Because carbon-manganese steels exhibit a transition from ductile to brittle behaviour as the testing temperature decreases, the appearance of the DWTT specimen after testing will either be fully ductile, fully brittle or mixture of both. A minimum percentage of fibrosity in the test piece is required to ensure brittle fracture propagation will not occur in the pipeline. Current specifications call for a minimum of 75-85% fibrosity in the DWTT at pipeline minimum design temperature.

In the Charpy V notch toughness test. The specimen is a 55mm long, 10mm by 10mm bar (or thinner to suit the pipe wall thickness and curvature) which has a 2mm deep machined notch at its mid point. Again the specimen is taken in the circumferential direction; so that when it is broken open in three-point bending the fracture propagates in the pipe axial direction. In this case the impact energy to fracture the specimen is recorded, again at the pipeline minimum design temperature. The required level of Charpy absorbed energy is related to the behaviour of similar pipe in full scale fracture propagation tests as there are a number of relationships between the pipeline material, the diameter and operating conditions, and the specified level of energy in the Charpy test. The relevance of the Charpy test to the full scale fracture behaviour of high strength steels of grade at least X80 is being debated and alternative tests are being considered<sup>17</sup>.

### **2.3.3 Weldability**

Weldability is the ability of the steel to be welded without the weld suffering from cracking or excessive hardness. The weldability of a pipeline steel can be controlled, to a certain extent, by controlling the chemistry of the steel. When a fusion weld is made, a heat affected zone (HAZ) is created in the parent material adjacent to the weld and this zone undergoes a rapid thermal cycle during welding. The portion nearest to the weld sees a high peak temperature. This results in coarsening of the grain structure in the steel. The rapid cooling after welding then result in hardening of the coarse grain region and this region is therefore normally the hardest and least tough part of the weld. In general, higher chemistry pipes harden more readily in the

HAZ than lower chemistry pipes. Also for a given chemistry, a thicker pipe will have a poorer weldability than a thinner component because it will provide a greater sink for the heat of the weld, leading to more rapid cooling and thus greater hardening. The thicker component will also lead to higher restraint in the weld area, so that the resulting residual stresses will be higher<sup>17</sup>. For steel, the carbon content largely defines the weldability. Weldability is defined by converting the other elements in the steel into a carbon equivalent and the sum is used as a guide to the weldability of the steel. The most commonly used formula for calculating carbon equivalent (CE) for pipeline is the international formula given in the API Specification 5L:

The CE and a material's cracking parameter (Pcm) values indicate how weldable a steel is and the empirical formulae to calculate them are given below. It is required that pipeline steel should have good strength to contain the internal pressure, good toughness to resist crack propagation and it should also be weldable. Because of these requirements, the alloying elements in pipeline steels are carefully selected to obtain an optimal combination of strength, toughness and weldability. For instance, an increase in carbon content increases both tensile strength and carbon equivalent (CE) but an increase in CE decreases weldability.

$$CE = C + \frac{Mn}{6} + \frac{(Cr + Mo + V)}{5} + \frac{(Ni + Cu)}{15}$$

$$Pcm = C + \frac{Si}{30} + \frac{Mn}{20} + \frac{Cu}{20} + \frac{Ni}{60} + \frac{Cr}{20} + \frac{Mo}{15} + \frac{V}{10} + 5B$$

According to the American Petroleum Institute's specification for line pipe (API 5L), when the carbon content is greater than 0.12% the weldability shall be calculated using CE and if the carbon content is less than or equal to 0.12%, then the Pcm formula is recommended and the maximum carbon equivalent shall not exceed Pcm of 0.25% and CE of 0.43% for all seam pipes of grade less than X80 and for all seamless pipe with specified wall thickness less than 20.3 mm<sup>30</sup>.

## 2.4 Banding

Banding is defined as inhomogeneous distribution of alloying element or phases aligned in filaments or plates parallel to the direction of working<sup>31</sup> or chemical segregation in steel produces alignment of the microstructure into longitudinal bands after hot rolling that is referred to as banding<sup>20, 32-34</sup> and is caused by interdendritic\* segregation during solidification<sup>20</sup>. The most common example of banding is alternate layers of ferrite and pearlite in carbon steels and in slowly-cooled alloy steels. Figure 2-12 show bands of pearlite (dark etched) and ferrite (light etched) in a grade X65 pipeline steel. This type of banding is thought to be caused by manganese segregation<sup>20, 32-34</sup>.

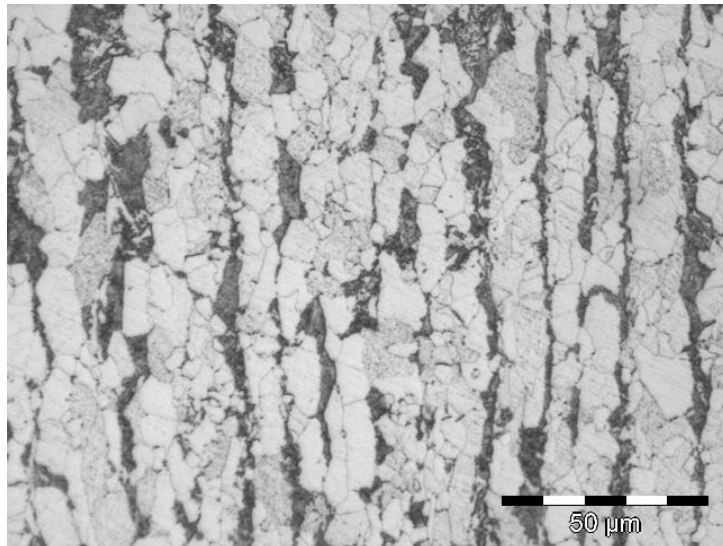


**Figure 2-12. Micrograph showing bands of pearlite (dark) and ferrite (light) in as-received X65 pipeline steel. Average band centre to centre (c/c) spacing is 19 μm**

According to Verhoeven<sup>34</sup>, there are two types of banding in hypoeutectoid steels (carbon content less than 0.87%): structural and chemical banding. Pearlite/ferrite banding is an example of structural banding in carbon steels and in alloy steel, other phase combinations could be found depending on the cooling rate. Structural banding is produced as result of difference in transformation temperatures between alternate bands but chemical banding occurs due to etching effects. Some etchants are capable

---

\* 'During solidification, heat evolution raises the temperature at the solid-liquid interface, but protruding solid fingers may extend into the cooler under-cooled region and their growth is accelerated. Radial arms are formed which send out secondary arms at right angles to them. This is repeated until a fir-tree type of crystal is produce, known as dendrite' E. C. Rollason, 4<sup>th</sup> edition 1973, p. 60.

of distinguishing regions of higher or lower concentrations. For instance, Stead's etchant (10 g cupric chloride, 40 g magnesium chloride, 20 ml hydrochloric acid and 1000 ml ethanol\*)<sup>35</sup> causes high phosphorus (P) regions to appear white relative to lower P regions: 'Therefore, bands appear in structures that are 100% martensite or 100% bainite'<sup>34</sup>.

The severity of the banding developed in a rolled product depends on a number of complex factors: (1) composition: banding is usually noticeable only at carbon contents of 0.1 to 0.5%. Banding cannot be observed in the absence of either pearlite or ferrite; some reasonable volume proportion of the two is necessary to make apparent. Banding is also favoured by high concentrations of P, Mn, O, Si and N, although the presence of none of these elements is necessary for its development. (2) The tendency for banding to develop seems to depend markedly on steelmaking and ingot practice. As a result, severity of banding may vary considerably from plate to plate within a heat, or even from one section to another in a single plate. It is found with modern steelmaking practices that severe banding is likely to be present only in steels with high manganese contents. The only feature that can be correlated directly with banding is the segregation structure developed in the original ingot. The ferrite-rich cores of the dendrites in the ingot roll out to become ferrite rich bands in the final product, and the pearlite-rich interdendritic areas roll out to become pearlite-rich bands. Segregation of carbon itself cannot be responsible for formation of ferrite-pearlite bands. Carbon has such high diffusivity in austenite that it would be distributed quite uniformly in the austenite which, when transformed during cooling, produces the bands of ferrite and pearlite. However, segregation of any element which significantly raises or lowers the  $A_{r3}$  temperature could be responsible. These elements include Si, P and Mn. Electron probe microanalysis indicates that the main segregated element in banded steels is manganese. The austenitizing treatment can also have an influence on the severity of banding developed during slow cooling: the banding tends to disappear when the grains of austenite are over grown, due to the use of a high austenitizing treatment<sup>36</sup>.

---

\*Dissolve cupric chloride in a minimum quantity of hot water (10-15 ml); add magnesium chloride and dissolve; add ethanol, then hydrochloric acid.

### **2.4.1 Effect of banding on mechanical properties of steel**

Microstructural banding contributes to the anisotropy of mechanical properties in steel plates<sup>37-39</sup>. A number of investigations have been carried out in the last five decades to understand the effect of banding on the mechanical behaviour of steels:

- The behaviour of banded and homogenized microstructures of low carbon steel was compared and no difference was found in impact properties below the transition temperature. Although, at the testing temperature for ductile fracture, both longitudinal and transverse energy absorption were higher in the non-banded specimens (Owen et al. in<sup>32</sup>)
- Grange<sup>37</sup> also found that homogenization of 0.25 % C steel with very low inclusion content markedly improved its ductile fracture properties and anisotropy due to banding. However work carried out by Spitzig<sup>38</sup> on 0.2 % C steel with aluminium addition concluded that pearlite banding has no significant effect on reduction of area or Charpy shelf energies. Both studies concluded that non-metallic inclusions have much greater effect on directionality of mechanical properties in impact than does banding.
- Effects of band spacing on tensile properties have been studied on artificially banded steel austenised at 850°C and cooled at a rate of 0.6°C/s. The work revealed that the tensile strength increased with increasing band spacing<sup>32</sup>.

### **2.4.2 Effect of banding on crack propagation**

It is easier for a crack to run parallel to bands than normal to them and so banding should be avoided in applications where lamellar tearing is possible<sup>20</sup>. Lamellar tearing is a common type of defect in the pipeline industry that is caused by banding. Pearlite bands can reduce the resistance of steels for hydrogen-induced cracking<sup>40</sup>. Microcracks aligned parallel to the major rolling direction have been observed in pipeline steel cathodically charged with hydrogen<sup>41</sup>.

### **2.4.3 Removal of banding**

A number of attempts have been made over the past five decades to understand banding formation and its removal in steels<sup>32, 33, 37-39</sup>. Grange<sup>37</sup> succeeded in

eliminating microstructural banding in 0.25% carbon, 1.5% manganese steel by soaking the steel for ten minutes within a temperature range of 1315 to 1345 °C and then air cooling. The steel was subsequently normalised at 900°C to obtain a microstructure similar to that prior to the treatment but without banding. The author also observed that, for a variety of carbon and low alloy steels, heating above or below this temperature range does not increase the overall efficiency of band removal. Spitzig<sup>38</sup> also applied Grange's method and completely removed banding in a 0.2% C, 1.0% Mn steel. Grange and Spitzig both concluded that band removal reduced anisotropy in the steels. Pearlite-ferrite banding was also removed in a semi-killed mild steel plate ( 0.2% carbon ) by quenching from the austenitizing temperature and then tempering at an appropriate temperature to obtain 'an adequate toughness without the return of banding in the form of temper banding'<sup>39</sup>. Thompson and Howell<sup>33</sup> studied banding in a steel containing 0.15% C and 1.49% Mn and concluded that slow (furnace) cooling yields intense banding and fast (air) cooling gives less intense banding. The authors also noted that in a steel with similar composition to that investigated, banding was not observed for a cooling rate of 5°C/s and banding disappears when the austenite grain size exceeds the spacing of the segregated bands by a factor of 2 or 3. However, Samuels<sup>36</sup> observed that banding removed by fast cooling or by large austenite grains formation can reappear if the material is subsequently austenitized and slowly cooled indicating that the segregation still exist.

Banding due to segregation of nickel, cobalt, molybdenum and titanium has been studied and a reasonably uniform homogenisation of cobalt segregation<sup>42</sup> was achieved by a solution treatment at 1150°C.

## ***2.5 Environment-assisted cracking***

Environment-assisted cracking (EAC)<sup>43</sup> is a general term used to describe failure of engineering materials that occurs by the initiation and propagation of cracks as a result of the synergistic interaction of mechanical stress and corrosive environment. EAC can be classified into four main categories: Stress corrosion cracking (SCC), Corrosion fatigue (CF), Hydrogen embrittlement (HE) and Liquid metal embrittlement (LME).



SCC has been defined by several authors as<sup>44-47</sup>:

- (a) fracture of alloys in certain chemical environments at static stresses considerably below that which would cause fracture in the absence of the particular environment<sup>44</sup>;
- (b) according to Ford<sup>46</sup>, fracture associated with a combination of a normally static tensile stress, environment and, in some systems, metallurgical condition, which lead to component failure due to the initiation and propagation of a high aspect ratio cracks
- (c) fracture in which the combination of stress, environment and susceptible material interact to lower the load-carrying capacity below that in inert environment<sup>45</sup>.
- (d) Stress corrosion cracking is a type of failure by which a normally ductile alloy develops cracks or suffers embrittlement<sup>47</sup>.

For SCC to occur three factors must exist simultaneously:

- tensile stress
- a specific aggressive environment and
- a susceptible microstructure

Stresses required to cause EAC could be small, but must be greater than a threshold value. The threshold stress for stress corrosion is defined as the stress above which cracks can initiate and grow for the specific test conditions. It is usually below the macroscopic yield stress, and much lower than that required to fracture the material in the absence of a corrosive environment, the stresses which are tensile in nature can be residual, externally applied, or a combination of both. Compressive stresses prevent the occurrence of EAC<sup>48</sup>.

Environments that cause EAC are usually aqueous and can be either condensed layers of moisture or bulk solutions. EAC is alloy/environment specific. That means, EAC is frequently the result of a specific chemical species in the environment. In the case of sodium hydrogen carbonate / sodium carbonate solution cracking of carbon steels, it is the  $\text{HCO}_3^-$  ion that was suggested to be largely involved in the crack development<sup>49,50</sup>. Also, an environment that causes EAC in one alloy may not cause it in another. In general, SCC observed in an alloy/environment combination results

from the formation of a film on the alloy surface. These films may be passivating layers, tarnish films, or de-alloyed layers, and decrease the rate of general corrosion, making the alloy desirable due to resistance to uniform corrosion in the environment<sup>48</sup>. While stress corrosion cracks propagate, the electrolyte conditions (electrochemical potentials, pH and solution chemistry) within the cracks often differ from the bulk electrolyte. Usually acidification, concentration of some species and nearer the free corrosion electrochemical potential exist at the crack-tip as compared to the conditions outside the crack<sup>48, 51</sup>.

The metallurgical conditions of materials, such as microstructure and chemical composition have significant effects on their susceptibility to EAC. Bulk alloy composition could affect stability of the passive film and phase distribution. Interstitial and impurity elements could segregate to grain boundaries and cause local difference in corrosion rate. Inclusions, especially manganese sulphide, can cause local crack-tip chemistry changes as the crack intersects them<sup>43</sup>.

The history of EAC goes back to the beginning of the twentieth century in which reports were concerned with the “Season Cracking” of cold-drawn brass cartridge cases in an ammonia-bearing environment and much later on caustic cracking of riveted boilers<sup>7</sup>. Since then EAC has received wide spread attention from researchers. EAC failures in industries have increased rapidly. That may be attributed to the use of new materials, such as corrosion-resistant alloys and high strength materials in a wider range of corrosive environments, and under more demanding loading conditions. The use of new test methods and advanced monitoring and controlling equipment as well as an increase in research activities in this field has revealed more combinations of alloys and environments which can give rise to EAC.

EAC poses a serious threat to engineering structures since it can occur at stress levels within the range of the design stress. It can initiate and propagate with little outside evidence of corrosion and with no warning a catastrophic failure can occur. The environment-assisted cracks frequently initiate at surface flaws that either pre-exist or are formed later during service by corrosion, wear and so on. Crack propagation can either be intergranular or transgranular (Figure 2-13); sometimes both types of cracking are observed on the same fracture surface. Intergranular is where the crack

propagation follows grain boundaries, and transgranular is where the crack propagation cuts across grains.

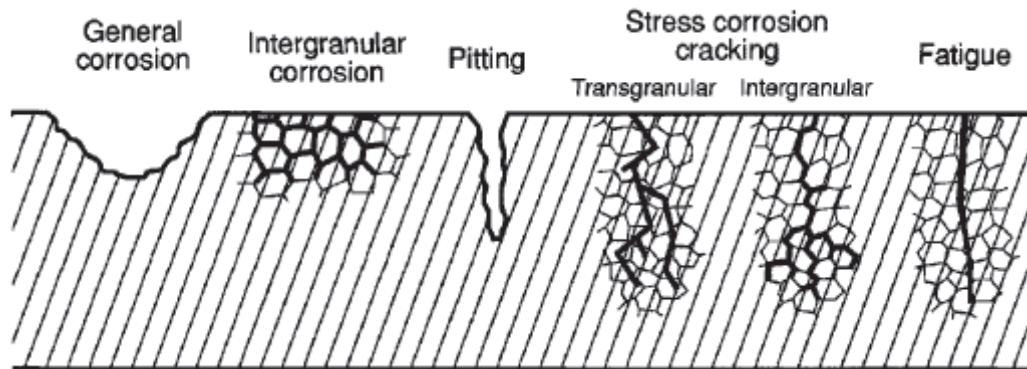


**Figure 2-13. Schematic showing modes of corrosion including transgranular and intergranular cracking<sup>52</sup>**

SCC of pipelines buried in the ground was first recognised over forty years ago in the U.S.A. and has now been experienced in several countries throughout the world. The countries include Australia, Canada, Iran, Pakistan, Saudi Arabia and the former Soviet Union<sup>53,54</sup>. There are two forms of SCC in pipelines: the classical form involving intergranular cracking due to the presence of concentrated carbonate / hydrogen carbonate solution with pH ranging from 9 - 11 and the transgranular cracking that is caused by a carbon dioxide containing, dilute ground water of relatively, low pH (~ 6.5)<sup>2</sup>. The two solutions are linked in that the high pH solution may be generated as a result of conversion of the low pH solution. The latter environment will remain only if the cathodic protection generates insufficient hydroxide ions to convert the free carbon dioxide to hydrogen carbonate or carbonate<sup>4</sup>.

The features of high pH intergranular SCC of high pressure buried pipelines are multiple cracks initiating from the soil side and mostly towards the bottom of the pipe. Such cracking has been observed in a wide range of pipe sizes and steel compositions, with coal tar, asphalt and tape coatings, and even on a few old lines buried without a coating, early field data showed no relationship of the incidence of cracking with soil type and all pipelines were cathodically protected at the time of failure. The solutions found adjacent to the pipes at the failure locations (including beneath coatings) had a pH range of 9.6 – 12.3 and predominant anions in the

solutions were carbonate and hydrogen carbonate with traces of chloride and nitrate in three cases. The major cation in all cases analysed was sodium. Failures have occurred in lines where the hoop stresses ranged between 46 – 80 % SMYS, all but one being in excess of 60 %, while cracking has in several instances been associated with dents resulting from accidents. Temperatures have been reported as ranging from 10 – 60°C, but mostly above 35°C, at times when failures have occurred and the much greater incidence of SCC (over 90 %) within ~ 16 kilometres downstream of compressor stations is most probably a reflection of the higher temperatures in such regions<sup>55</sup>. The cracks have been reported to be associated with a black film which has been shown by X-ray diffraction studies, to consist of siderite and magnetite<sup>8</sup>. Iron carbonate has been identified in the black film of seven out of eight SCC failure analyses where X-ray diffraction was performed. In the eighth case, there were insufficient deposits on the fracture surface to conduct X-ray diffraction analysis. The SCC deposits were black in colour possibly because of contamination with magnetite as pure siderite is generally grey<sup>8</sup>.

The standard solution generally used for high pH SCC experiments is 1 M sodium hydrogen carbonate / 0.5 M sodium carbonate with a pH ~ 9.4. This solution was first used by Parkins in 1969 and has been extensively used in subsequent works by many researchers. According to Parkins these concentrations were arrived at on the assumption that heat transfer through the pipe wall could lead to a solution practically at saturation and crystals of sodium hydrogen carbonate have been observed in the region of SCC failures<sup>55</sup>.

CF failure is caused by cracks which form under the combined action of corrosion and fluctuating or cyclic stress. The boundary between SCC and CF is not clear especially for low frequency cyclic loading conditions in CF.

HE is the fracture or degradation in mechanical performance of alloys due to absorption of atomic hydrogen. The degradation is a result of the formation of internal cracks or loss of ductility associated with fracture<sup>56</sup>.

LME is an embrittlement of certain materials when in contact with some liquid metals which results from liquid-metal chemisorptions that induce reduction in the cohesive strength of atomic bonds in the region of a stress concentration.

### **2.5.1 EAC tests types**

The aim of EAC testing is to determine whether cracking will occur in a stressed specimen in a given environment over a test period. In some cases the objective is to predict service behaviour. Testing usually provides information more rapidly than can be obtained from engineering service experience and at the same time attempts to predict engineering service behaviour. Shortening the EAC testing period does not just save time and resources but can also improve the reproducibility and reliability of the data. The most common approaches employed to achieve these include the following:

1. High stress
2. Changes in structure or alloy composition
3. Slow continuous straining or cyclic stress
4. Pre-cracked specimen
5. Higher concentration of chemical species in the test environment than that in the engineering service environment
6. Increase temperature and
7. Electrochemical simulation

However, it is important to control these variables in such a way that the basic failure mechanism is not changed. Before undertaking a programme of EAC testing, an appropriate test method must be selected. The selection depends largely on the purpose of the test and the data required. While some tests attempt to reproduce engineering service conditions as closely as possible, others are designed to study the mechanistic aspects of EAC. In some situations, it is advantageous to use an actual structure component for EAC testing, but usually this is not practical. More often, it is necessary to select a smaller specimen to obtain the data required for engineering prediction. Various EAC test methods and their features have been discussed<sup>43, 57-59</sup>. The EAC test methods and specimens can be classified into three groups:

1. Static loading of a smooth specimen
  - Constant-load test

- Constant-strain test
2. Static loading of pre-cracked specimen (fracture mechanics)
    - Constant-load (K-increasing) test, for example Compact Tension (CT) specimen
    - Constant crack opening displacement (K-decreasing) test, for example T-type Wedge Opening Loaded specimen (WOL)
    - Constant stress intensity test, for example Contoured double cantilever beam specimen
  3. Dynamic loading of smooth or pre-cracked specimens
    - Slow strain rate test (SSRT)
    - Cyclic loading test (CF)

All testing can be conducted in uniaxial tension or bending. Each type of test has certain advantages and disadvantages. The test types may not give identical ranking for different materials and environments or enable the same conclusions to be drawn.

#### **2.5.1.1 Static loading of smooth specimen constant-load and constant-strain tests**

Constant-load and constant strain tests of smooth specimens usually take a long time but appear more realistic. The tests are conducted at various fixed stress or strain levels and the time to failure of the specimen in the environment is recorded.

#### **2.5.1.2 Static loading of pre-cracked (fracture mechanics) specimens**

The discipline of fracture mechanics can be employed to study the propagation behaviour of an environment-assisted crack. Fracture mechanics testing techniques are also used for evaluation of the effects of metallurgical or environmental variables on EAC where the specimen contains a sharp crack. One of the most common and relatively simple techniques for integrating fracture mechanics techniques for the evaluation of EAC is through the use of constant load or constant deflection specimens in combination with a pre-cracked specimen. In the case of constant load specimens, a load is applied to the fracture mechanics specimen using a dead weight load, by a hydraulic cylinder, or through a pulley or lever system to magnify the dead

weight load. The most common types of specimens used for evaluation of EAC are the compact tension specimen (Figure 2-14), pre-cracked double beam specimen (Figure 2-15) or single-edge notched bend specimen (Figure 2-16)<sup>60</sup>.

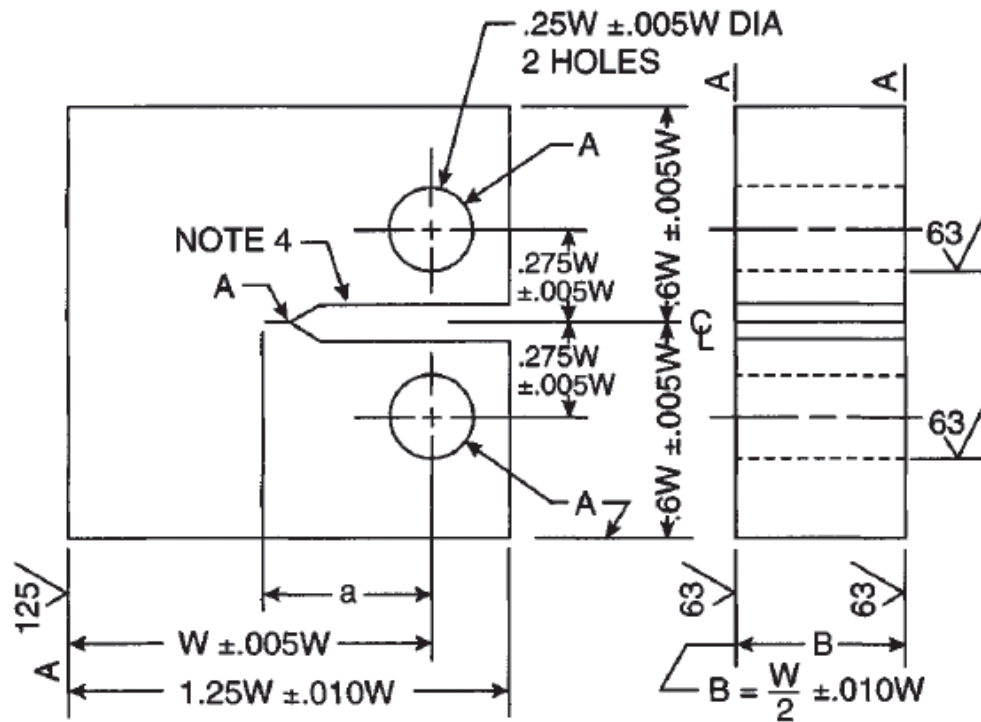


Figure 2-14. A compact tension specimen. Also referred to as single edge notch tension (SENT) specimen<sup>60</sup>

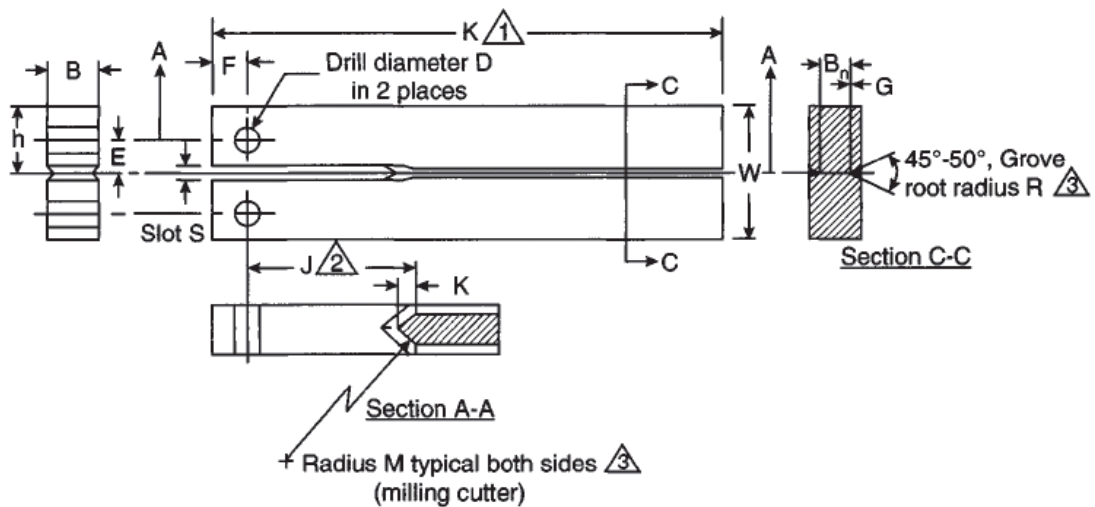


Figure 2-15. Pre-cracked double beam specimen. Also referred to as double cantilever beam (DCB) specimen<sup>60</sup>

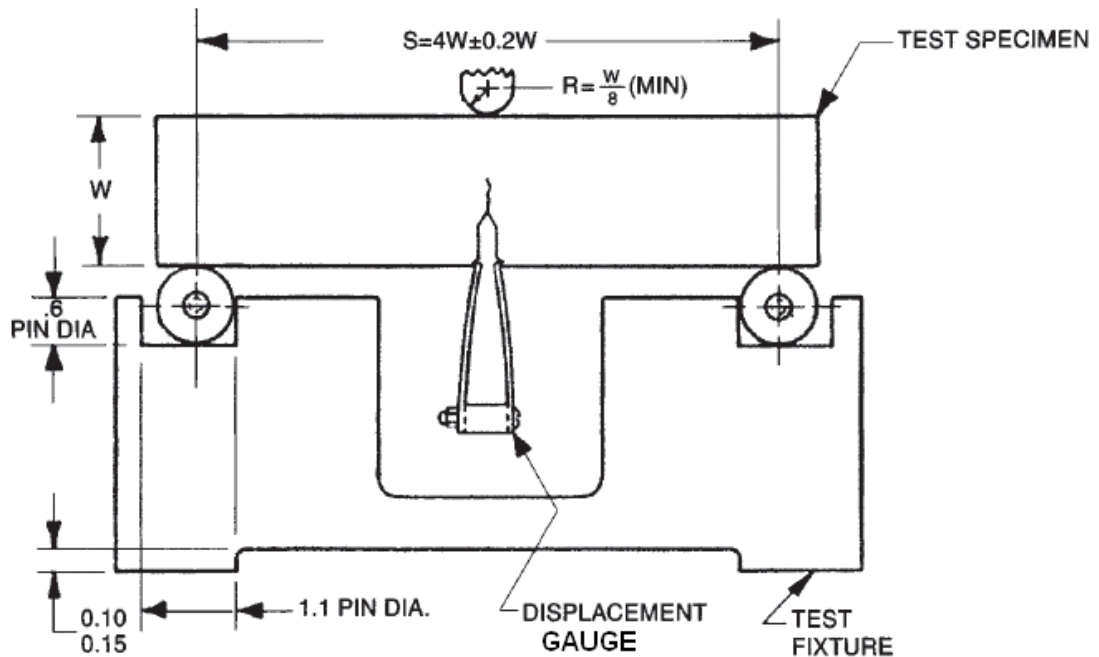


Figure 2-16. single-edge notched beam (SENB) specimen<sup>60</sup>

The specimens are pre-cracked or, in some cases, slotted to produce a crack-like defect that can assist in initiating EAC at high levels of stress intensity (K). Susceptibility is measured in terms of threshold stress intensity factor for EAC ( $K_{IEAC}$ ).  $K_I$  is called plane strain stress intensity factor which is a function of applied load, crack length and specimen geometry having dimensions of stress x length<sup>1/2</sup> which also uniquely defines the elastic stress field intensification at the tip of a crack subjected to opening mode displacements.  $K_{IEAC}$  is the stress intensity above which EAC will initiate and grow for the specified test conditions under conditions of high constraint to plastic deformation.  $K_{IC}$  is called plane strain fracture toughness factor which defines the critical value of  $K_I$  at which the first significant environmentally independent extension of the crack occurs under the influence of rising stress intensity under conditions of high constraint to plastic deformation. The stress intensity at the tip of the crack can be calculated using standard equations as given in ASTM E399<sup>61</sup>.



### 2.5.1.3 Slow strain rate testing

Slow strain rate test (SSRT) is a method for determining the susceptibility of an alloy to EAC. It is basically a tensile test conducted at low crosshead speeds typically ( $10^{-4}$  to  $10^{-7}$  cm/s)<sup>58</sup>. However, according to Parkins<sup>62</sup>, the absence of cracking in tests conducted at such rates should not be taken as an indication of immunity to cracking for a given system until tests have also been conducted at faster and slower strain rates. The slow speed is to allow sufficient time for the environment to attack the material although there seem to be an optimal strain rate for a given set of test conditions (Figure 2-17). The figure shows the effect of strain rate on stress corrosion susceptibility of pipeline steels in carbonate-bicarbonate solution at 79°C and three applied potentials. The susceptibility was measured in terms of the ratio of % reduction in area (RA) in the corrosive environment to that of an inert solution (oil). The effect of the corrosive environment is to embrittle (reduction in ductility) the steel. Other parameters for measuring susceptibility include, crack velocity, time to failure, and tensile fracture stress. In a SSRT experiment, a specimen submerged in a corrosive environment is uniaxially loaded to failure. The fracture is either produced by stress corrosion or by mechanical failure, or both. The principal advantages of SSRT are the speed with which the EAC susceptibility of a particular alloy and environment can be assessed and lower scatter in the data when compared with other EAC test methods. It also facilitates cracking in circumstances where, under constant load or constant total strain cracking is not observed or shows poor reproducibility, or takes an excessively long time. The additional advantage of SSRT over constant load or strain tests is that the test is not terminated after some arbitrary time, since the conclusion is always achieved by the specimen failure and the criterion of cracking susceptibility is then related to the mode of failure. SSRT is excellent for comparing the relative susceptibility of materials to EAC and for studying the influence of metallurgical variables on the susceptibility of an alloy; however, the test is not good for predicting actual in-service crack growth rates<sup>63</sup>.

In SSRT, ductility provides a convenient parameter for measuring EAC severity. Severe loss of ductility is also used to measure embrittlement due to cathodic charging of hydrogen in steel. Loss of ductility combined with cracking could be an

indication of SCC or of hydrogen embrittlement depending on the potential/pH regime. In reporting the results of SSRTs, the following information should be given:

- a description of the test material, including the composition, mechanical properties, heat treatment, microstructure, and type of product and section thickness from which the specimens were taken
- orientation, type, and size of the test specimens and their surface preparation and
- test environment including potentials, temperature, etc.

Figure 2-18 and Figure 2-19 show susceptibility of a grade X52 pipeline measured in terms of % RA and crack velocity, respectively. An addition of 1 %  $\text{Na}_2\text{CrO}_4$  (Figure 2-19), improved the resistance of the pipeline steel to cracking over the critical potential range in the sodium hydrogen carbonate / sodium carbonate solution. Other substances, for example like phosphates, has been suggested to be effective in reducing cracking tendency both in the hydrogen carbonate-carbonate solution and other cracking solutions such as hydroxide and nitrates<sup>5</sup>.

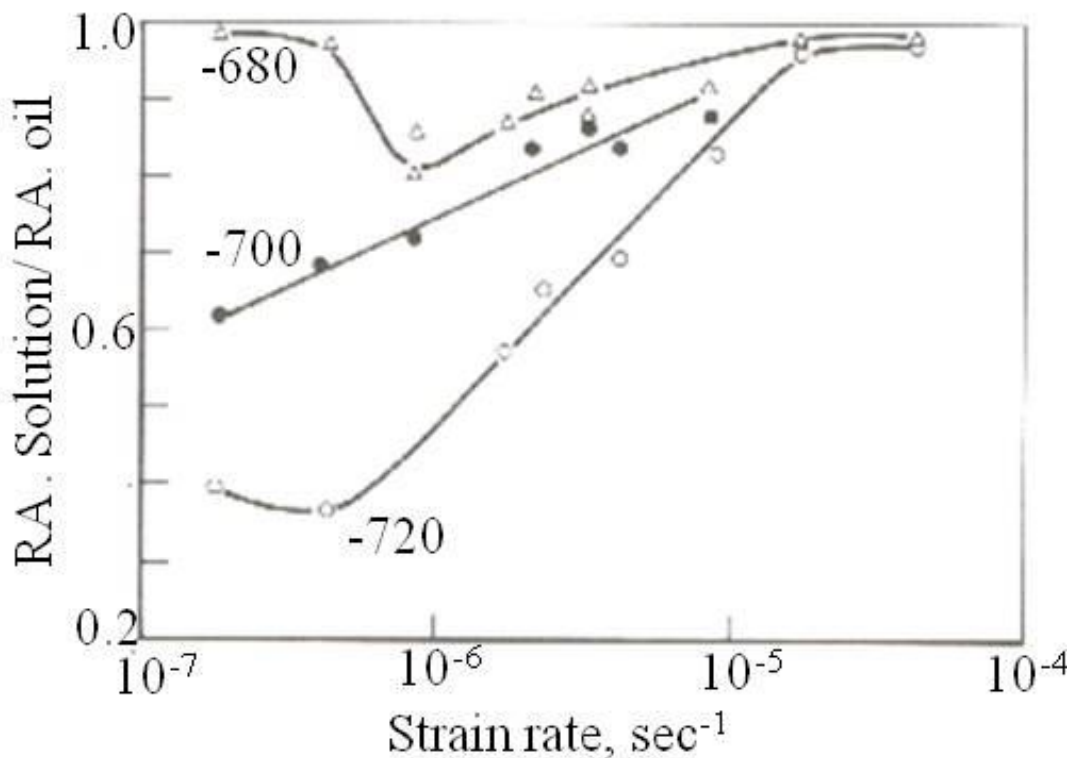


Figure 2-17. Effect of strain rate upon the stress corrosion susceptibility of a pipeline steel at 79°C 1M  $\text{NaHCO}_3$ /0.5M  $\text{Na}_2\text{CO}_3$  solution (Tensile test on plain specimen)<sup>62, 64, 65</sup>

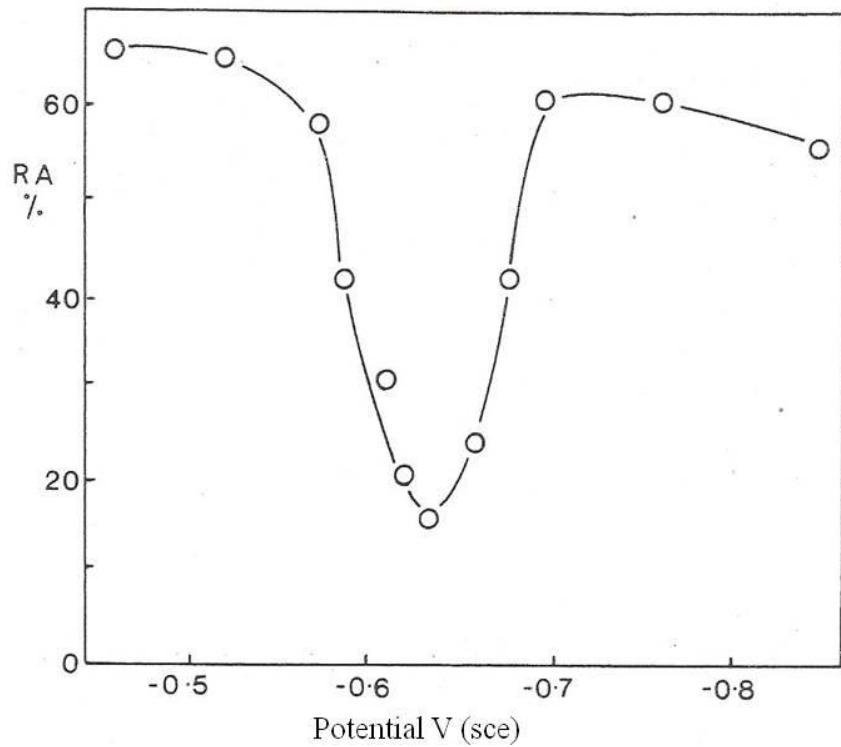


Figure 2-18. Slow strain rate stress corrosion test results for pipeline steel in 1M NaHCO<sub>3</sub>/0.5M Na<sub>2</sub>CO<sub>3</sub> solution at 75°C and various potentials. Increasing susceptibility to stress corrosion is associated with decreasing reduction in area <sup>5</sup>

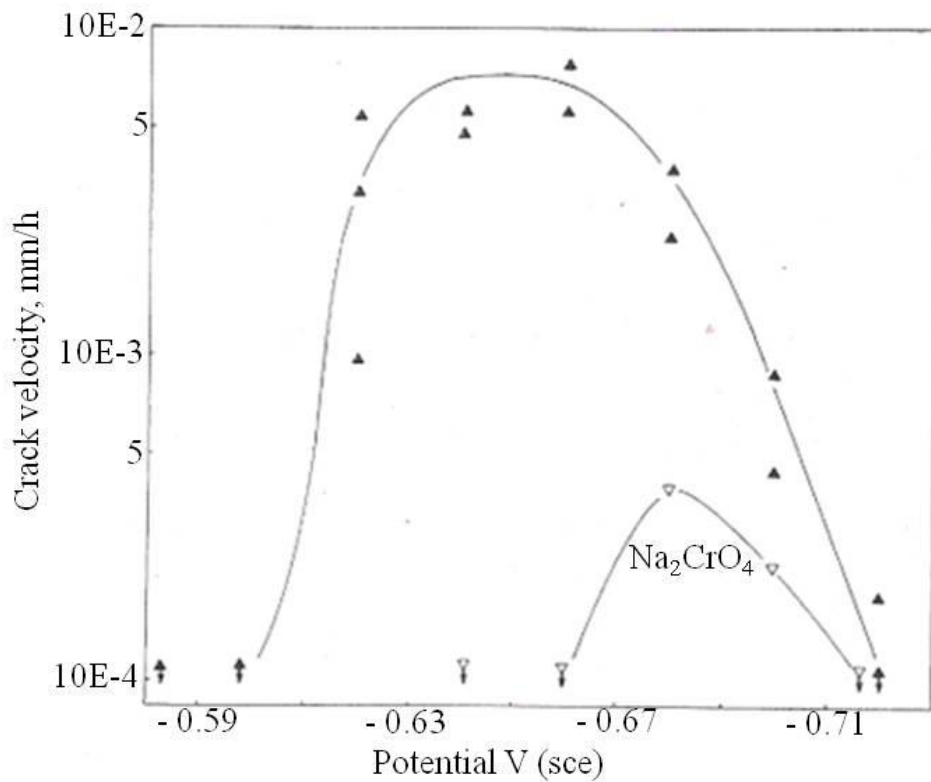


Figure 2-19. Stress corrosion crack velocities from slow strain rate tests on X52 grade pipeline steel in 1M NaHCO<sub>3</sub>/0.5M Na<sub>2</sub>CO<sub>3</sub> solution, with and without Na<sub>2</sub>CrO<sub>4</sub> additions, at 75°C and various potentials <sup>5</sup>.

## 2.5.2 Mechanisms of EAC

Development of quantitative predictive models of EAC depend on establishing a mechanism for the crack growth process and identifying the various factors that influence the extent of crack advance. Many parameters can influence the EAC processes, including<sup>48</sup>:

1. Environmental parameters : Temperature, pH, electrochemical potential, solute concentration and activity, solute species, pressure, flow rate, solution viscosity and so on
2. Material parameters
  - alloy composition, especially impurities element compositions such as sulphur and Phosphorus
  - inclusions, especially sulphide inclusions
  - residual stress
  - metallurgical condition: strength level, grain size, grain boundary precipitation and segregation
3. mechanical parameters
  - magnitude of stress or the stress intensity factor applied
  - stress state, plane strain or plane stress
  - the loading mode at the crack-tip and
  - crack geometry

There are numerous mechanisms proposed to describe EAC in aqueous solutions and it is impossible to use a single mechanism to cover all EAC phenomena. The problem is that environment-assisted cracking is dependent on the interaction of the localised environment at the straining material surface, the local crack-tip mechanics (stresses, strains and strain rates) and the local material characteristics and microstructure. They are different from the macroscopic parameters such as bulk environment and applied stress. Thus, there is a requirement to relate the local parameters which 'drive' the system to the known macroscopic parameters<sup>51</sup>.

The whole EAC process is generally divided into two succeeding stages, crack initiation and crack propagation. Precise separation of initiation and propagation stages is experimentally difficult. Crack initiation and propagation are related but different processes. Some cracks will cease growing if the environment, mechanical and material conditions are not met for sustaining crack growth at the crack tip, while some will continue to propagate. There are numerous mechanisms proposed to describe stress corrosion cracking based primarily on the effect of anodic reaction processes (anodic-dissolution mechanisms) and of absorbed hydrogen atoms (hydrogen embrittlement mechanisms). Parkins<sup>66</sup> suggested that different SCC mechanisms were arranged in a continuous stress corrosion spectrum, ranging from those in which the mechanisms were thought to be dominated by a dissolution process to those in which mechanical fracture due to stress, or strain, occupied a more important role in SCC propagation. He divided the spectrum into three zones from the mechanistic viewpoint for convenient discussion:

1. Pre-existing active paths – the idea of this mechanism is that stress corrosion cracking is associated with pre-existing features, either as segregate or precipitate at the grain boundaries, which are electrochemically different from the matrix. Thus, a local galvanic cell can be established between alloy matrix and the segregate or precipitate when exposed to the environment. The segregate or precipitate may act as an anode to be dissolved in the local cell or as an efficient cathode causing localised dissolution at the immediately adjacent matrix. Alloys having such features are likely to be susceptible to intergranular corrosion. Such structurally dependent attack usually cannot continue in the absence of stress or anodic polarisation. The role of stress or strain is to enhance and sustain the localised corrosion by cleaning the corrosion products out of the corrosion path or by breaking the film formed at the grain boundaries, resulting in crack growth along the boundaries, which is classified as intergranular stress corrosion cracking. However, stress or strain only plays a secondary role in the cracking process<sup>66</sup>.
2. Strain-generated active paths – in the absence of pre-existing active paths, or even in their presence if other conditions are satisfied, plastic strain may generate active paths by rupturing a protective film or by activating dissolution at emerging slip lines<sup>66</sup>. Many corrosion resistant alloys owe their

electrochemical inactivity to a relatively inert protective film that forms on the exposed surface of the metal, so that the active metal is separated from the corrosive environment. If the protective film is disrupted because of the localised plastic strain, the active metal surface is exposed and then attacked by the corrosive environment until the protective film can form again. Thus, the active path along which the crack propagates is cyclically generated as disruptive strain and protective film build-up alternate with one another. This mechanism of crack propagation is also called a film rupture mechanism.

3. Specific adsorption at sub-critically stress sites – It has been suggested that metal bonds at crack tips are weakened by adsorption of critical anions from solution<sup>66, 67</sup>.

Hydrogen embrittlement mechanism - this accounts for the electrochemical kinetics of hydrogen generation, the absorption of hydrogen atoms, transport and localisation of hydrogen atoms in the metal and the interaction of the material with the absorbed hydrogen atoms under conditions of localised stress and strain<sup>51</sup>. Cracking processes based on the hydrogen embrittlement mechanism are usually associated with cathodic polarisation or high strength alloys because a high triaxial stress in front of a crack-tip can be easily attained and thereby the thermodynamic possibility of hydrogen super-saturation near the crack-tip is more likely. The super-saturation can cause crack propagation. The hydrogen embrittlement mechanism is divided into two theories based on the effect of diffused hydrogen atoms in the lattices of steels:

1. Decohesion theory – an increase in hydrogen concentration in steels reduces the cohesive force of iron-iron bonds by forming iron-hydrogen bonds. The combined effect of reduction in the cohesive force and internal stress generated during the steel-making processes may lead to hydrogen embrittlement<sup>68</sup>
2. Hydrogen – enhanced localized plasticity (HELP) theory – in this mechanism, it has been proposed that elastic relaxation of dislocation – dislocation repulsion by interstitial hydrogen atoms is regarded as enhancing dislocation mobility leading to hydrogen embrittlement<sup>68</sup>.

Figure 2-20 schematically demonstrates two EAC mechanisms: film rupture/dissolution and hydrogen embrittlement. These two mechanisms are the most

popular mechanisms proposed in the literature. The mechanism of intergranular cracking of pipeline steels in high pH solution has been suggested to be dissolution related<sup>69</sup> whereas the mechanism of transgranular cracking of pipeline steels in both high (at more negative potentials) and low pH solutions has been proposed to be associated with dissolution and diffusion of hydrogen into the steels although the exact role of hydrogen in the cracking process remains tentative.

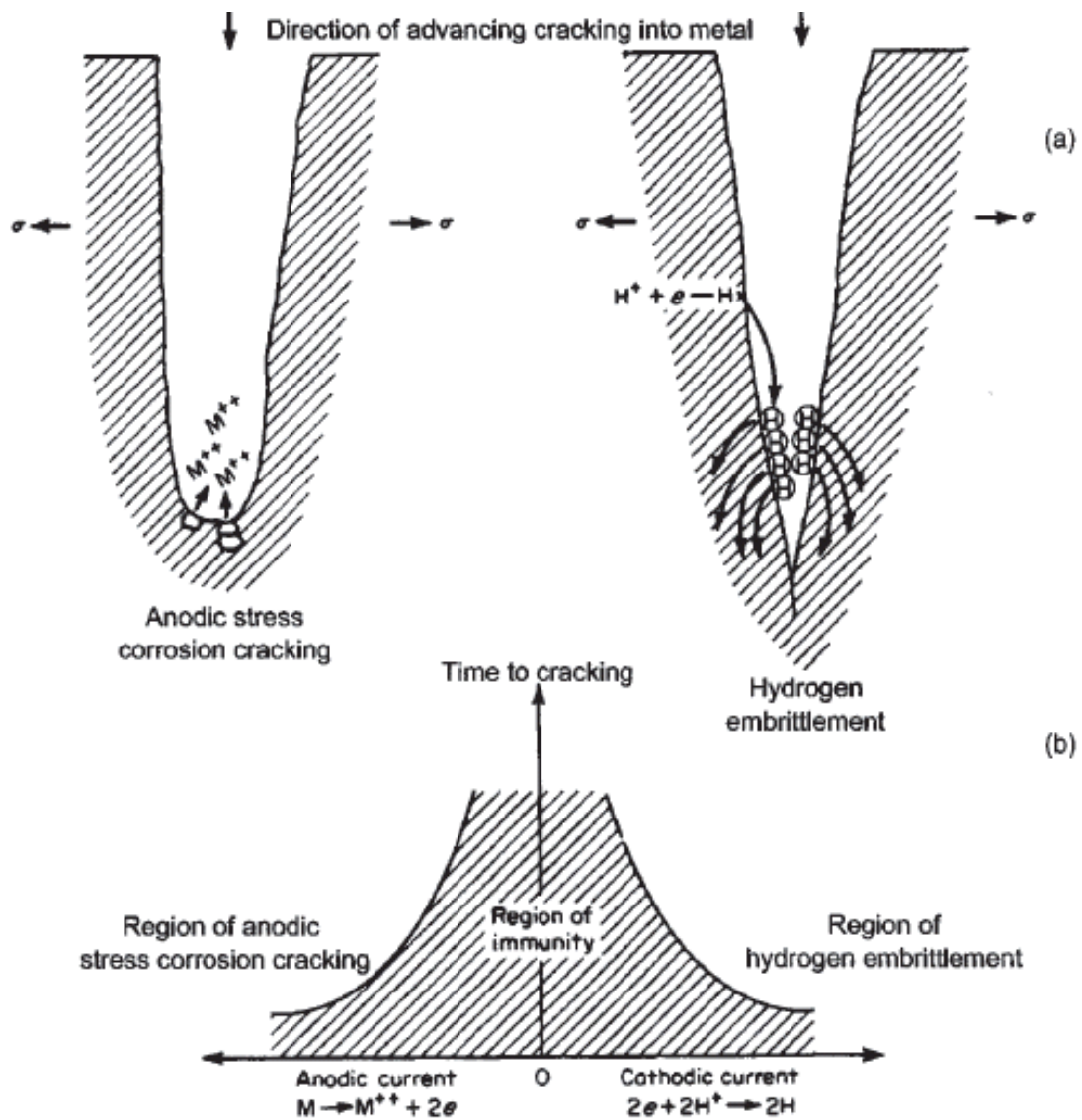


Figure 2-20. Schematic comparison of (a) anodic SCC and (b) hydrogen embrittlement cracking (HEC) mechanism<sup>56</sup>

### 2.5.3 Effect of microstructure on EAC

This review will focus on the effect of microstructure on the susceptibility of pipeline steels to SCC and HE in carbonate / bicarbonate solution. Parkins summarised that

the SCC resistance in many materials has been shown to be influenced by microstructure<sup>56</sup>. In general large grain sizes are often associated with relatively low threshold stresses for SCC, reflecting the influence of grain size upon yield strength, but increasing the latter by quenching and tempering treatments, where feasible, or heat-affected zones associated with welds, may result in higher crack growth rates.

Microstructural modification associated with cold work may also influence SCC resistance, but it is rarely the case that this can be used in plates in view of its implications on other directions<sup>56</sup>. Parkins argued that there has been no attempt made to fabricate pipeline steels for SCC resistance as opposed to their development for increased yield strength and fracture toughness. Hot rolled pipeline steels with ferrite-pearlite structures are more susceptible to SCC when compared with higher strength, controlled rolled and pearlite-reduced steels, but that is not simply a function of yield stress and moreover service failures have occurred involving control rolled steels.

An evaluation<sup>70</sup> of the resistance to EAC of two grades of X70 pipeline steels: one with ferritic-bainitic microstructure and the other with a bainitic structure, and a grade X80 with ferritic microstructure revealed that the ferritic microstructure of the grade X80 was least susceptible to EAC in sodium carbonate / sodium bicarbonate solution at 75°C and at an applied potential of – 650 mV (sce), whereas the ferritic-bainitic microstructure of grade X70 was the most susceptible microstructure. The evaluation also concluded that the grade X70 with bainitic structure and the grade X80 steels both appeared to have significantly better EAC resistance than conventional grades. In particular, the grade X80 exhibited a threshold stress for EAC that exceeds the normal operating hoop stress of the pipe. The three microstructures were evaluated using a tapered tensile specimen under cyclic loading. The assessment was made in terms of threshold stress for crack nucleation. The two microstructures of the grade X70 were the product of controlled rolling and accelerated cooling whereas the microstructure of the grade X80 was the product of controlled rolling without accelerated cooling. The contribution made by this evaluation is that the mechanical property requirements of a grade was met by two



different microstructures and that a principally bainitic or ferritic microstructure has a better resistance to EAC than a ferritic-bainitic microstructure.

The role of microstructure on EAC of pipeline steels has also been studied using the same approach as the evaluation mentioned above. A relative susceptibility to cracking of microstructures produced through different heat treatment processes: normalization, controlled rolling, thermomechanical-controlled processing and quenched and tempering. The study concluded that uniform microstructures were more resistant to SCC than mixed microstructures and that the presence of locally soft microstructures decreases resistance to SCC. The study also concluded that a ferrite-pearlite structure produced by controlled rolling is less susceptible to SCC than that produced by normalization<sup>3</sup>. This work<sup>3</sup> together with that of Christman<sup>70</sup> suggests that homogenisation of chemicals and phases in steels improve their resistance to EAC.

The susceptibility to EAC in sodium carbonate / sodium bicarbonate solution of a grade X70 pipeline whose microstructure was reported as acicular ferrite was assessed using slow strain rate tests. The susceptibility (measured in terms of loss in ductility) increased generally with decreasing potential in the range from – 200 to – 1500 mV (sce). Deep transgranular cracks were observed at cathodic potentials from – 1500 to – 840 mV (sce) and shallow, numerous and mainly intergranular cracks around – 700 to – 600 mV (sce). A rise in temperature from 30°C to 50°C increased the susceptibility to EAC in the anodic potentials but had no apparent effect at cathodic potentials<sup>71</sup>. This study suggests that the microstructure of grade X70 is more susceptible to the environment at potentials cathodic to the free corrosion potential (FCP) than potentials anodic to the FCP.

EAC susceptibility of an as-rolled, dual-phase steel (microstructure: 15 vol % martensite in a ferrite matrix) was compared with a commercial API-X65 pipeline steel with similar mechanical properties having a conventional pearlite (15 vol%)-ferrite microstructure. The former steel was found to be less susceptible to cracking in a 0.5 M sodium carbonate / 0.5 M sodium hydrogen carbonate solution. A selective attack of the martensite phase was observed and the phase was not aligned

in any direction but was randomly distributed, resulting in a microstructure that is more resistance to SCC<sup>72</sup>.

Wang and Atrens<sup>73</sup> measured the susceptibility to EAC of a commercial pipeline steel of grade X65 in terms of fracture stress across an applied potential range of – 1000 to – 450 mV (sce). The susceptibility across this potential range was divided into two regions based on mechanism: cracking at potentials more negative than – 800 mV (sce) was attributed to hydrogen embrittlement whereas the cracking within the potential range of – 700 to – 500 mV (sce) was attributed to an anodic dissolution. In the latter region, the lowest fracture stress occurred at the potential of – 600 mV (sce). The authors reported that the grade is more susceptible to hydrogen embrittlement than to cracking due to anodic dissolution. The susceptibility was measured at 70°C and the method used was a linearly increasing stress test (LIST), however, the microstructure of the grade X65 has not been report.

A constant extension rate tests (another name for SSRT) on cold-worked X52 pipeline steel in the carbonate solution at an applied potentials of – 650 mV (sce) showed that increasing the test temperature from 50°C to 75°C changed the mode of cracking from intergranular to transgranular cracking. The microstructure of the grade was reported as elongated alternate grains of pearlite and ferrite and an abundant presence of inclusions, largely manganese sulphide<sup>74</sup>.

Mitsui et al.<sup>75</sup> compares the susceptibility of low carbon steel with a pearlite / ferrite microstructure with HAZ microstructures produced with three different methods of welding and concluded that the resistance of the HAZ microstructures to intergranular SCC is higher than that of the parent metal. This suggests that the welding heat improved the as-received microstructure. The test solution was the sodium carbonate / sodium bicarbonate solution at 80°C. The susceptibility to SCC was found to be highest at a potential of – 675 mV (sce). The SCC region was predicted using potentiodynamic polarisation curve.

## Chapter 3 : EXPERIMENTAL

### 3.1 Material specifications

Three steel pipes of different grades were used in this research. The first two were American Petroleum Institute (API) grades, X65 and X80. The third was one of the new generation X100 steels<sup>41</sup> that are being developed for high pressure applications and for the approval of API. The pipes were produced using the ‘UOE’ method (Figure 2-4). The dimensions of the as-received pipes are shown in Table 3-1.

Table 3-1. Pipe dimensions

Grade	Diameter (mm)	Wall thickness (mm)
X65	812.8	9.4
X80	1219.0	13.8
X100	914.4	15.3

#### 3.1.1 Chemical compositions and mechanical properties

The chemical compositions, the weldability units and the mechanical properties of the steels in as-received conditions are shown in Table 3-2, Table 3-3 and Table 3-4. The chemical compositions lie within the code specification, API 5L. The details of how to calculate the weldability units CE and Pcm were given in section 2.3.3. The mechanical properties were measured using a slow strain rate test (SSRT) with cylindrical tensile specimens cut from fabricated pipes with major axes oriented perpendicular to the major rolling direction. Grade X65 material was only used to study the effect of heat treatment on the formation and removal of microstructural bands of pearlite and ferrite.

#### 3.1.2 Microstructures of the as-received steels

10 mm cube blocks were mounted in bakelite, wet-ground with silicon carbide papers of various grades: P240, 600, 800, 1200 and 2500, polished on 6 $\mu$ m and 1 $\mu$ m diamond cloths lubricated with paraffin oil and then finally etched with 2% nitric acid in alcohol (nital).

**Table 3-2. Chemical compositions in weight % (balance is iron in each grade) of the as-received steels determined previously<sup>6,76</sup>**

Elements	X65	X80	X100
<b>C</b>	0.07	0.11	0.062
<b>Mn</b>	1.36	2.0	1.82
<b>Si</b>	0.19	0.5	0.16
<b>S</b>	0.002	0.003	0.002
<b>P</b>	0.013	0.02	0.011
<b>Ni, Cr, Mo, Cu</b>	<0.23	0.35	0.989
<b>Nb, Al, V, Ti</b>	<0.071	0.14	0.133
<b>N</b>	-	0.006	0.0041

**Table 3-3. Calculated weldability for the steels**

Weldability	X65	X80	X100
<b>CE</b>	0.342	0.489	0.479
<b>Pcm</b>	0.157	0.245	0.206

**Table 3-4. Mechanical properties of the steels in silicone oil at 75°C**

Grade	Yield stress, MPa	UTS, MPa	Elongation, %	Reduction in area, %
<b>X65</b>	494	582	17	76
<b>X80</b>	589	663	17	75
<b>X100</b>	785	796	11	79

The microstructure of the three steels viewed in three different directions: pipe circumferential face, transverse and longitudinal sections through the pipe wall are shown in Figure 3-1, Figure 3-2 and Figure 3-3. The top view in each of the figures indicates the microstructure of the circumferential face of the pipe whereas the side face and the front face of each of the cubes show the microstructures of the longitudinal and the transverse sections through the pipe wall, respectively. These three faces are labelled ‘CL’, ‘LT’ and ‘CT’, respectively. The grains in the faces ‘LT’ and ‘CT’ are elongated due to rolling whereas on the face ‘CL’ the grains are not elongated. The degree of grain elongation is severe in the major direction of rolling, the longitudinal direction.

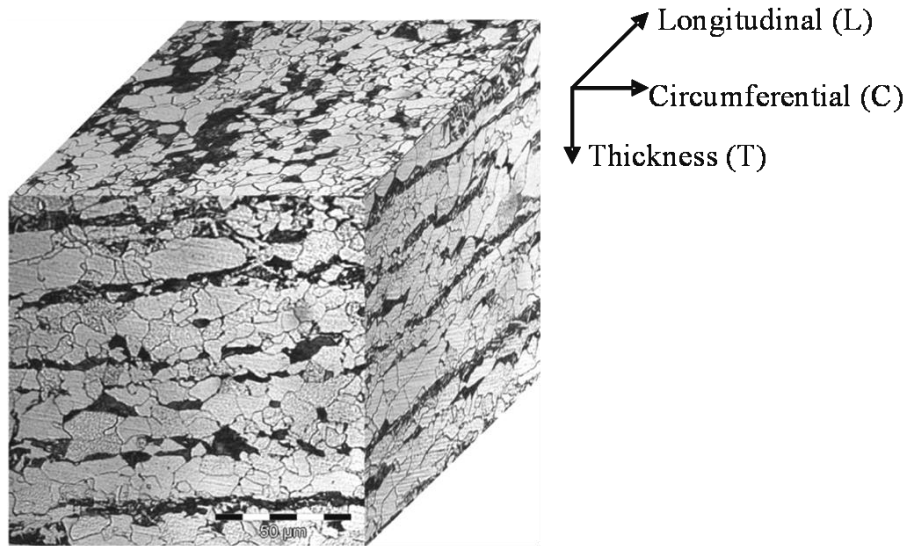


Figure 3-1. Microstructure of grade X65 steel viewed in three dimensions, 360x

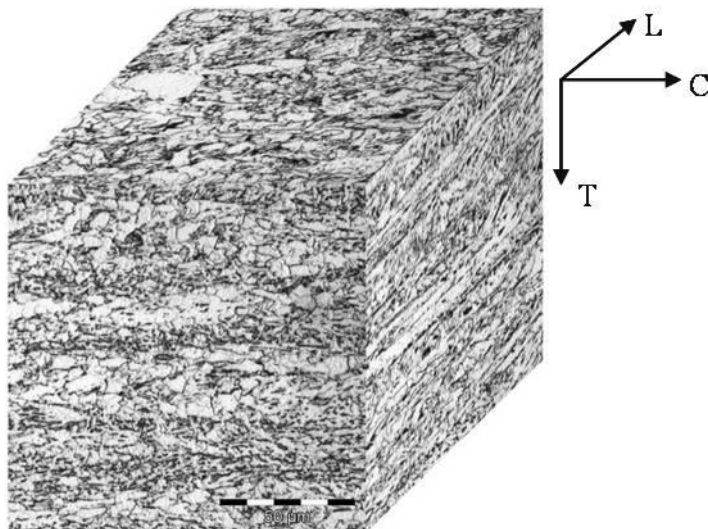


Figure 3-2. Microstructure of grade X80 steel viewed in three dimensions, 360x

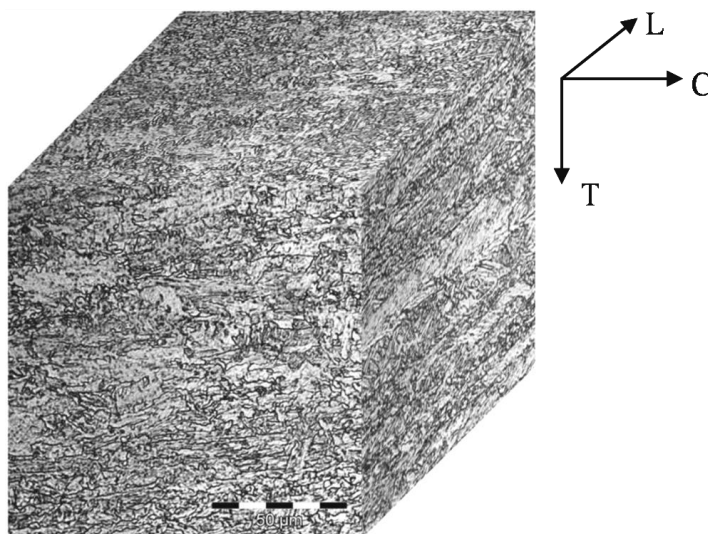


Figure 3-3. Microstructure of grade X100 steel viewed in three dimensions, 360x

### 3.1.2.1 Microstructure of as-received seam-weld heat-affected zone (HAZ)

The as-received low magnification microstructures of the seam-welds with their HAZs for the grade X80 and X100 steel are shown in Figure 3-4 and Figure 3-5, respectively. The seam-weld was made by a double submerged-arc process. It consists of two deposits of weld metal: one internal and the other external. The spot marks shown in the figures are indents left as a result of hardness measurements.

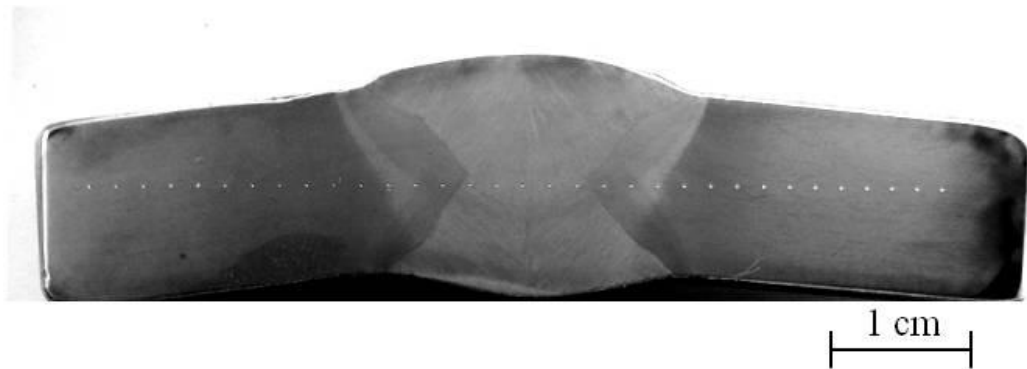


Figure 3-4. Seam-weld and HAZ of a grade X80 pipeline steel

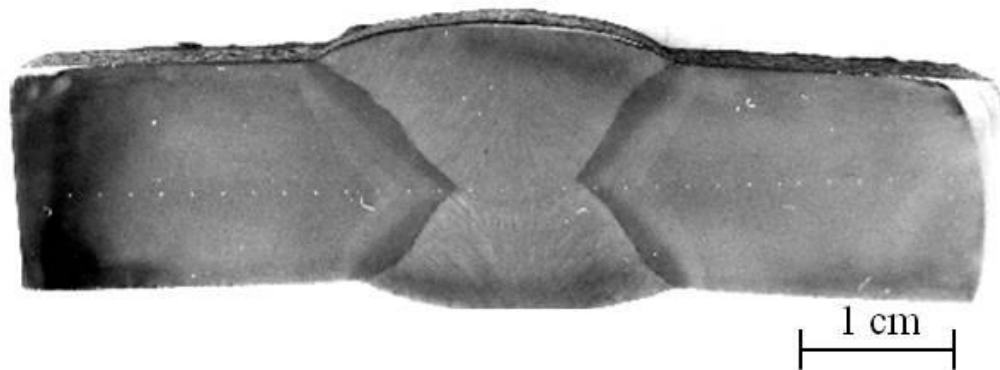


Figure 3-5. Seam-weld and HAZ of a grade X100 pipeline steel

### 3.1.2.2 Grain size and crack frequency measurement

The mean grain size was calculated by applying the Abrams Three-Circle Procedure to the grain size data<sup>77</sup>. Three concentric equally-spaced circles having a total circumference of 500 mm were drawn on a micrograph of known magnification and then the number of grain boundaries intersected by each circle was counted. The

mean grain size in mm was calculated by dividing the total circumference by the product of image magnification and the number of intersections counted. Further detail of this method can be found in ASTM standard, E112-96<sup>78</sup>. The number of secondary cracks per mm (crack frequency) on a gauge length was counted on a sectioned and polished specimen, using a travelling microscope at 100 times magnification.

### 3.2 Hardness measurement

The hardness<sup>77,79</sup> of specimens was measured with a Vickers diamond pyramid hardness tester and this was conducted according to the British Standard, BS EN ISO 6507-4:2005. All hardness values were taken from surfaces polished on 1 $\mu$ m diamond cloth. In performing the test, a square based pyramidal diamond indenter was forced into the surface of a sample using a 10 kg load (Figure 3-6). The load was applied within 10 and 15 seconds. The machine applied the load to the indenter by a simple weighted lever. As shown in Figure 3-6 the diagonals,  $d_1$  and  $d_2$ , were measured and averaged. The average value was used to determine the hardness from a table of hardness. The hardness may be calculated from the equation: Hardness (HV) =  $1.8544L/d^2$  where  $d$  = mean diagonal, mm and  $L$  = load used in kilogram. The hardness may be reported in various ways but in this case it is reported as  $Hv_{10}$ .

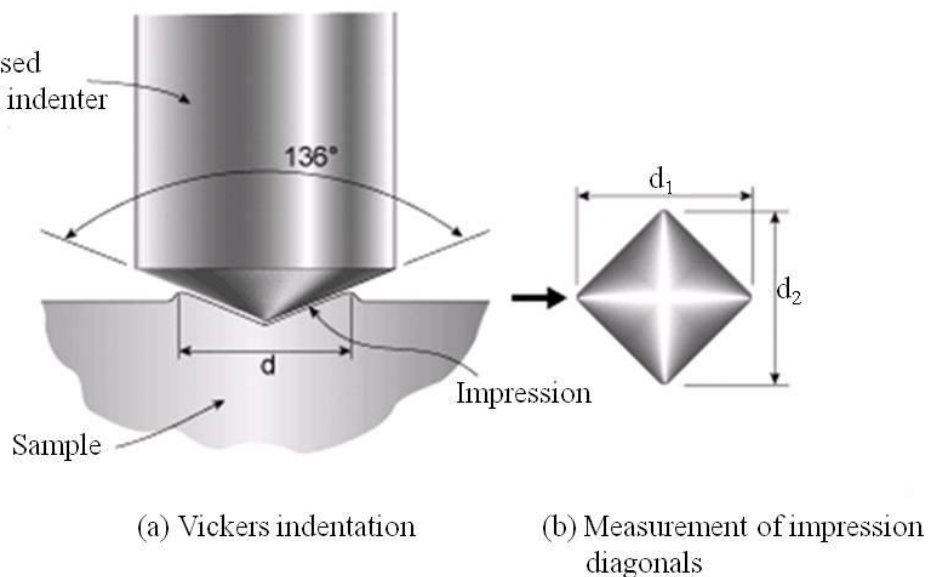


Figure 3-6. Schematic of Vickers hardness test method

### **3.3 Cracking environment**

#### **3.3.1 Test solutions**

Two solutions were selected for this research: 1 M sodium hydrogen carbonate / 0.5 M sodium carbonate (carbonate solution) and 4M sodium nitrate. Silicone oil (an inert liquid) was used as a control.

The carbonate solution was made by dissolving 84g of sodium hydrogen carbonate and 53g of sodium carbonate in one litre of deionised water at room temperature; which corresponds to 1M NaHCO<sub>3</sub>/0.5M Na<sub>2</sub>CO<sub>3</sub> (pH ≈ 9.5). This solution was chosen because carbonate solutions with a pH range of 9 to 10 are known to induce SCC and have caused the failure of a number of operating pipelines and it has been used by a number of researchers to examine the susceptibility of a base material and a weld zone to environment-assisted cracking<sup>2, 5, 6, 71, 80-82 73, 75</sup>. Tests were generally performed at a temperature of 75°C as the temperature is appropriate to over 90% of SCC failures in gas pipelines which occur within 16 kilometres downstream of compressor stations. Gas temperatures at the time of the failures have ranged from 15 to 61°C<sup>8</sup>. According to Parkins and Fessler<sup>5</sup>, there are indications that prior to the failures the temperatures were higher.

The 4 M sodium nitrate solution was prepared by dissolving 340g in one litre of the solution. One percent potassium dichromate (K<sub>2</sub>Cr<sub>2</sub>O<sub>7</sub>) was added to the sodium nitrate solution to inhibit general corrosion and so promote stress corrosion cracking<sup>83</sup> at the test temperature (75°C). Laboratory SCC tests in nitrate solutions have generally been conducted in boiling solutions<sup>84, 85</sup>. The shoulders of the specimens tested in the nitrate solution were wrapped with a polytetrafluoroethylene (PTFE) tape to minimise corrosion of the rough, unpolished shoulders.

#### **3.3.2 Applied potential**

For tests conducted in the aqueous solutions, various potentials were applied to the specimens using a potentiostat to simulate anodic attack, cathodic protection or over protection. A potential is normally applied to a pipeline as a protection against pitting



and general corrosion. A cathodic potential of  $-724$  to  $-824$  mV (sce) is considered adequate for protecting steel against pitting and general corrosion. The great majority of pipeline failures occurred on coated pipelines with pipe-to-soil potentials in the vicinity of failure ranging from  $-770$  to  $-1920$  mV (sce)<sup>5</sup> but the potential at the pipe surface would be less negative than these figures. The potential range considered in this work for tests in the carbonate solution was  $-500$  to  $-1100$  mV (sce). Nitrate solution SSRTs were conducted over the same potential range which include the reported SCC potential of  $-300$  to  $-400$  mV (sce)<sup>85</sup>. Only as-received grade X100 was tested in the sodium nitrate solution. Some tests in each of the solutions were repeated to check reproducibility.

### **3.4 Electrochemical test**

Polarization curves were generated using an electrochemical cell and a Solartron potentiodynamic data acquisition system. The cell was a multi-neck flask which contained  $\sim 300$  ml of the solution; two platinum foil counter electrodes and the steel specimen (the working electrode, a cylindrical specimen with a surface area of  $2\text{ cm}^2$ ) were immersed in the solution. The specimen was polished with silicon carbide paper grades down to P1200 and then cleaned with ethanol prior to testing.

The cell was connected to an external saturated calomel reference electrode (sce) by a salt bridge. Initially the specimen was held at  $-950$  mV (sce) and then subsequently swept in potential to  $-300$  mV (sce) at slow and fast sweep rates of  $0.1$  and  $10$  mV/s, respectively. The fast and slow polarisation curves can be used to determine the potential region where SCC might occur<sup>86</sup>.

### **3.5 Heat treatment**

The three steels were tested in both as-received and heat-treated conditions. Specimens were heat-treated for two reasons: to study the formation and removal of microstructural banding and to simulate seam-weld heat-affected zone.

### 3.5.1 Heating of rectangular bars

One end of each rectangular bar was heated to melting to simulate the weld HAZ: (1) the temperature profile, (2) the microstructural changes and (3) the cooling rate. The dimensions of the rectangular bars are given in Table 3-5 and the lengths of the bars were cut parallel to the longitudinal rolling direction.

**Table 3-5. Bar dimensions and heating times for grade X65**

<b>Bar</b>	<b>Dimensions (mm)</b>	<b>Heating time (min)</b>
01	9x17x244	~ 1½
02	9x17x158	5
03	9x17x158	12
04	9x15x244	12

One end of each bar was heated to melting with an oxy-acetylene flame while the other end was clamped in a vice, whereas Bar 04 was covered with furnace bricks during heating to reduce heat loss. Prior to heating Bar 03, a hole was drilled 60 mm away from the heated end and a thermocouple inserted into the hole to monitor the temperature. Intermediate temperatures between the two ends of the heated bars were also estimated based on the discolouration produced by oxide formation<sup>87</sup>. Two colours were considered: faint straw and light blue, which correspond to average temperatures of 204°C and 338°C respectively. Metallographic sections of the heated bars were prepared and the effect of the heating on the microstructure and the extent of the HAZs were studied.

### 3.5.2 Heat treatment of blocks and rods

The heating of the bars was found to be unsatisfactory for correlating changes in microstructure to a specific temperature and so blocks of average size 10 mm cube along with tensile specimen shoulders were heat treated at various temperatures in a tube furnace (Figure 3-7) equipped with a programmable controller. Specimens were cleaned with ethanol before placing in the furnace which had been preheated to the

required temperature. The furnace was purged with nitrogen gas during heat treatment to minimise surface oxidation. The modes of cooling used were furnace, air, oil and water.

The cooling rate of the tube furnace was measured with a thermocouple. The average cooling rate from temperatures between 1200°C and 1000 °C down to 725 °C was found to be ~ 0.1 °C/s. The cooling rate in air from a temperature of 1000 °C of a block was also measured by tightly inserting a thermocouple into a hole drilled in the middle of the block. The block was soaked for 20 minutes in the furnace and then cooled in air (Figure 3-8).

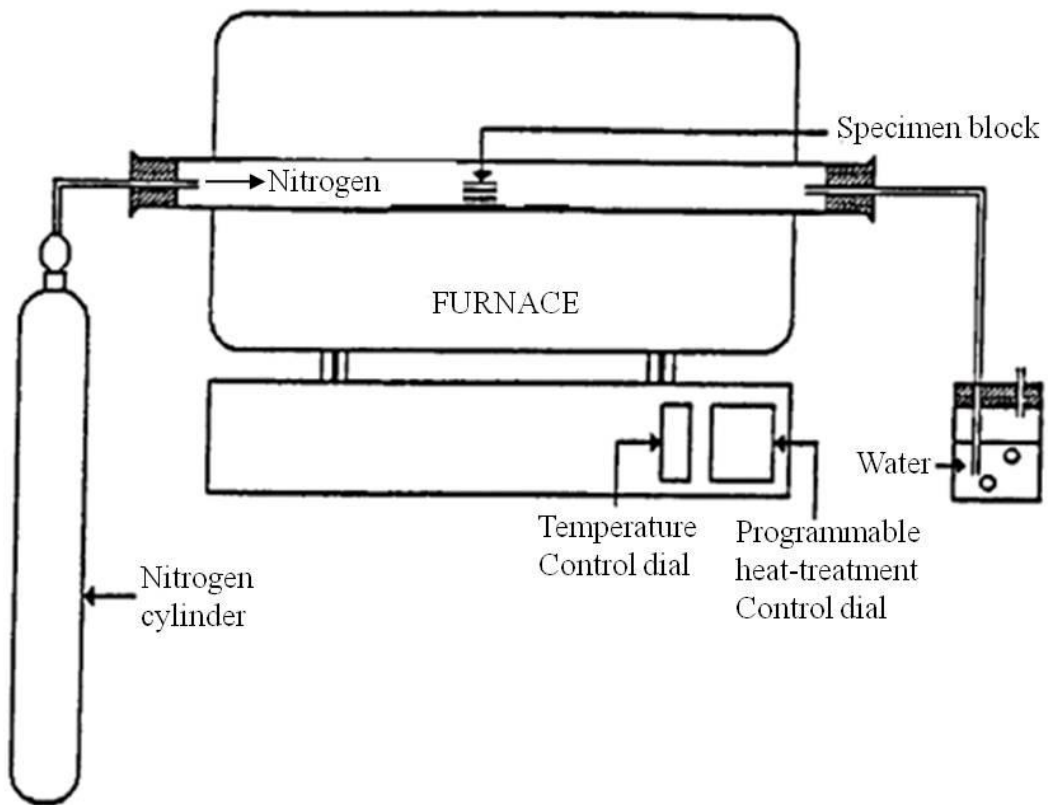


Figure 3-7. Schematic representation of the tube furnace used in heat treatment of specimens<sup>88</sup>

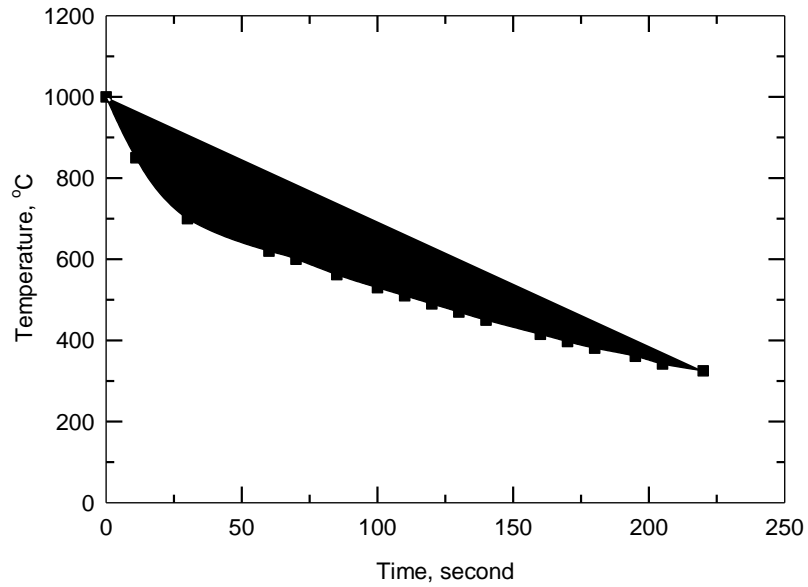


Figure 3-8. Air-cooling curve for 10 mm cube grade X65 steel after 20min at 1000°C

### 3.5.4 Estimation of transformation temperature

The minimum temperature required to transform the steel to austenite upon heating was estimated from the plot shown in Figure 3-9. It shows how the upper transformation temperature to austenite of hypo-eutectoid steel with a carbon content of 0.1% is lowered by increasing the concentration of manganese. Manganese is not the only element that shifts the transformation temperature but it has more effect than any other alloying element in pipeline steels (Table 3-2).

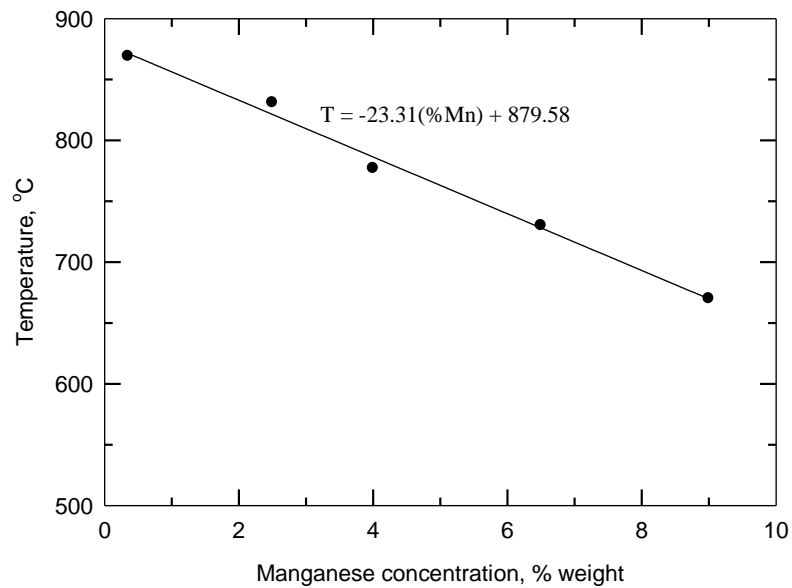


Figure 3-9. Variation of upper transformation temperature ( $Ar_3$ ) with manganese concentration for 0.1% carbon steel<sup>89</sup>

### 3.5.5 Estimation of time to remove banding

The time required to remove banding completely<sup>90</sup> was estimated from  $t = \frac{0.467l^2}{D}$  where  $l$  is half the centre to centre spacing of pearlite bands and  $D$  is the temperature dependent diffusion coefficient of the segregated element and is calculated using equation 2-1. Banding in pipeline steels is mainly caused by the segregation of manganese and carbon. The values of  $D_0$  and  $Q$  for manganese in austenite<sup>90,91</sup> are  $0.95 \text{ cm}^2/\text{s}$  and  $276 \text{ kJ/mol}$ , respectively and for carbon in austenite<sup>19</sup> are  $0.20 \text{ cm}^2/\text{s}$  and  $142 \text{ kJ/mol}$ . Figure 3-10 shows the estimated minimum time required to remove banding in the grade X65 pipeline steel with an average pearlite band centre to centre spacing of  $19 \mu\text{m}$ . This was determined by counting number of bands across a sample using a travelling microscope.

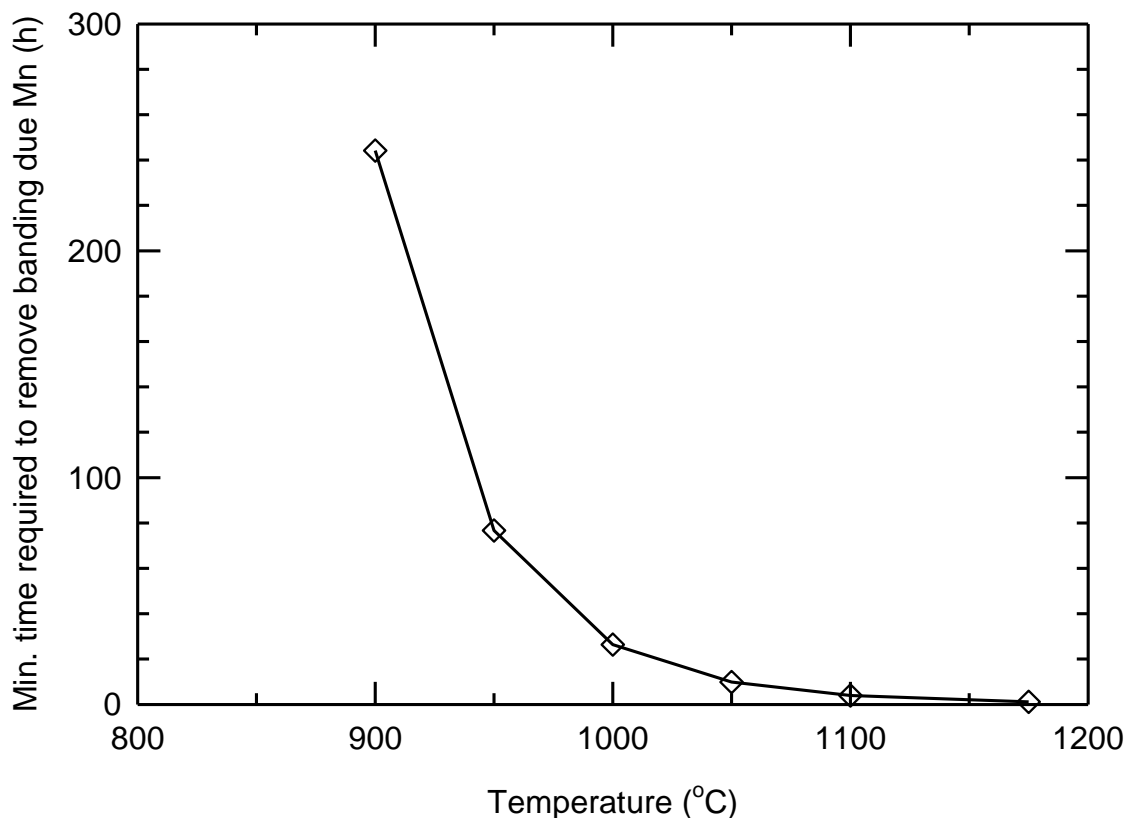


Figure 3-10. Estimated minimum time required to remove banding in grade X65 pipeline steel with an average pearlite centre to centre spacing of  $19 \mu\text{m}$ . Note: banding due to carbon segregation is removed in approximately five seconds at  $900^\circ\text{C}$

### 3.6 Slow strain rate testing

The environment-assisted cracking test using SSRT was carried out in accordance with ASTM Standard, G 129 – 00<sup>92</sup>. The SSRT was performed on a “relatively stiff-framed” tensile testing machine (Figure 3-11) designed at Newcastle University<sup>62</sup>.

The machine consists of a motor-driven crosshead in a load frame with a load cell to measure the load on the specimen continuously. Time is proportional to the crosshead travel, which is a measure of deformation or strain in the tensile specimen.

The result is a load versus time plot.

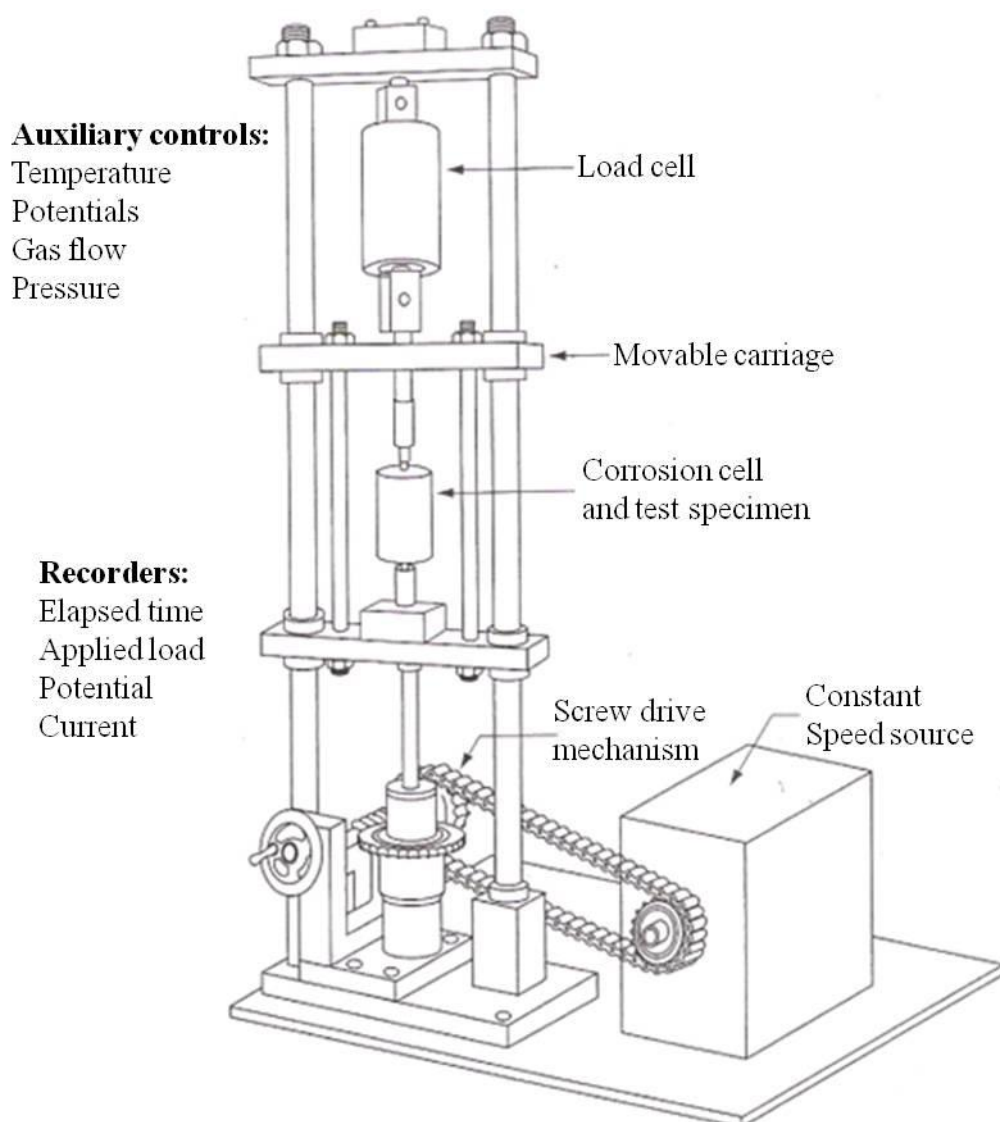


Figure 3-11. Slow strain rate testing machine<sup>7</sup>

The strain rate for most experiments was  $2 \times 10^{-6}$ /s but some tests were carried out both slower and faster than this. The stress corrosion test cells were 8 cm long, 4.6 cm internal diameter glass tubes, with external electric heating, and were sealed at each end with rubber bungs that permitted the insertion of the specimens, platinum-counter electrode, a condenser, a thermocouple and a thermostat each in a pocket (glass tube) immersed in the solution for temperature control and a conducting salt bridge led from the solution to an external saturated calomel reference electrode (sce). Potentials were applied to the test specimens using potentiostats and the test solution volume was approximately 85 cm<sup>3</sup>.

Cylindrical tensile specimens with gauge lengths of 12.7, 19.0 and 25.4 mm and a 2.54 mm diameter were cut from the walls of the as-received pipes. Specimens were cut with their major axis transverse or parallel to the longitudinal axis of the pipe. Prior to testing, the gauge lengths were polished with silicon carbide paper with grades down to P1200 and then cleaned with ethanol. Figure 3-12 shows a picture of a SSRT specimen 90 mm in overall length, 5 mm in diameter with a reduced gauge length of 12.7 mm length and 2.54 mm in diameter. It was threaded at both ends to allow attachment to the grips of the test machine.



Figure 3-12. SSRT specimen, length 90 mm

### 3.6.1 Interrupted SSRT

Several SSRTs were interrupted at different plastic strain levels to study: (1) whether cracks are formed before or after necking; (2) the effect of strain, temperature and pre-conditioning on the loss in ductility in the carbonate solution at an applied potential of  $-800$  mV (sce); (3) the effect of strain ageing on serrations - tests were interrupted approximately five hour after UTS and the specimen were then aged for 30 minutes at temperatures of 75, 150 and 300°C before re-loading them to fracture and (4) the mode of cracking at transition potentials where uninterrupted tests gave shallow cracks, less than the average grain size of the specimen, and the mode of

cracking was not apparent. These specimens were held for two days at a load just before UTS and then loaded to fracture.

### 3.6.2 Metallography

After each test the cracked specimens were sectioned, mounted in Bakelite (Figure 3-13) and polished for metallography. The maximum crack depths were measured using an optical microscope. Crack velocities were calculated by measuring the deepest secondary crack in any one specimen and dividing it by a time to failure measured from the fracture load (Figure 3-14). After crack depth measurements, the specimens were etched with 2 % nital solution and examined to determine whether the cracking mode was intergranular or transgranular.



Figure 3-13. Cross-section of a fractured specimen polished for crack measurement, 1.5x

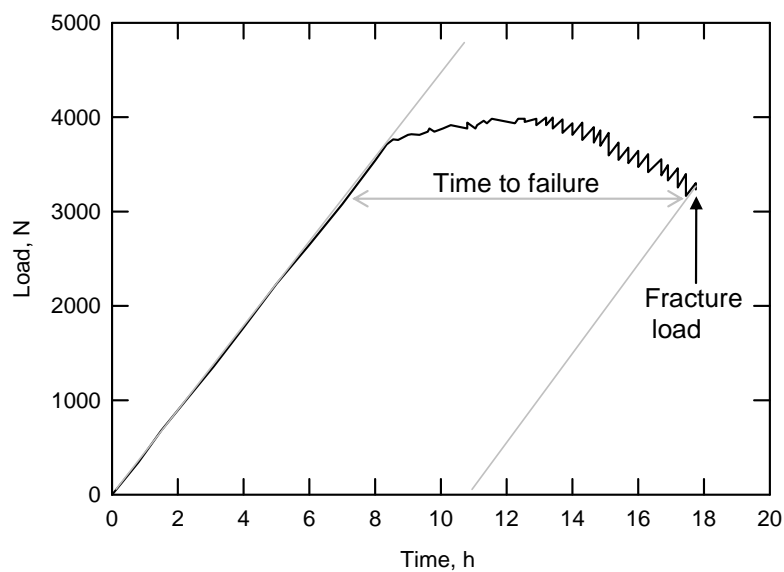


Figure 3-14. SSRT load-time plot of a test conducted on as-received grade X100 pipeline steel in the carbonate solution at 75°C and an applied potential of - 850 mV (sce)



### 3.6.3 Ductility measurement

The percent elongation (%EL) at fracture is the ratio of the total plastic elongation and the initial gauge length. Prior to testing, a reference spot mark was punched on each of the two shoulders of a specimen and the initial distance between the two spots was noted. After the test, the two pieces of a fractured specimen were laid together on a grooved block and then the final distance between the two spots was measured using a travelling microscope. The difference in distance before and after the test was taken as the total elongation in length of the specimen with the assumption that the total elongation occurred only on the gauge length. The percent elongation in length was also calculated by multiplying the time to failure measured from the fractured load (Figure 3-14) with the applied strain rate. The two measurements of the percent elongation in length were compared (Figure 3-15) and the one measured on the specimen was generally found to be longer. However, for 80% of the tests conducted on specimens with gauge lengths of 25.4 mm, the elongation on chart is equal to that of the specimen, indicating that the difference in elongation between the chart and the specimen is possibly connected to the size of the gauge lengths of the specimens and this agrees with literature that the value of percent elongation depends on the gauge length over which the measurement was taken<sup>93</sup>. The little gap between the two pieces also contributes to the difference, although they are tightly fitted together at the time of measuring the elongation. Therefore, Figure 3-15 strongly suggests that the above assumption that the strain is occurring only in the gauge length during straining of specimens is more accurate for specimens with gauge lengths of 25.4 mm than that of 12.7 mm. The specimen with gauge lengths 25.4 mm used in this case are all weld specimens with localised softer regions on both sides of a weld metal in the gauge lengths also contribute to the concentration of strain within the gauge lengths. So the total elongation measured on specimen for specimens with gauge lengths of less than 25.4 mm include that of the portion of shoulders within the two reference spot marks.

The percent reduction in area (% RA) was calculated by comparing the final cross-sectional area of the necked region at fracture with the original cross-sectional area calculated from the initial diameter of the gauge length. The final diameter of the neck at fracture was also measured with a travelling microscope.

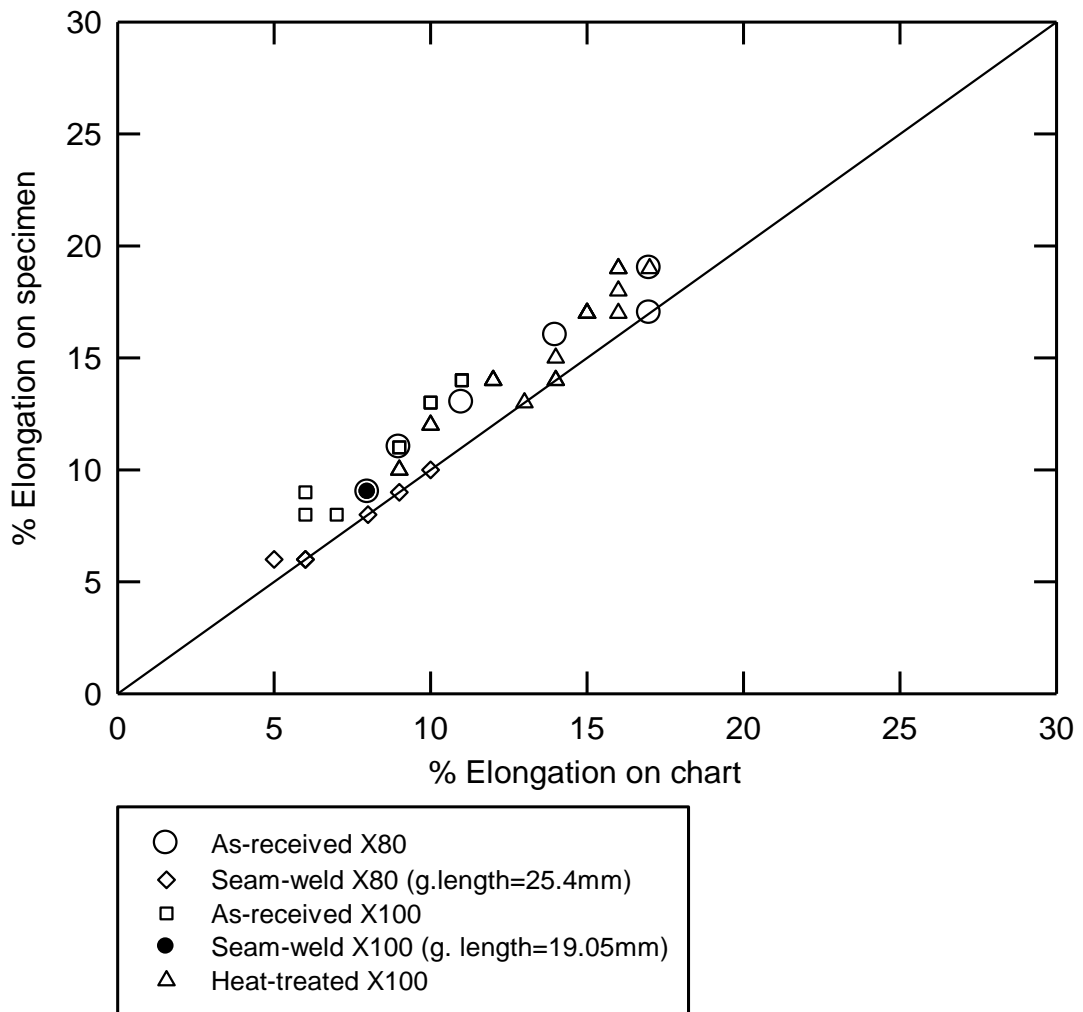


Figure 3-15. % Elongation measured from chart compared with that from the specimen

### 3.6.4 SSRT data analysis

The parameters used in measuring the susceptibility of the alloys to the corrosive environment include: crack velocity, embrittlement index, ductility (percent elongation in length and percent reduction in cross-sectional area of the fracture surface), ductility ratio and fracture stress.

The crack velocity (crack growth rate) was calculated from the deepest observed crack divided by the time to failure measured from the fracture load (Figure 3-14). Two types of crack were considered: primary and secondary. Primary cracks were measured on the fracture surfaces whereas the secondary cracks were measured on sectioned gauge lengths.

The embrittlement index<sup>71</sup> was calculated from  $(1 - \frac{D_c}{D_s}) 100\%$ , where  $D_c$  is the ductility in the carbonate solution and  $D_s$  ductility in silicone oil. The ductility ratio was calculated from  $\frac{D_c}{D_s}$ .

### **3.7 Fractography**

Examination and measurement of primary cracks on the fracture surfaces were made using a Hitachi S2400 Scanning Electron Microscope (SEM). Before SEM examination and measurement, corrosion products on the fracture surface were removed by ultrasonic cleaning in an 'ENDOX' solution (12% wt sodium cyanide in caustic) while under cathodic polarisation.

SEM structural images are obtained by scanning repeatedly over the surface area of a sample with a small electron beam spot of approximately 1  $\mu\text{m}$  in diameter. Slight variations in surface topography produce marked variations in the strength of the beam of secondary electrons ejected from the sample surface. The secondary electron beam signal is displayed on a monitor in a scanning pattern synchronized with the electron beam scan of the sample surface. Because of this, SEM allows the inspection of an irregular surface, unlike optical microscopes that require flat and polished surfaces. Information about primary cracks can be obtained from fracture surfaces. An additional feature of the SEM allows chemical mapping of a sample at microstructural scale. The incident electron beam of the SEM also generates characteristic wavelength X-rays on the sample surface in addition to the secondary electrons. The X-rays are used to identify the elemental composition of the sample under study<sup>19</sup>. SEM has three main components: vacuum column, detectors and a viewing console (Figure 3-16). A filament tip generates electrons at the top of the column and this is called the electron gun. Magnets in the column direct and focus the electron beam to travel towards the sample. The scanning coil makes the fine beam of electrons swing across the surface of the sample in synchronism with the spot of the display monitor.

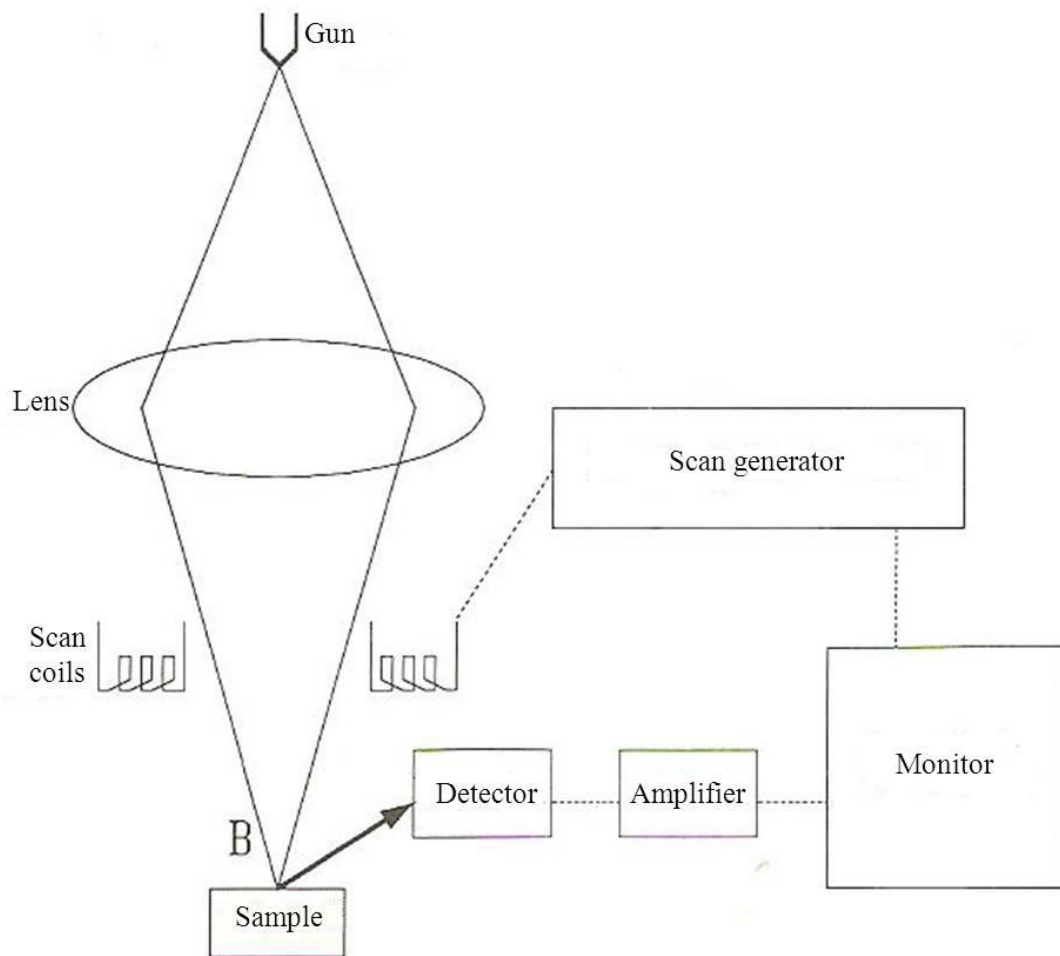


**Figure 3-16. Schematic of the parts of a scanning electron microscope<sup>94</sup>**

A detector monitors the chosen signal (for example, secondary electrons) and the brightness of the monitor spot is controlled by the amplified detected signal. If, for any reason, the intensity of the emitted signal changes across the specimen then the contrast will be seen in the image on the monitor. There are three types of detector: Secondary Electron, Back Scatter, and X-Ray. The secondary electron detector detects ejected surface electrons and converts to a digital image. The back scatter detector reads the pattern of electrons being reflected from the specimen. Softer or less dense areas will absorb electrons more than harder or denser areas. The back scatter detector does not show three dimensional structures. It is a flat image which shows atomic number contrast. The X-ray detector, or the energy dispersive X-ray Analyser (EDX), tells you what elements are present.

### **3.7.1 Elemental analysis**

The segregation of alloying elements, particularly manganese, across ferrite/pearlite bands was measured using Energy Dispersive X-ray (EDX) microanalysis. Line scan, spot analysis and chemical mapping were tried. EDX analysis is attached to the SEM as explained above. The SEM and EDX analyses were generally conducted at an excitation voltage of 25 kV and for the EDX spot analysis, a spot size of approximately one micrometer was used. Measurements were made on an unetched sample and the position of the pearlite/ferrite bands were marked with microhardness indents. Specimens were used unetched to avoid loss of alloy and formation of surface roughness due to etching<sup>95</sup>.

### **3.8 Film morphology test**

The types of films formed anodic to the free corrosion potential (FCP) on the surface of the as-received grade X100 steel, in the carbonate solution at 75°C and their morphologies were studied by growing films at various potentials on polished surfaces. The film growth time was four hours at each potential. The filmed surfaces were washed with DI water and dried prior to observation of the morphologies with a SEM. The comparison of the composition of the film formed at potentials of – 720 and – 850 mV (sce) using X-ray diffraction indicated that the film formed at the former potential contains more siderite than the latter.

#### **3.8.1 X-ray diffraction**

X-ray diffraction (XRD) analysis was employed to identify the composition of the film formed on the surface of the as-received grade X100 pipeline steel.

XRD is principally used for the study of crystalline minerals and may also be used for checking the presence of amorphous materials. X-rays diffracted in the surface layers of crystals and by studying the patterns of reflections, information about the structure of the material can be obtained (unit cell dimensions), and almost any mineral with a crystalline structure can be identified by searching a database of standard XRD patterns<sup>96, 97</sup>.

The machine used was a Phillips X'Pert Pro diffractometer fitted with an X'Celerator and a secondary monochromator. The X'Celerator serves to give a good quality pattern in a much shorter scan period than the time taken for a traditional diffractometer. The secondary monochromator eliminates fluorescent scattering from the specimen. Scans are carried out in 'continuous' rather than 'step' mode and take approximately 26 minutes per sample. In this work, the coating was scrubbed from the specimen surfaces into a sample holder. The holder was placed in the machine for analysis.

The XRD analyser produces X-rays by bombarding a target anode with high energy electrons emitted from a Röntgen X-ray tube. This X-rays beam is then directed at the sample and when the lattice planes in the sample reach the correct angle in relation to the beam then X-rays diffraction takes place in accordance with Braggs Law<sup>98</sup>:

$$n\lambda = 2d \sin \theta$$

where: n is an integer;

$\lambda$  is the wavelength of the X-rays;

d is the lattice space of the specimen measured in Angstroms and

$\theta$  is the angle of diffraction.

The resultant diffraction produces X-rays which are then detected, amplified and recorded as a digital signal on electronic media. The digital signal is displayed as an X-ray diffractogram type graph, with x-axis values of  $2\theta$  angle and y-axis values representing diffraction peak intensity. Interpretation of this graph involves identifying sets of peaks that are unique to specific lattice types and phases. Standard patterns have been compiled by the Joint Committee on Powder Diffraction Standards<sup>99</sup>. A first pass in peak identification can be undertaken with computer software designed to identify patterns by comparing the X-ray diffractogram with a comprehensive suite of standard patterns. If this automated method does not produce satisfactory results (i.e. does not identify major peaks, or assigns unlikely rare mineral species) the manual method of identification involves converting the  $2\theta$

value of the peak into a lattice spacing value (by means of a table), then identifying the major peaks and searching the published diffraction index for matches.

## Chapter 4 : RESULTS

### 4.1 Heat treatment

The 3-D microstructures of the three as-received pipeline steels studied in this research were shown in chapter three. In general, the microstructural details such as elongated grains and pearlite bands which may play a vital role in the corrosion (SCC in particular, Figure 4-1) and mechanical performance of the steels could be altered during welding. Therefore, a number of heat treatments were given to the as-received materials to simulate a seam-weld heat-affected zone (HAZ). The susceptibility to cracking of a few simulated microstructures and as-received seam-welds were compared with that of the as-received parent alloys using SSRT. The effect of a “spheroidised” structure (globular particles of carbide distributed in a matrix of ferrite) on environment-assisted cracking was also studied. The average grain size of the three steels (Table 4-1) decreases as the steel grade increases.

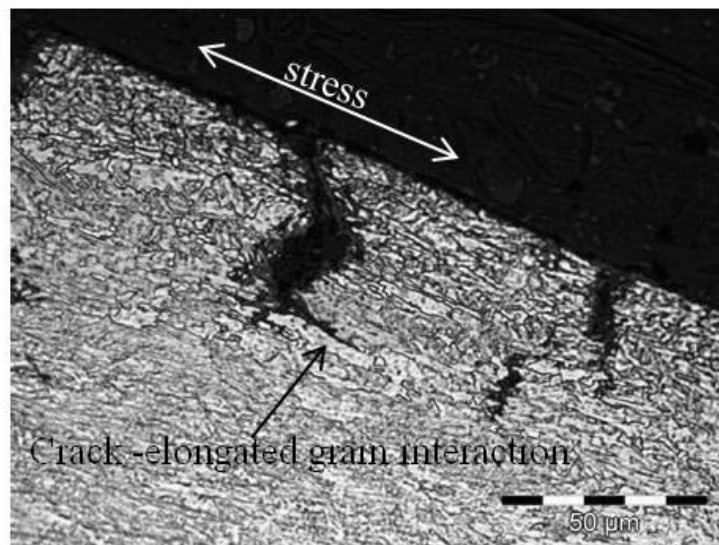


Figure 4-1. Elongated ferrite grains deflect growth of an IG crack in grade X100 steel

Table 4-1. Average grain size of the as-received pipeline steels

Grade	Average grain size ( $\mu\text{m}$ )		
	Face 'CL'	Face 'CT'	Face 'LT'
<b>X65</b>	4.9	6.8	6.2
<b>X80</b>	6.3	5.4	4.5
<b>X100</b>	2.7	3.1	3.2



### 4.1.1 Grade X65 pipeline steel

As stated in chapter three, the grade X65 was mainly used to study the effect of heat treatment on the formation and removal of bands of pearlite and ferrite. Its grains are coarser (Figure 3-1) than the other grades, so making it easier to study changes in microstructure due to heat treatment. The pearlite bands in hot-rolled steel plates form due to the concentration of carbon where manganese is high. EDX microanalysis consisting of: a line scan, spot, area and an elemental mapping was carried out and Figure 4-2 shows the result of a line scanned across the bands of pearlite and ferrite. The figure shows the distribution of manganese as intensity in counts per second (cps). A profile for silicon was also recorded as a control.

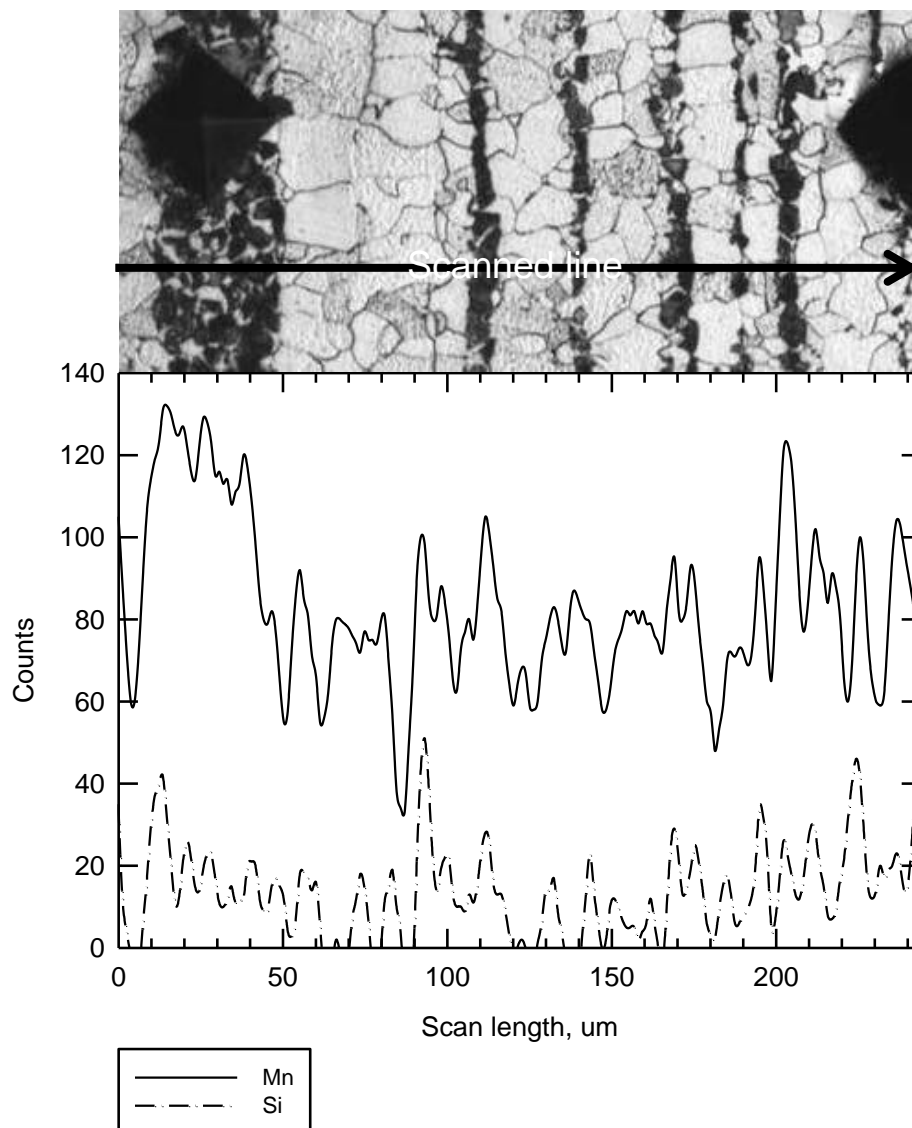


**Figure 4-2. Twenty minute line scan showing variation of manganese and silicon across bands of pearlite and ferrite**

The peaks on the Mn line reasonably correlate with the pearlite bands. The correlation is not perfect because the X-ray beams penetrate to a depth below the surface and that depends on the excitation energy and atomic mass. The variation in band thickness with depth also contributes to the imperfection. The result agrees with a previous analysis<sup>33</sup> for a low carbon steel carried out at 15 kV where the concentration of Mn was found to be slightly higher in the pearlite bands when compared with that of the ferrite bands. As expected the peaks in the Si profile correlate poorly with the pearlite bands.

An average of ten spot analyses in each of the bands of pearlite and ferrite on an unetched surface of the micrograph shown in Figure 4-3 revealed that the concentration of Mn in the two bands was in the ratio of 1.1: 1 (the standard deviation in the ratio is 2%), meaning that the pearlite band contained a slightly higher concentration of Mn. The spot size (Figure 4-4) was approximately one micrometer. The sampling time was 58 seconds. Spot analysis at slightly lower energies of 15 and 20 kV also showed that the pearlite band contained a slightly higher concentration of Mn than the ferrite band.

A typical spectrum for the spot analyses carried out in the band of pearlite is shown in Figure 4-5 and is similar to that of the ferrite. Only three elements: Mn, Si and Fe were detected in the analysis. The ratio of the Si composition is 1.37: 1 with standard deviation of 23%. The standard deviation in the Si data is higher than that of Mn because Si has a much lower atomic mass.

Area analyses in bands of pearlite and ferrite indicate that the concentration of Mn was in the ratio of 1.3:1. The area was a rectangle of 260  $\mu\text{m}^2$  (Figure 4-4), the sampling time was 4 minutes. Although the difference in the concentration of Mn between the two bands is small it is sufficient to cause segregation of carbon during slow cooling. Figure 4-6 shows the result of elemental mapping across the bands of pearlite and ferrite. The figure demonstrates that the concentration of Mn is higher in the pearlite than the ferrite bands. The sampling time was one hour. The map for Si showed, as expected, no difference in concentration in the pearlite and ferrite bands under the same sampling time.

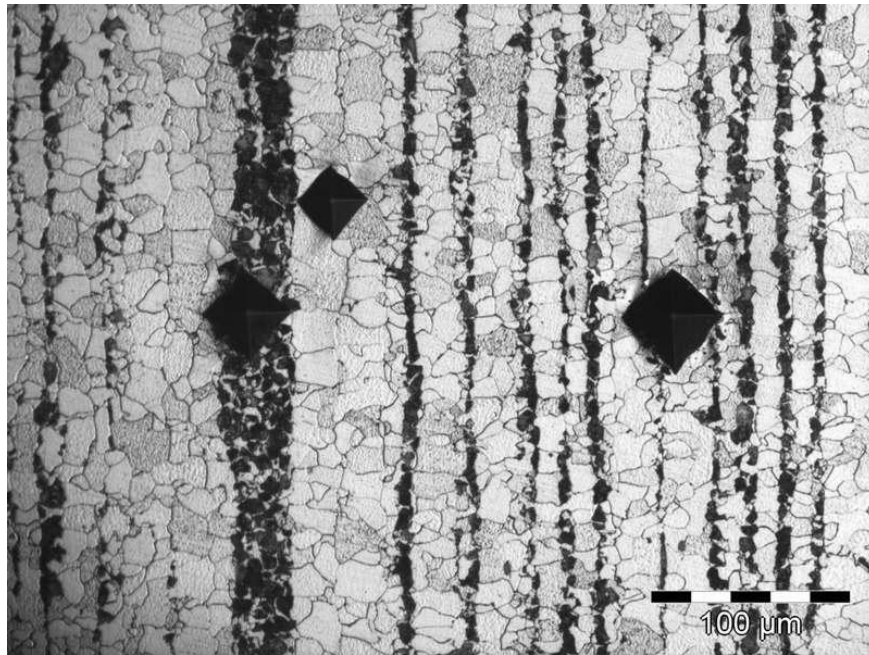


Figure 4-3. Micrograph showing longitudinal section through a pipe wall of a heat treated (furnace cooled after 20min. at 1000°C) grade X65 pipeline steel. Pearlite and ferrite etched dark and white, respectively.

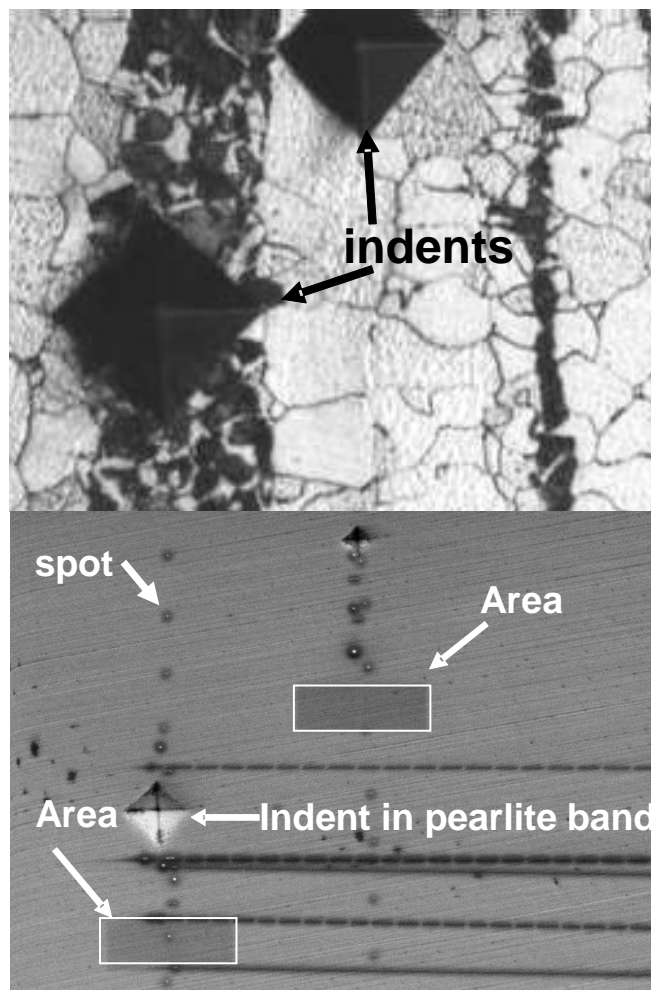


Figure 4-4. Micrograph showing the positions of the area and spot analyses, 670x

#### **4.1.1.1 Band removal through carbon diffusion**

Figure 4-7 shows that band removal depends upon the heat treatment temperature and the rate of cooling. A range of cooling rates was tried: furnace cooling is the slowest ( $\sim 0.1$  °C/s) and water quenching the fastest ( $> 30$  °C/s).

Oil and water quenching from 900°C gives a bainitic microstructure whereas air cooling from 1175°C gives a Widmanstätten structure. Air-cooling from 1000°C and fan cooling from 950°C both give slightly banded pearlite/ferrite microstructures. A heavily banded pearlite/ferrite structure is obtained by furnace cooling from 1000°C. The non-banded microstructures are obtained by transformation of austenite to a non-equilibrium microstructure by giving a faster cooling rate than that which forms a stable microstructure. In other words, the faster cooling rate suppresses the enrichment of austenite by carbon diffusion at the austenite/ferrite interface during cooling and this may lead to the precipitation of carbides within ferrite. As stated in chapter two, this is a process of band removal by hindering the segregation of carbon.

#### **4.1.1.2 Band removal through manganese diffusion**

Another approach is to remove banding by homogenisation of Mn through diffusion, as the EDX analysis confirmed that the concentration of Mn in the pearlite band is higher than that of the ferrite band. The result of an attempt to eliminate Mn segregation through diffusion is shown in Figure 4-8. This demonstrates that, as the soak time increases the pearlite centre-to-centre spacing increases. This is probably due to elimination of intermediate bands of lower concentration through diffusion.

Other heat treatments considered in an attempt to eliminate banding are summarised in Table 4-2. Furnace cooling after 5 hours at 1175°C eliminated banding but increased the average grain size to 50  $\mu\text{m}$ . This was refined to 9  $\mu\text{m}$ , without return of banding by air cooling after 20 minutes at 950°C. However, banding returned after a third heat treatment involving furnace cooling after 20 minutes at 1000°C. This indicates that the Mn segregation was not removed.

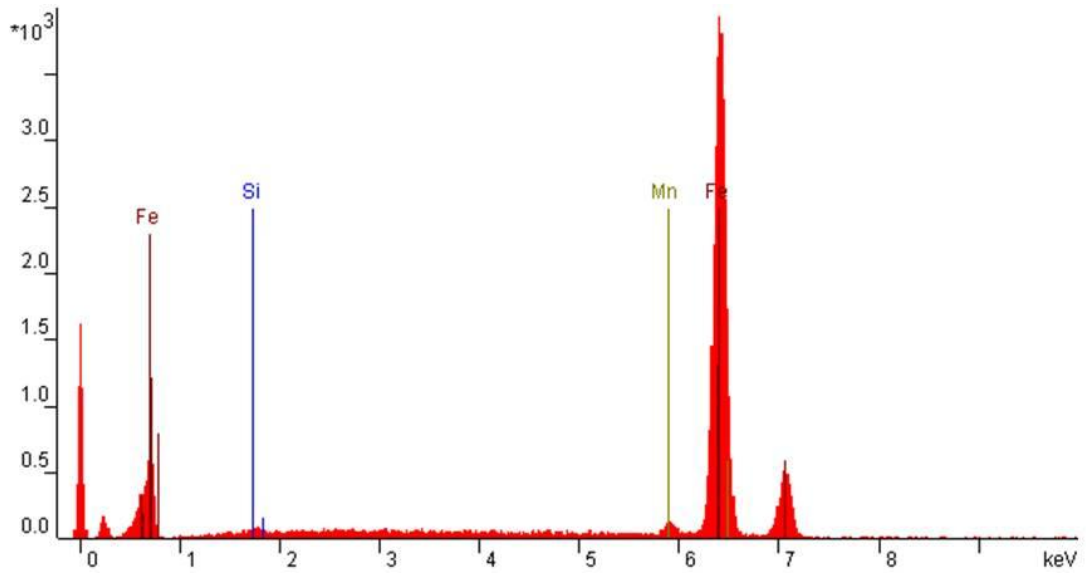


Figure 4-5. Energy-dispersive X-ray spectrum by spot analysis for a pearlite band of the heat-treated (furnace cooled after 20 minutes at 1000°C) grade X65 pipeline steel

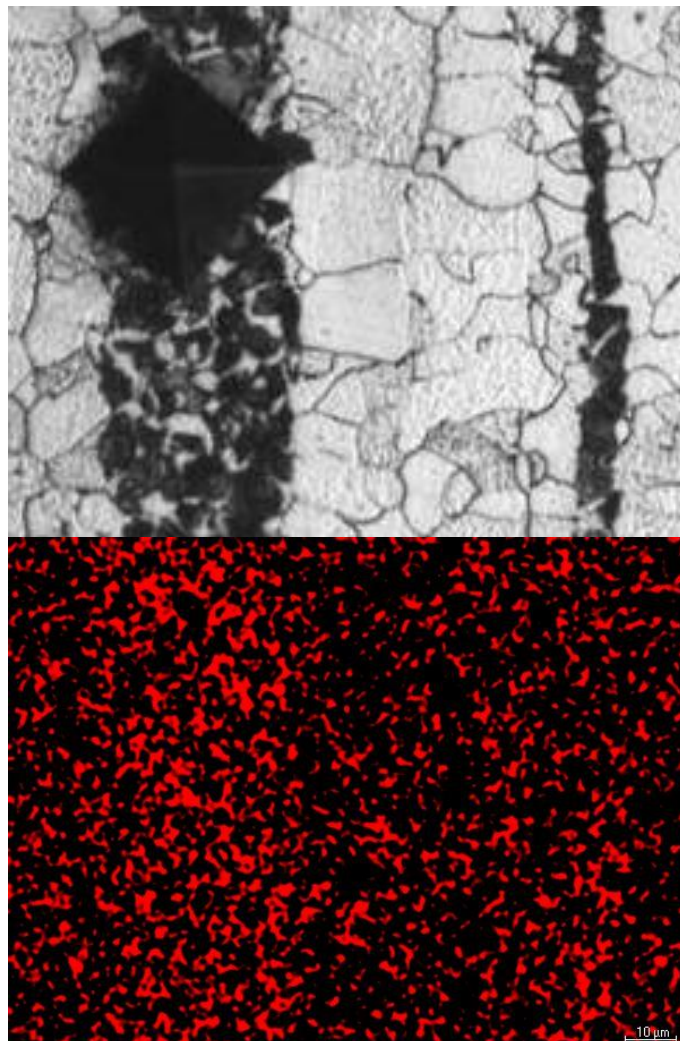


Figure 4-6. Elemental mapping showing the difference in the concentration of Mn in the band of pearlite and ferrite,

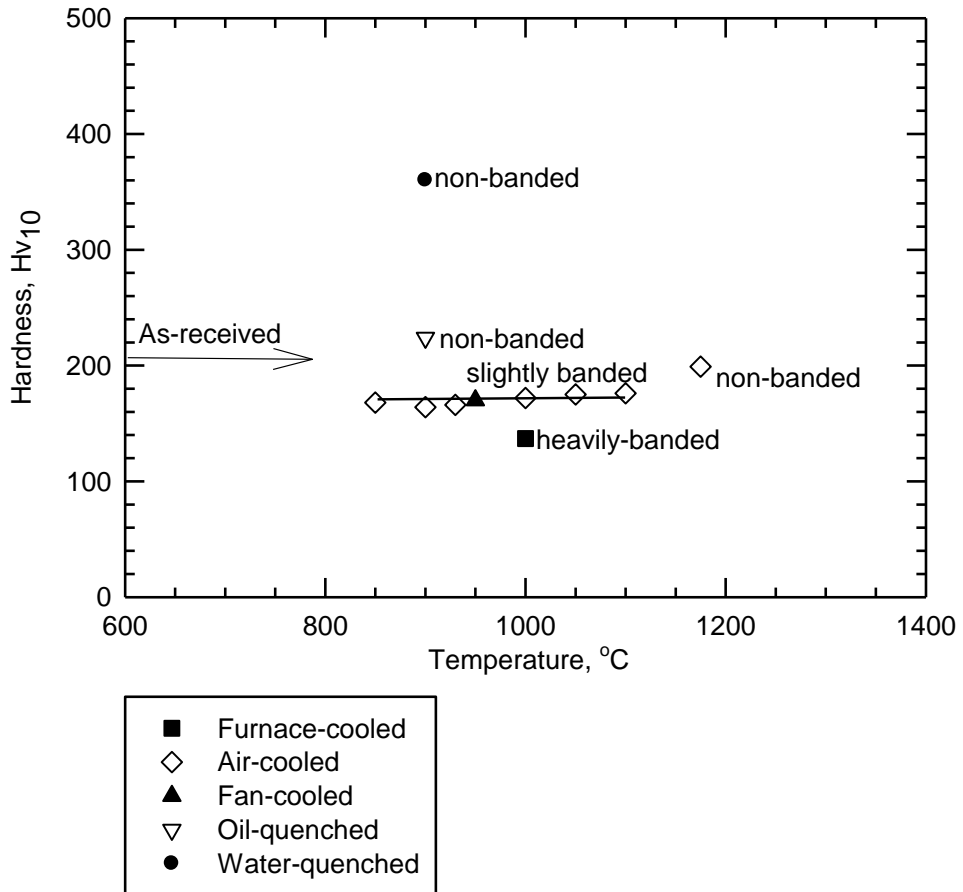


Figure 4-7. Effect of heat treatment on average hardness and banding in the 'LT' face for the grade X65 pipeline steel. Heating time for each heat treatment was 20 minutes

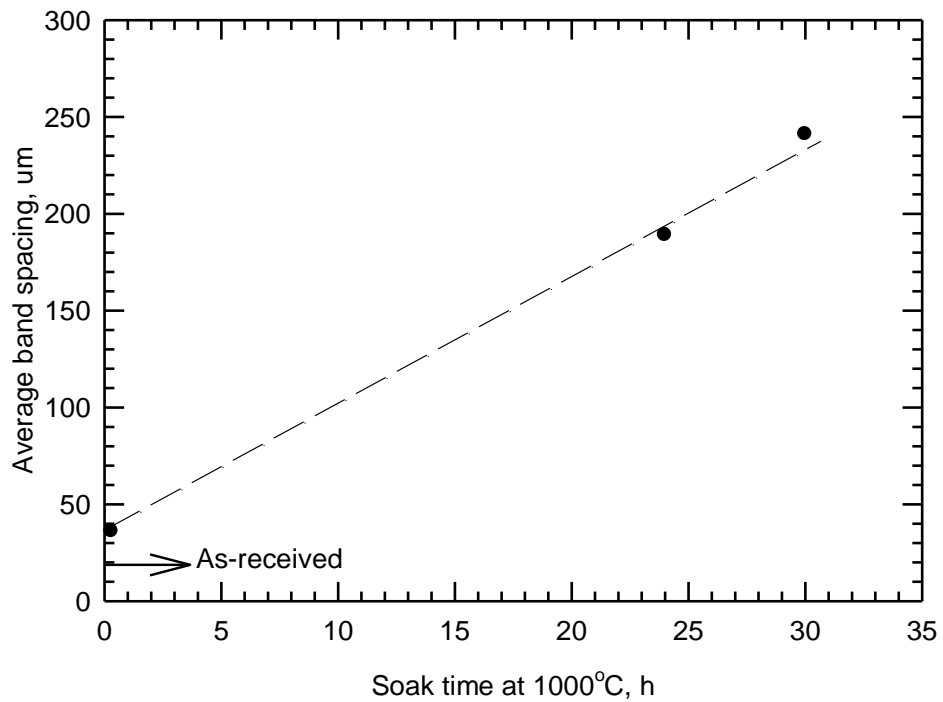


Figure 4-8. Effect of soak time on the average centre-to-centre spacing of pearlite bands in the 'LT' face of grade X65 steel; the mode of cooling applied is furnace cooling

Figure 4-9 shows the microstructures of the non-banded region in the simulated HAZ of a rectangular bar of the grade X65. One end of the bar was heated to melting in 90 seconds and then allowed to cool in air. Comparison of these microstructures with those produced by the different heat treatments shown in Figure 4-7 revealed that air cooling is the best option to simulate HAZ microstructures. Therefore, the air cooling approach was applied to the grade X100 steel.

#### 4.1.2 Grade X80 and X100

Figure 4-10 shows the hardness profiles of as-received seam-weld and HAZ for the grade X80 and X100 pipeline steels. The weld bead has the highest hardness across the section. For the X80, the difference in hardness across the weld bead and the HAZ is small. The as-received seam-weld hardness profile for the X100 agrees with a previous<sup>100</sup> micro-hardness plot for the same alloy where the maximum hardness was 320 Hv and the minimum was 240 Hv. The plot also agrees with mid-section hardness profiles for 12.7 and 15 mm thickness pipes in which the maximum and the minimum hardnesses were approximately 220 and 290 Hv, respectively<sup>25</sup>.

The heat treatment results for hardness and other mechanical properties for the grade X100 are shown in Figure 4-11. There is a correlation between the simulated hardness profile and the proof stress within the studied temperature range. Ultimate tensile strength can also be correlated with hardness.

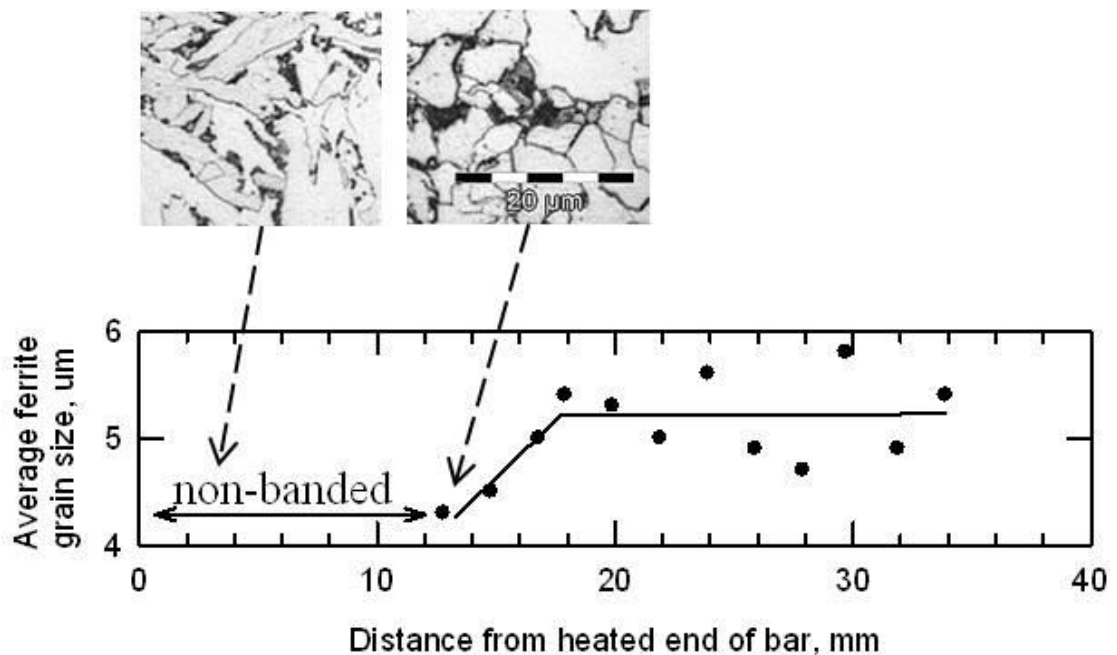


Figure 4-9. Microstructure of a heated bar of grade X65 steel, images 1150x

**Table 4-2. Effect of heat treatment on pearlite bands in the ‘LT’ face of grade X65 steel**

Temperature (°C)	Soak time	Mode of cooling	Microstructure	Grain size (µm)	No. of treatments
950	60h	FC	Banded with average spacing* (AS) 201 µm	24	1
1175	1h	FC	Slight traces of banding with large pearlite areas and some Widmanstätten	29	1
1175 then 1000	1h then 20min	FC	Banded with AS 60 µm	12	2
1175	5h	FC	Not banded with ferrite/pearlite and some Widmanstätten	50	1
1175 then 950	5h then 20min	FC then AC	Not banded (ferrite/pearlite)	9	2
1175 then 950 then 1000	5h then 20min then 20min	FC then AC then FC	Banded with AS 130 µm	10	3
1200 then 1000	20 min then 20min	FC	Banded with AS 52 µm	13	2

\* As received pearlite band spacing and average grain size: 19 and 6 µm, respectively.



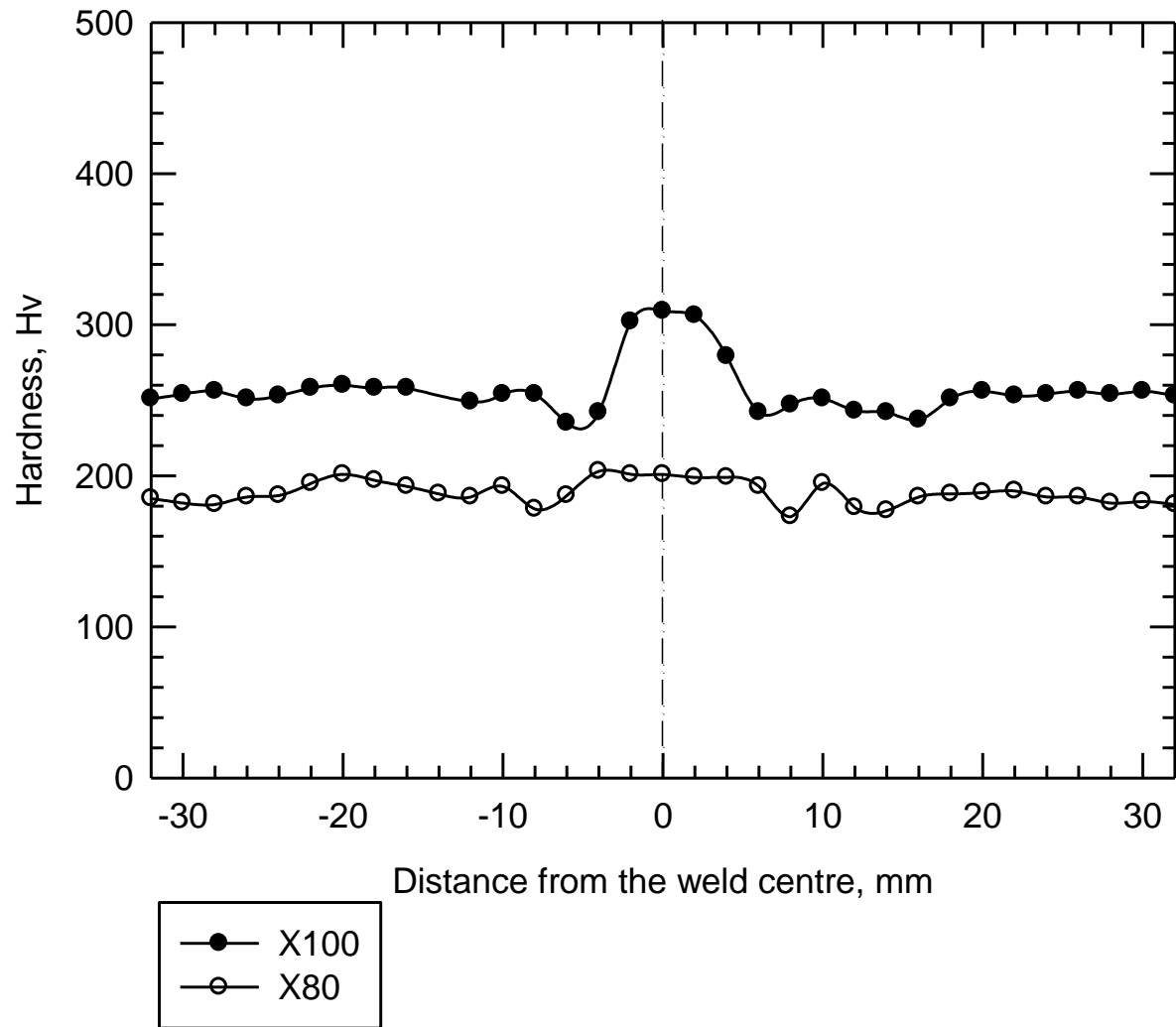


Figure 4-10. Mid-section hardness of the ‘CT’ face across the seam-weld and HAZ for grades X80 and X100 pipeline steel

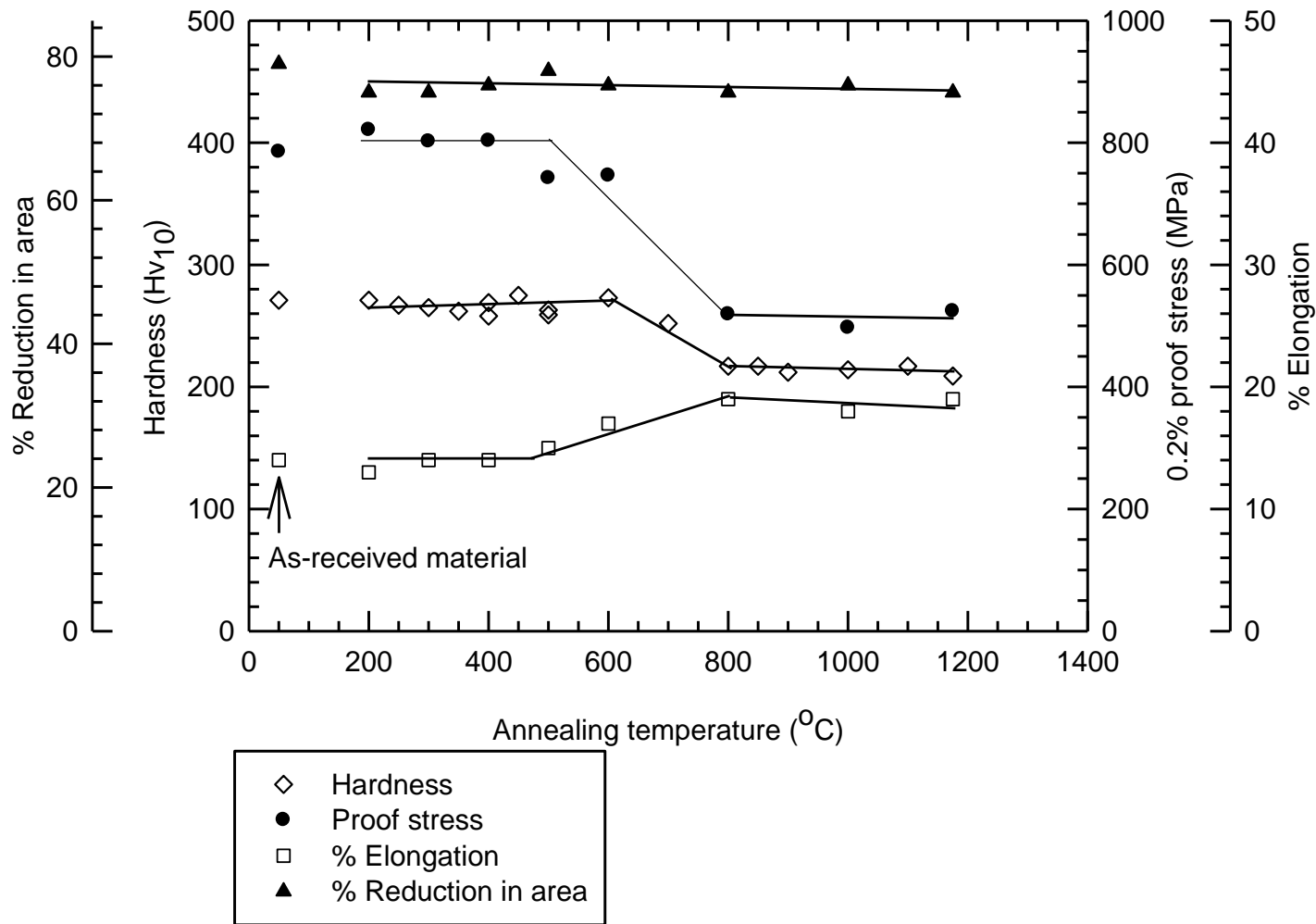


Figure 4-11. Mechanical properties of simulated HAZ of grade X100 line pipe steel. The proof stress and the ductility were measured in silicone oil at 75°C. Average hardness measured from the 'LT' face at room temperature

Figure 4-11 shows that the minimum temperature that is sufficient to affect mechanical properties is approximately 600°C. This agrees with the suggestion that the temperature at which atomic mobility is sufficient to affect mechanical properties of cold worked materials is between one-third and one-half times the absolute melting point<sup>19</sup>. This corresponds to temperatures between 328 to 629°C for the pipeline steel. Based on the carbon content of the grade X100 alloy (0.06 % weight), the estimated melting temperature is approximately 1803 K. Therefore, the microstructure for the X100 in the vicinity of the indent mark + 20 mm away from the centre of the weld could be compared with the simulated microstructure at 600°C.

#### **4.1.2.1 Seam-weld HAZ microstructures**

A noticeable (at an optical magnification of 500x) change to the as-received microstructure for the grade X100 steel due to the seam welding, extends ~ 5.5 mm on both sides of the weld metal. However, the hardness measurements indicated that the HAZ stretched up to 14 mm on both sides of the weld. The extent of the HAZ strongly depends on the heating time. A longer heating time would give more time for the heat to conduct along the length. This has been demonstrated by heating one end of rectangular bars (~ 12 x 15 x 120 mm) of the grade X100 steel to melting temperature for different times. Heating times of 5 and 10 minutes showed that the temperatures at a distance of 15 mm each from the melted ends of the bars were 626°C and 830°C, respectively<sup>101, 102</sup>.

Figure 4-12 shows the interface, where the base metal melted and fused with the weld metal. Next to the interface is the coarse grain growth zone showing Widmanstätten structure, whereas the weld metal consists of mainly acicular ferrite. At a distance of ~ 5.3 mm from the centre of the weld, a Widmanstätten structure was formed (Figure 4-13). The microstructure at distances 6 and 8 mm from the centre of the weld consists of equiaxed grains of ferrite and carbides/pearlite (Figure 4-14 and Figure 4-15). The grain sizes of the microstructures at 6 mm are bigger than those at 8 mm from the centre. Figure 4-15 contains slight traces of pearlite bands implying that the microstructure reached a slightly lower temperature during welding and also a slightly lower cooling rate when compared to the microstructure shown in Figure 4-14. It is also slightly harder, probably because of the pearlite distribution. At a distance 10 mm from the centre, the microstructure is partially transformed

(Figure 4-16). Figure 4-17 shows the microstructure at a distance 12 mm from the centre of the weld. There is no noticeable change in structure under magnification of 500 times but some softening occurs because of the heat of welding.

## **4.2 Slow strain rate testing**

### **4.2.1 Electrochemical tests**

Prior to conducting the SSRT, fast and the slow sweep rate potentiodynamic polarization curves for the grade X100 pipeline steel exposed to the carbonate solution at 75°C were produced to predict the likely potential range where film-associated cracking would occur and the result is shown in Figure 4-18. The peak current density was less than 10 mA/cm<sup>2</sup>, is in agreement with the literature<sup>71, 82</sup>. The active-passive transition – 800 to – 600 mV (sce) has been shown<sup>81, 103</sup> to be related to SCC of ferritic steels exposed to various environments. Other researchers<sup>82</sup> have demonstrated that the likely cracking range was where the difference in current density between the fast and the slow scan was of the order of at least 1 mA/cm<sup>2</sup>. The significance of this difference is that it indicates an intermediate passivation rate that is ideal for a dissolution mechanism. A high passivation rate causes the crack tip to be protected continually, while a low rate results in excessive dissolution at the crack tip, leading to blunting. Parkins suggested<sup>81</sup> that in determining the cracking range from such plots, the following two boundary conditions are applied: (1) a current density of less than that 1 mA/cm<sup>2</sup> on the fast scan plots was regarded as insignificant and (2) the difference in current density between the two sweeps divided by the current density indicated by the slow sweep rate plots at a given potential should exceed 1000. Comparison of the potentiodynamic polarisation curves for the carbonate solution with that of the nitrate<sup>104</sup> solution indicates that the current densities in the IG regions are higher in the nitrate solution than that of carbonate solution.

### **4.2.2 SSRT in the carbonate solution for the as-received X100**

The crack velocity result of SSRT on the as-received grade X100 steel between the potentials of – 500 and – 1100 mV (sce) is shown in Figure 4-19. The scan plots (Figure 4-18) were not extended up to – 1100 mV (sce) because it is well established

that in the carbonate solution, at potentials more cathodic than the free corrosion potential (FCP) of  $\sim -890$  mV (sce), hydrogen bubbles are generated on the surface of the steel even at  $25^{\circ}\text{C}$ <sup>105</sup>.

As predicted, film-associated cracks were measured at potentials anodic to the FCP and hydrogen-associated cracks were measured at potentials cathodic to the FCP. Both intergranular (IG) and transgranular (TG) cracks were observed on filmed specimens and this in agreement with the work conducted by Parkins and Zhou<sup>50</sup>. The transition between the two modes of cracking lies between  $-650$  mV and  $-675$  mV (sce). The micrographs, Figure 4-20 and Figure 4-21 are for tests conducted at potentials of  $-650$  and  $-720$  mV (sce). It was observed that cracks that are associated with hydrogen evolution are mainly transgranular and are not related with film formation.

#### **4.2.2.1 Types of film associated with the SCC of the grade X100**

Table 4-3 shows details of the different types of film formed at different potentials anodic to the FCP. The flat and the nodular film induced IG and TG cracks, respectively whereas the pseudo-cubic film induced less secondary cracking but is associated with embrittling the steel (Figure 4-22). The results in the table suggest that the sharp drop in current density in the slow sweep rate plot (Figure 4-18) is related to the change in surface condition of the steel. The secondary crack velocities (Figure 4-19) within the anodic potential range are approximately  $1 \times 10^{-6}$  mm/s and this is low compared with a lower steel grade in a similar environment<sup>5</sup>. Figure 4-22 shows that the grade X100 generally embrittles less at the potentials where IG cracks are observed. In the TG region, the embrittlement index generally increases as the applied potential becomes more negative.

#### **4.2.3 Susceptibility of the as-received and heat treated X100 compared**

The as-received seam-weld HAZ microstructures have been shown previously (Figure 4-13 and Figure 4-14). The microstructures simulated by air cooling after 20 minutes at temperatures of  $1175^{\circ}\text{C}$  and  $1000^{\circ}\text{C}$  (Figure 4-23) are similar (in phases distributions) to the as-received seam-weld HAZ microstructures.

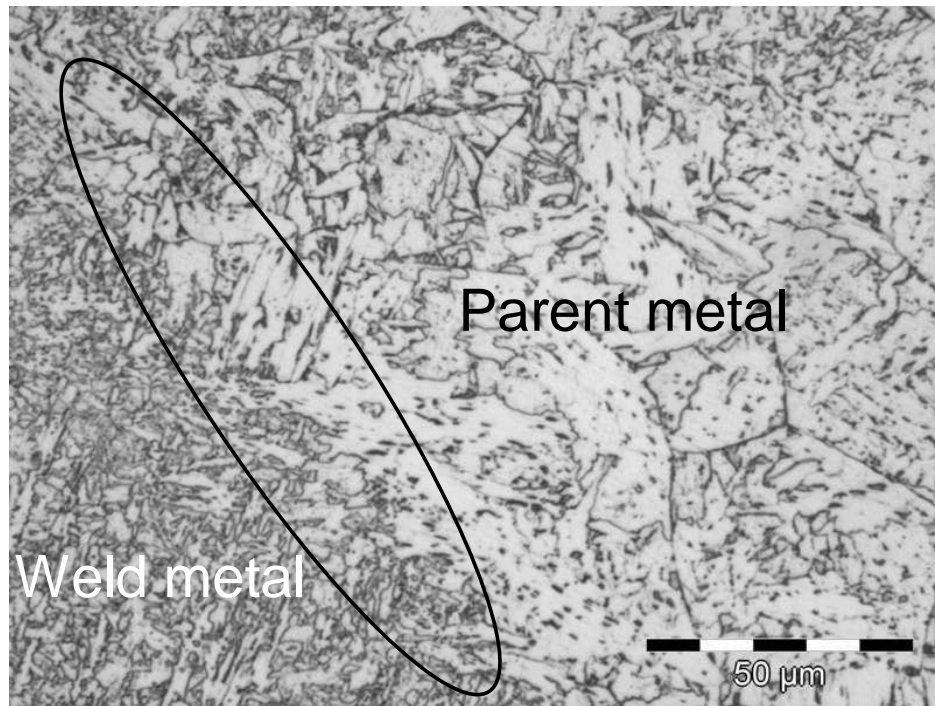


**Figure 4-12. The interface boundary (encircled region) for weld and parent metal**

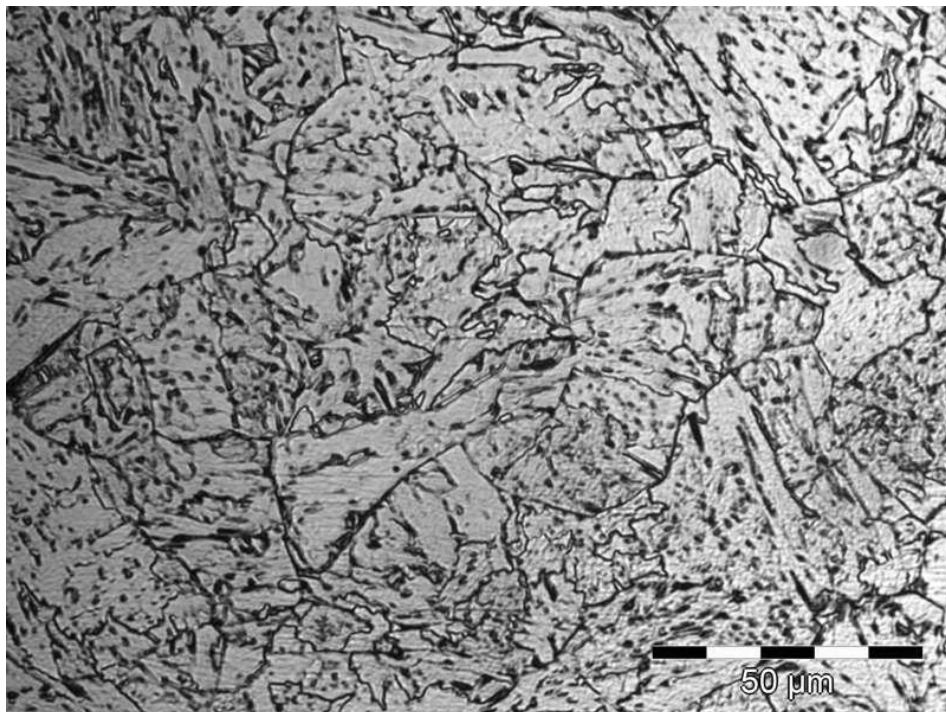


**Figure 4-13. Widmanstätten structure at 5.3 mm from the centre of grade X100 steel seam weld (Figure 4-10)**

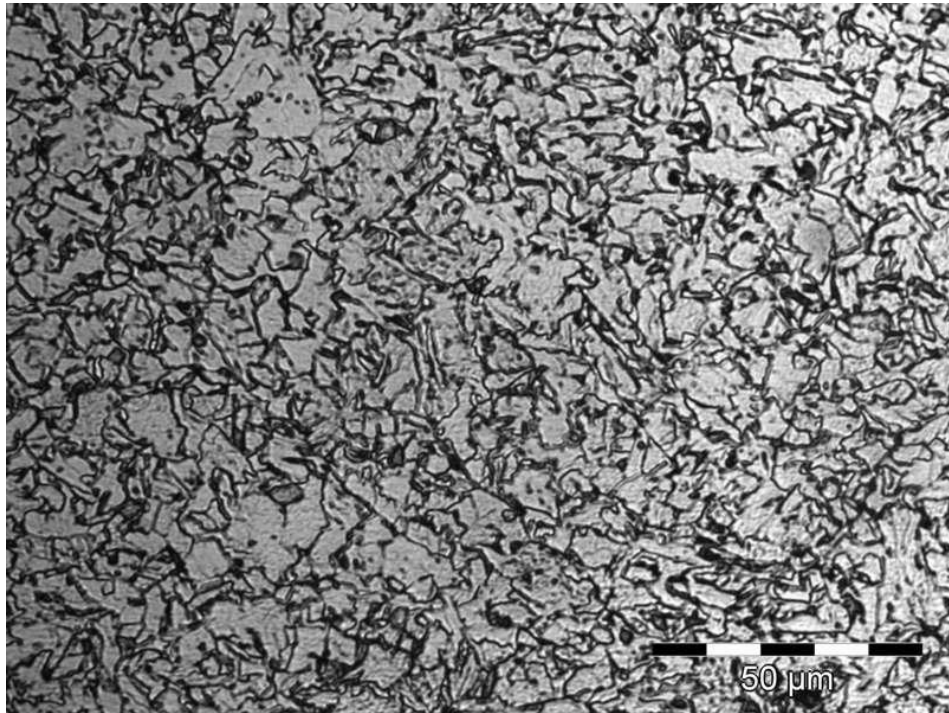


**Figure 4-14. Microstructure formed at 6 mm from the centre of the grade X100 steel seam weld**

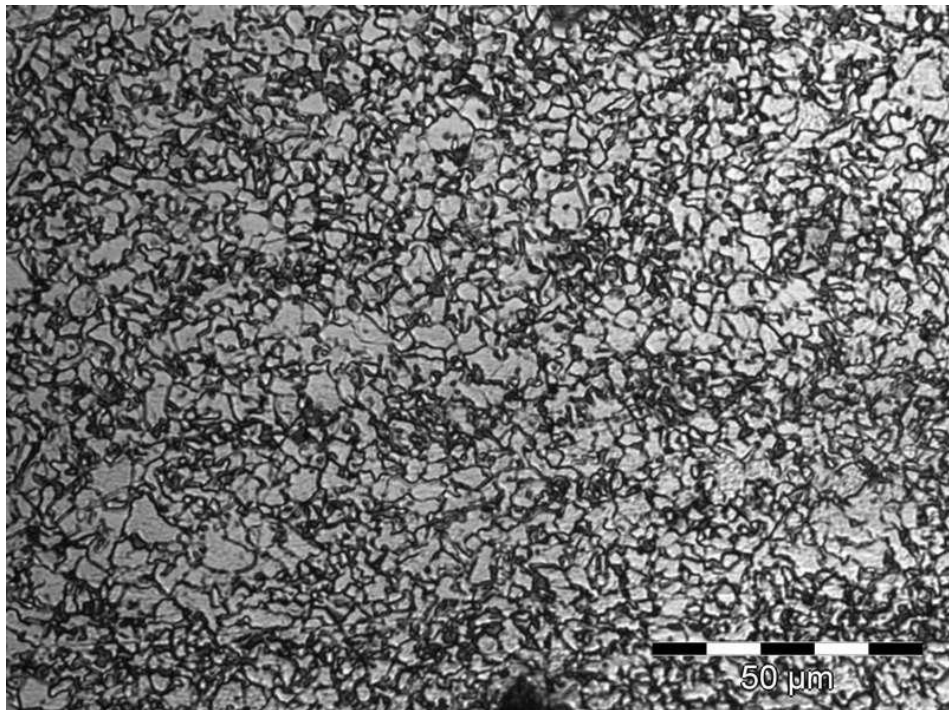


**Figure 4-15. Microstructure formed at 8 mm from the centre of the grade X100 steel seam weld**



Figure 4-16. Microstructure formed at 10 mm from the centre of the grade X100 steel seam weld

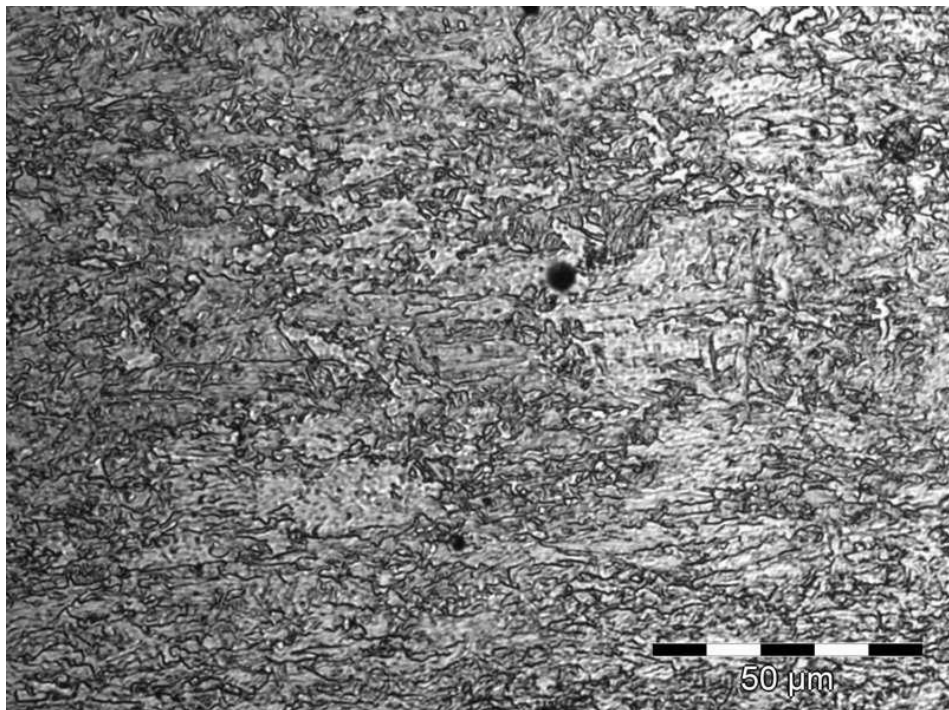


Figure 4-17. Microstructure formed at 12 mm from the centre of the grade X100 steel seam weld



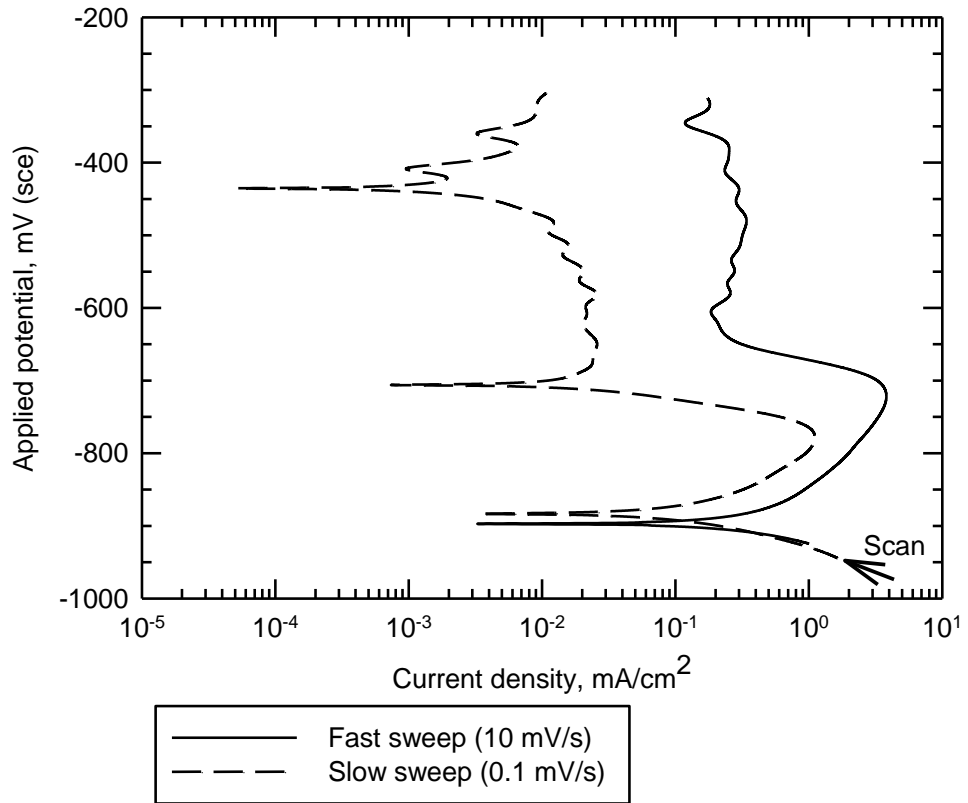


Figure 4-18. Fast and slow sweep rate potentiodynamic polarisation curves for as-received grade X100 steel in carbonate environment at 75°C.

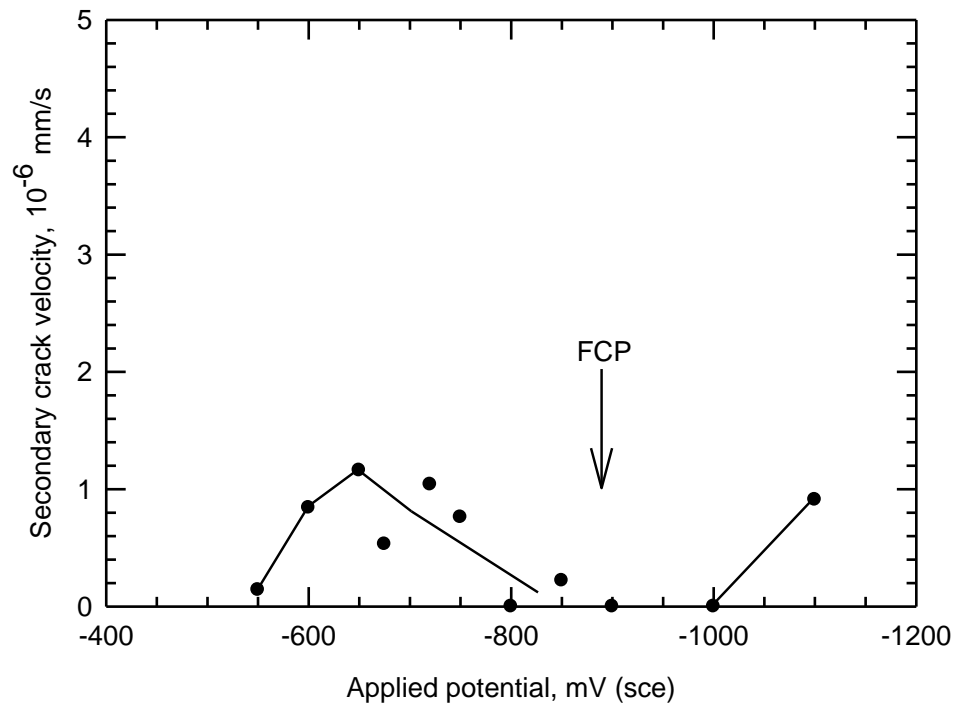
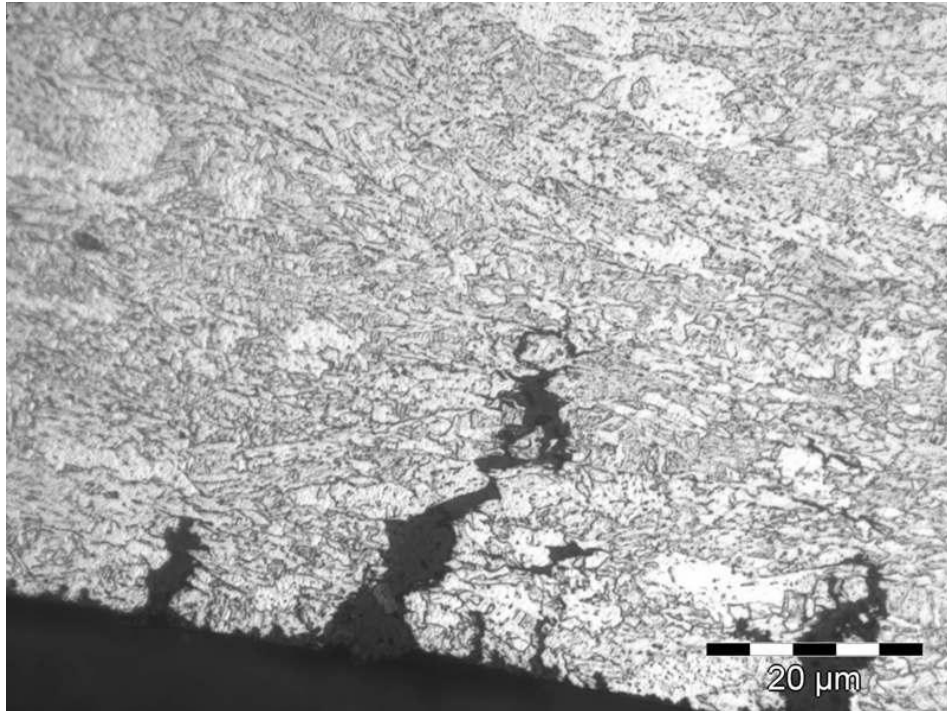
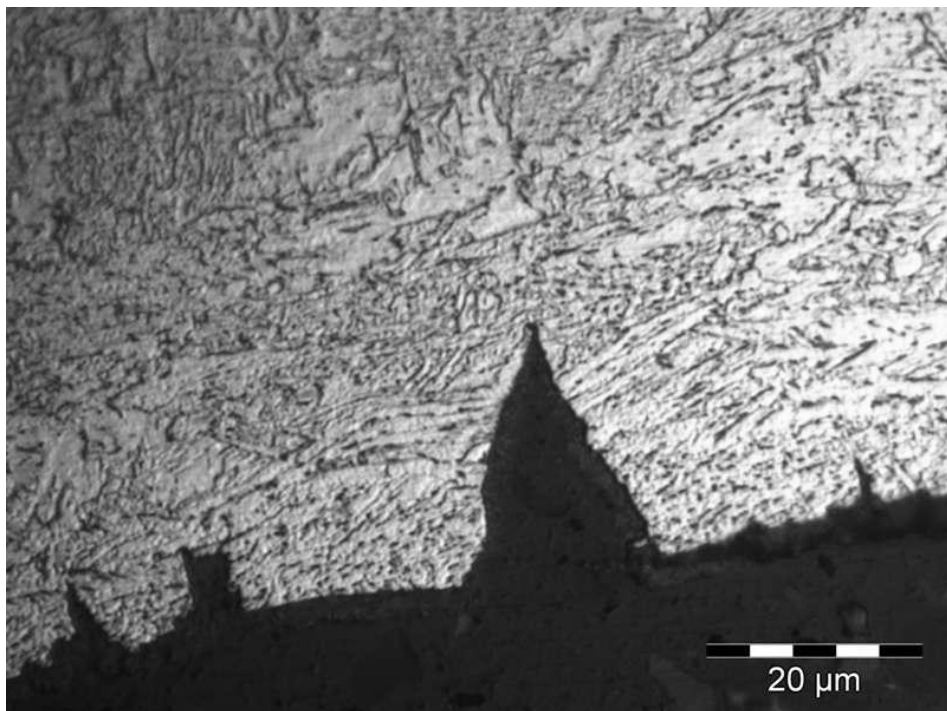


Figure 4-19. Variation of average secondary crack velocity with potential for the as-received grade X100 in carbonate environment at 75°C

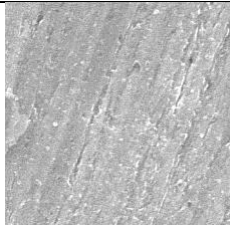
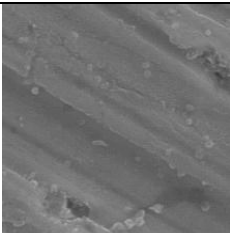
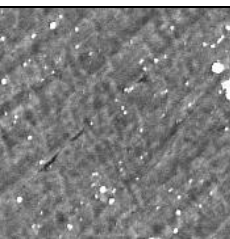
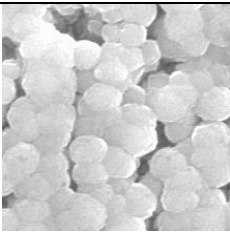
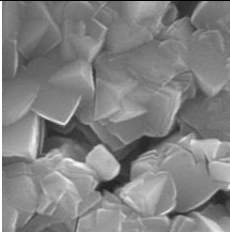
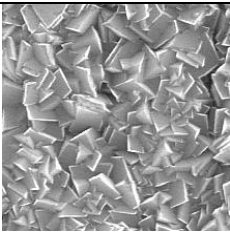


**Figure 4-20. IG cracks in as-received X100 pipeline steel tested in the carbonate solution at an applied potential of  $-650$  mV and at  $75^{\circ}\text{C}$ . Prior to testing specimen was held for 24h at  $-500$  mV (sce)**



**Figure 4-21. TG cracks in as-received X100 pipeline steel tested in the carbonate solution at an applied potential of  $-720$  mV and at  $75^{\circ}\text{C}$**

**Table 4-3. Details of the different types of film formed on the surface of the as-received grade X100 steel at different potentials, film growth time (4h) and micrographs were taken at 5000x**

Potential (mV) sce	Film type	Film micrograph	Chemical composition/remarks	Failure mode
- 490	none		at the boundary of anodic protection	ductile
- 600	flat and smooth		contains siderite <sup>106</sup>	IG
- 650	textured		siderite and magnetite <sup>106</sup>	IG
-720 and - 750	nodular		contains magnetite and siderite <sup>106</sup>	TG
- 800	pseudo-cubic		contains Fe <sub>2</sub> O <sub>3</sub> and magnetite (Fe <sub>3</sub> O <sub>4</sub> ) <sup>106</sup>	TG
-850	pseudo-cubic fine crystal		contains less siderite than nodular	TG

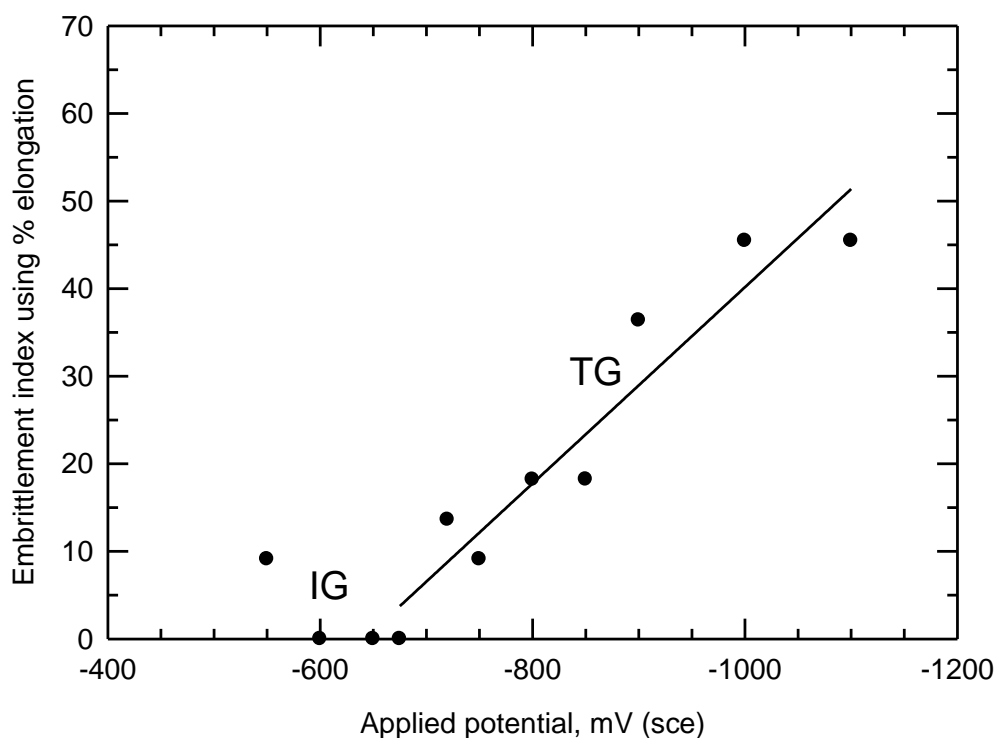
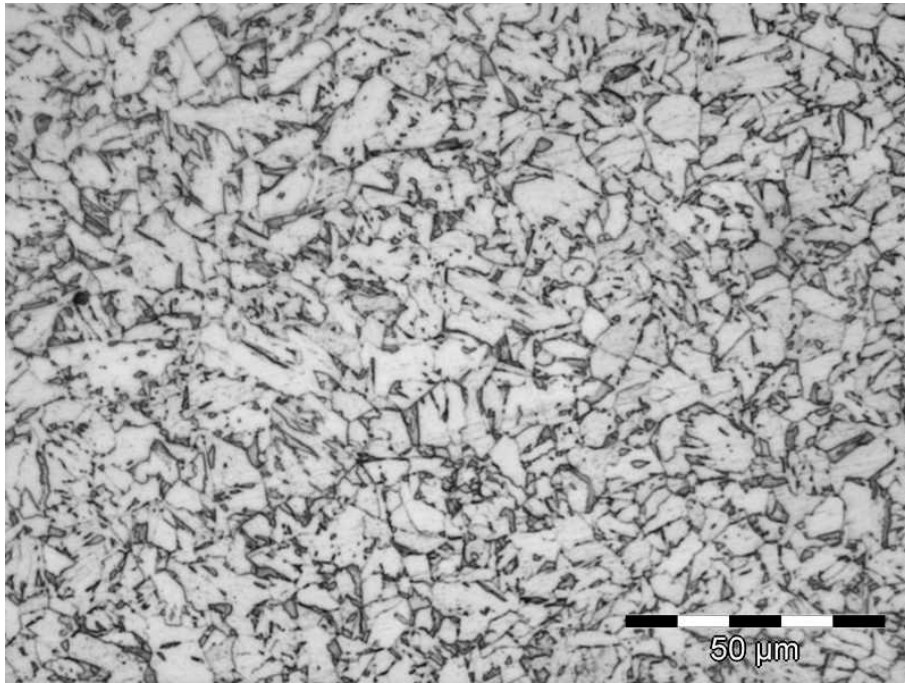
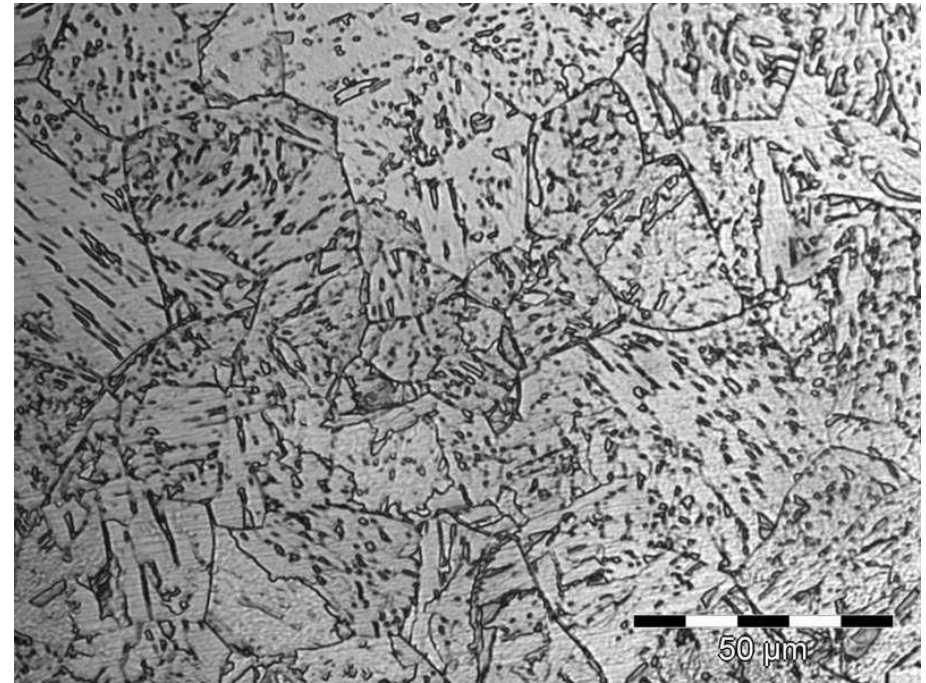


**Figure 4-22. Variation of embrittlement index (using % elongation) with potential for the as-received grade X100 steel in the carbonate solution at 75°C.**

Figure 4-24 shows the relationship between the applied potential and the average secondary crack velocity for as-received and heat-treated specimens of grade X100 pipeline steel. The peaks of IG cracking occur at a potential of around  $-600$  mV (sce), fall sharply and then gradually approach zero at  $-800$  mV (sce). Susceptibility to the carbonate solution at  $-600$  mV (sce) appears to increase with increasing heat treatment temperature whereas the resistance to cracking is approximately the same for both the as-received and the heat-treated specimens where the mode of cracking changes to TG. The transition from IG to TG occurs  $\sim$  between potentials of  $-650$  and  $-700$  mV (sce). This agrees with previous work carried out in a solution of similar concentration<sup>50</sup>. Although the specimens heat treated at  $1000^{\circ}\text{C}$  and  $1175^{\circ}\text{C}$  are relatively softer and more ductile than the as-received, they are more susceptible to IG attack and this is possibly due to compositional changes in the grain boundaries. At potentials more cathodic than  $-800$  mV, the secondary crack velocity generally increases as the potential becomes more negative and it appears to be indifferent to microstructure.



(a)



(b)

Figure 4-23. Simulated microstructures in specimens air cooled after 20 minutes at: (a) 1000°C and (b) 1175°C

Figure 4-25 shows the effect of heat treatment temperature and grain size on IG cracking at an applied potential of  $-600$  mV (sce). The figure demonstrates that the secondary crack velocity increases with increase in heat treatment temperature. The sudden change in gradient in the crack velocity plot indicates a change in distribution from ferrite/pearlite to Widmanstätten structures. However, the same figure indicates that grain size has no significant effect on the secondary crack velocity. The increase in the crack velocity may be associated with changes at the grain boundary due to the heat treatment. It might be connected with migration and coalescence of carbide particles. The change in gradient in the grain size plot also indicates a change in microstructure. Figure 4-26 shows the relationship between the primary and secondary crack velocity. The primary crack velocity is generally bigger than the secondary crack velocity except between the potential  $-700$  to  $-850$  mV (sce) where the difference between the two crack velocities seems to be insignificant. However, the difference between the primary and the secondary crack velocity at an applied potential more cathodic than  $-850$  mV (sce) increases as the potential becomes more negative and the secondary cracking is less.

Figure 4-27 and Figure 4-28 show IG and TG primary cracks for tests carried out at applied potentials of  $-600$  and  $-700$  mV (sce), for the heat treated (air cooled after 20min at  $1175^{\circ}\text{C}$ ) grade X100 alloy. The transition from IG to TG is between the potentials  $-600$  to  $-650$  mV (sce). Figure 4-29 shows shallow secondary TG cracks from uninterrupted SSRT at potential of  $-650$  mV (sce). In an interrupted SSRT at the same applied potential where a specimen was held for two days at a load just before UTS and then loaded to fracture, the shallow TG cracks in the uninterrupted test grew across grain boundaries (Figure 4-30). This confirmed that the mode of cracking is transgranular and the position of the transition potential from IG to TG (Figure 4-26) is anodic to  $-650$  mV (sce).

In addition to the secondary crack velocity (Figure 4-24), the relative susceptibility of the as-received and the heat-treated grade X100 steel were compared using embrittlement indices (Figure 4-31 and Figure 4-32). Figure 4-31 shows that the specimens heat-treated at  $1175^{\circ}\text{C}$  generally embrittle more than both the as-received and the specimens heat-treated at  $1000^{\circ}\text{C}$ .

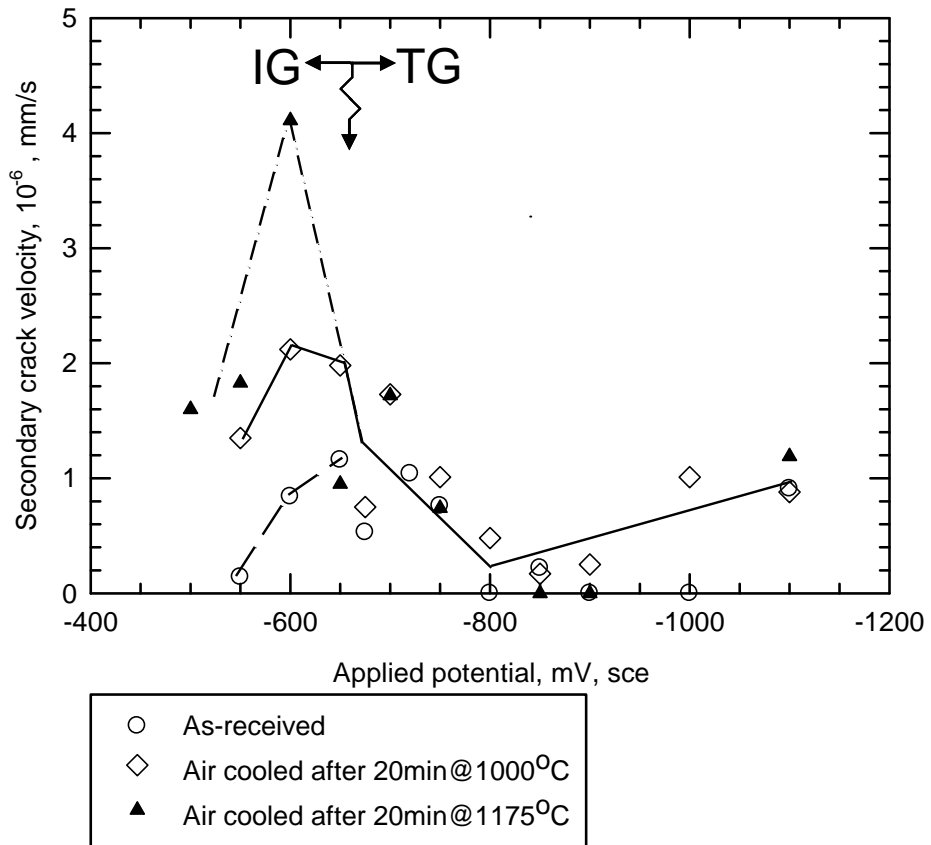


Figure 4-24. Variation of average secondary crack velocity with potential for the as-received and heat-treated grade X100 pipeline steel in the carbonate solution at 75°C.

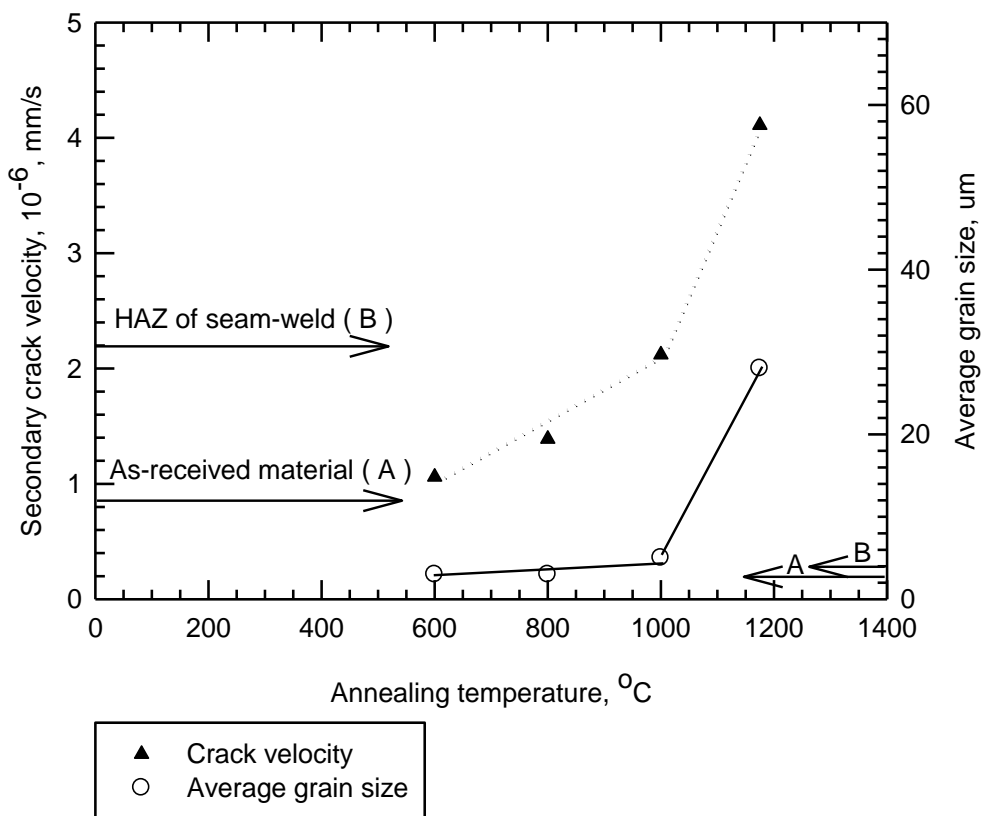
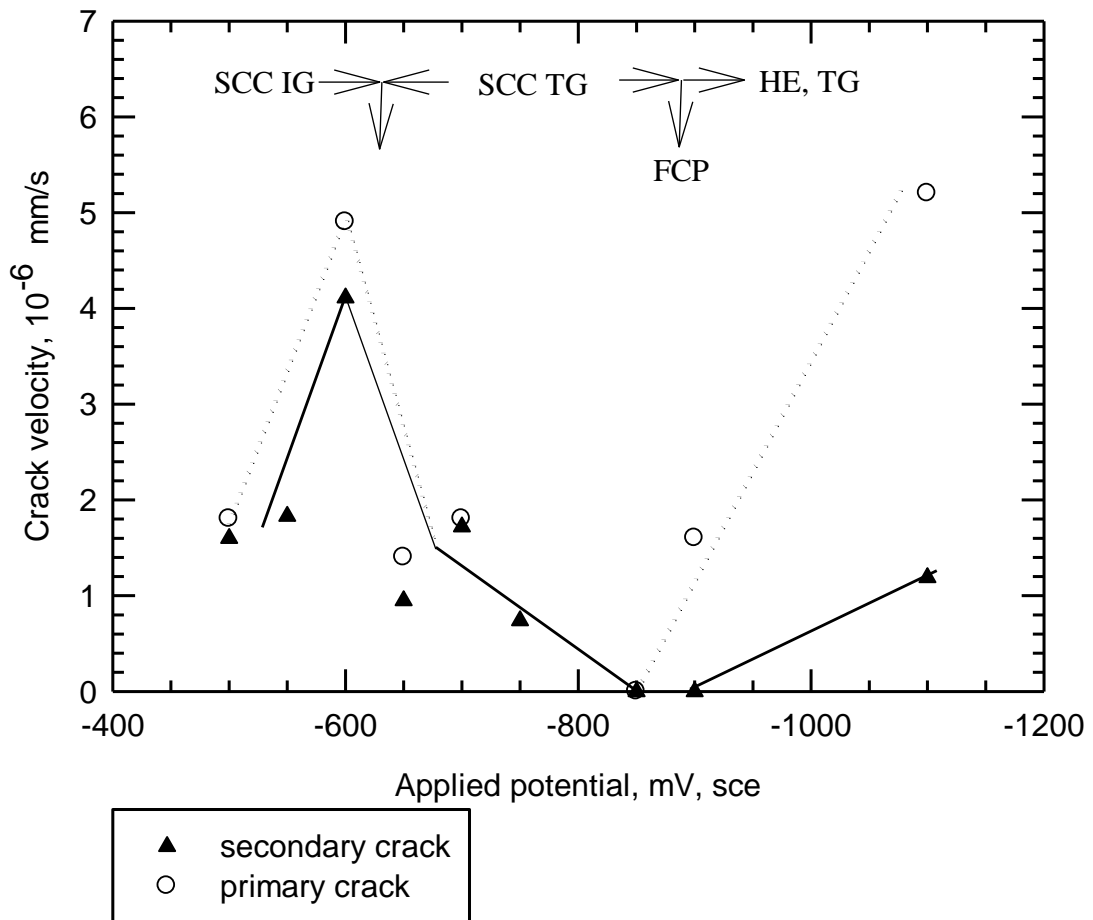


Figure 4-25. Effect of heat treatment on average secondary crack velocity and grain size of grade X100 pipeline steel in carbonate solution at 75°C and a potential of -600 mV (sce)



**Figure 4-26. Variation of average secondary and primary crack velocities with potential for the heat treated (air cooled after 20min at 1175°C) grade X100 pipeline steel in the carbonate solution at 75°C.**

The embrittlement indices of the as-received and the specimens heat-treated at 1000°C appear to be the same, allowing for the scatter. However, Figure 4-32 indicates that the embrittlement indices for the as-received and the heat-treated specimens are the same in both IG and TG regions. As expected, both the percent elongation ratio (Figure 4-33) and percent reduction in area ratio (Figure 4-34) agree with Figure 4-31 and Figure 4-32, respectively.

The difference in the two ductility plots (% elongation and % reduction in area) could be explained by Figure 4-35. The figure reveals that the fracture surface “ovality” (ratio of two perpendicular diameters on fracture surfaces) approaches one as the applied potential becomes more negative. The difference in susceptibility to the carbonate solution between the as-received and the heat-treated specimens is more apparent (Figure 4-32 and Figure 4-34) at potentials more negative than – 850 mV (sce), where the effect of ovality is less.



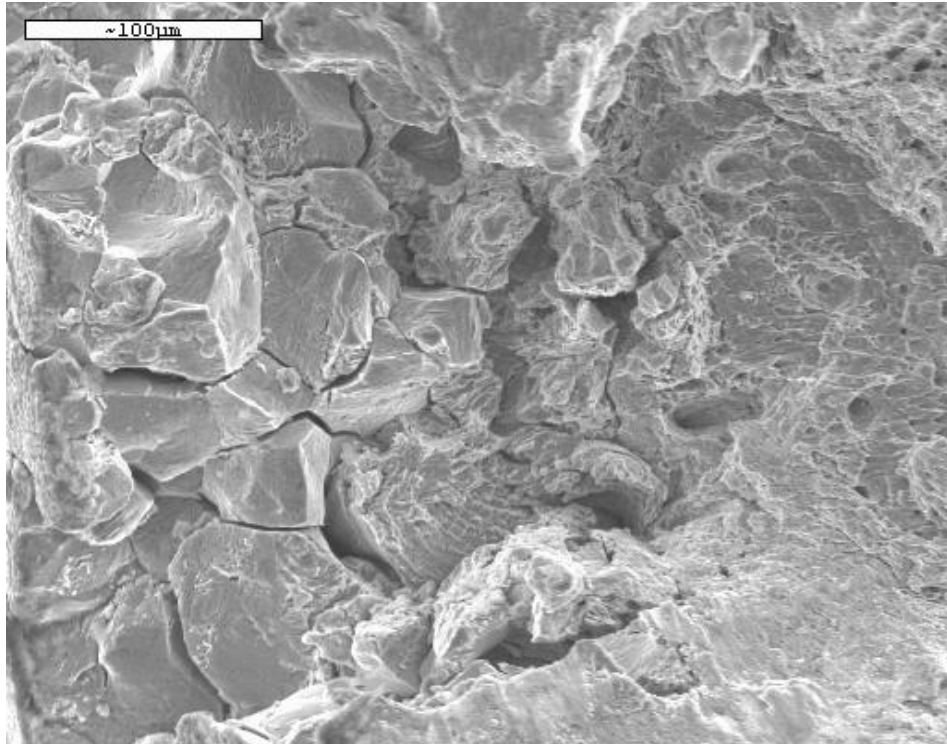


**Figure 4-27. IG crack on the fracture surface of the heat treated (air cooled after 20min at 1175°C) grade X100 pipeline steel tested in the carbonate solution at 75°C and an applied potential of - 600 mV.**

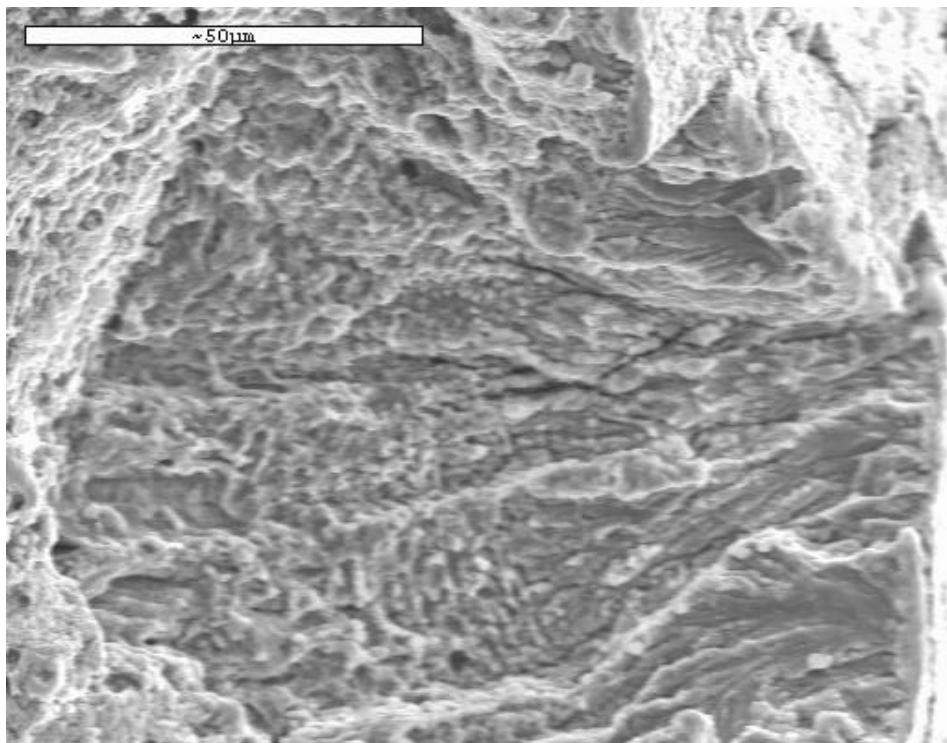


**Figure 4-28. TG crack on the fracture surface of the heat treated (air cooled after 20min at 1175°C) grade X100 pipeline steel tested in the carbonate solution at 75°C and applied potential of - 700 mV.**

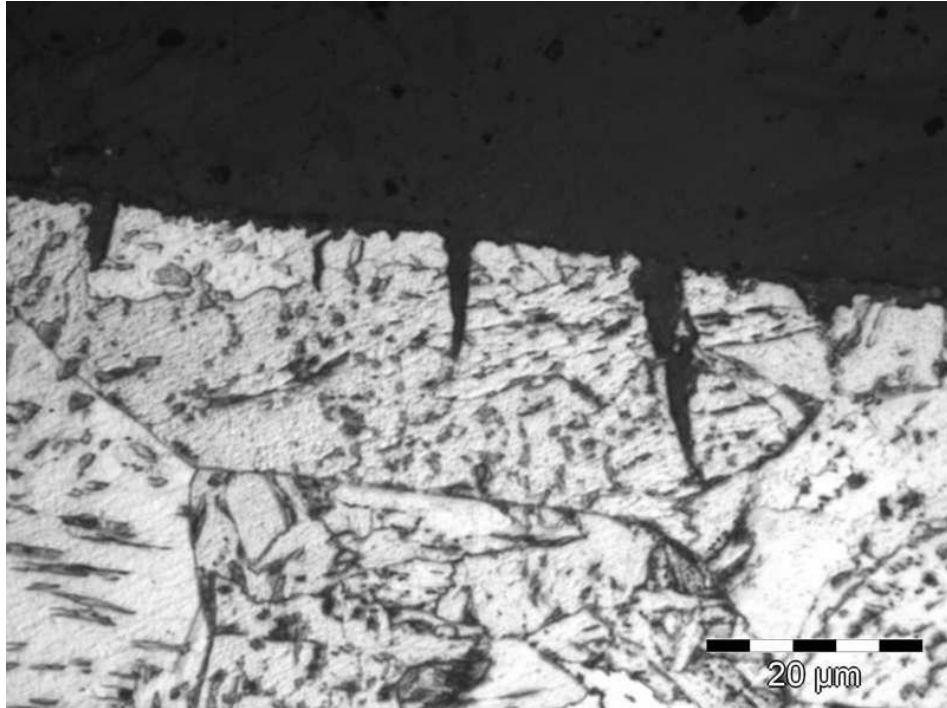


**Figure 4-29. Shallow TG secondary cracks in the heat treated (air cooled after 20min at 1175°C) grade X100 pipeline steel tested in the carbonate solution at 75°C and an applied potential of – 650 mV.**

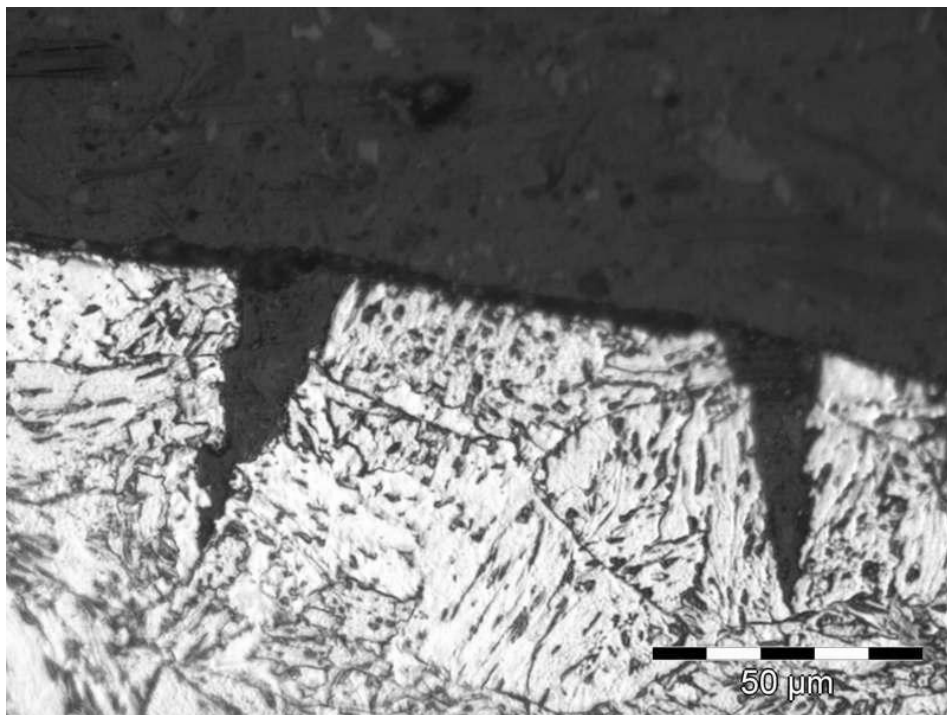


**Figure 4-30. TG secondary cracks in the heat-treated (air cooled after 20min at 1175°C) grade X100 steel in the carbonate solution at 75°C and an applied potential of – 650 mV. Test held for two days at a load just before UTS and then loaded to fracture.**

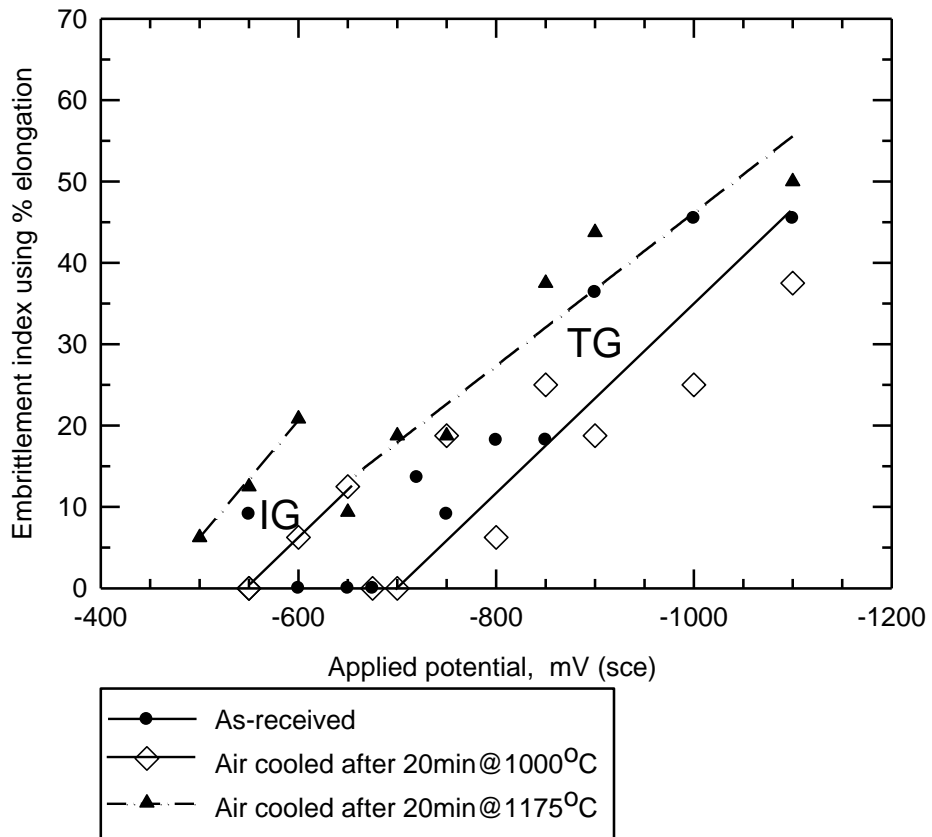


Figure 4-31. Variation of embrittlement index (using % elongation) with potential for the grade X100 pipeline steel in the carbonate solution at 75°C

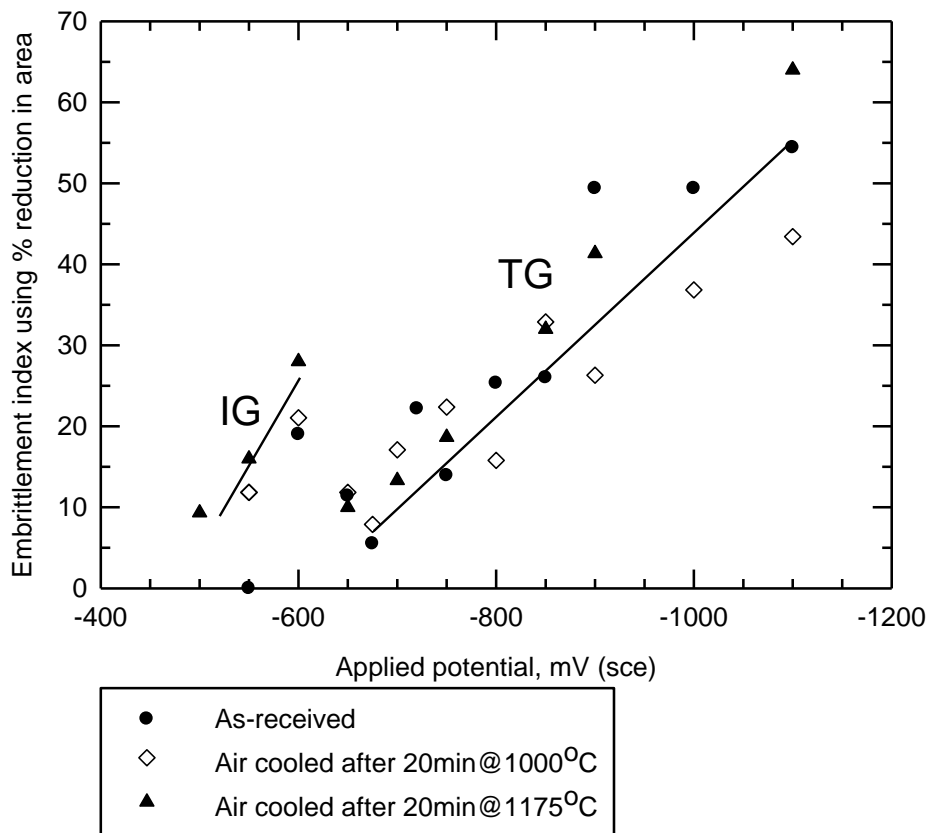


Figure 4-32. Variation of embrittlement index (using % reduction in area) with potential for the grade X100 pipeline steel

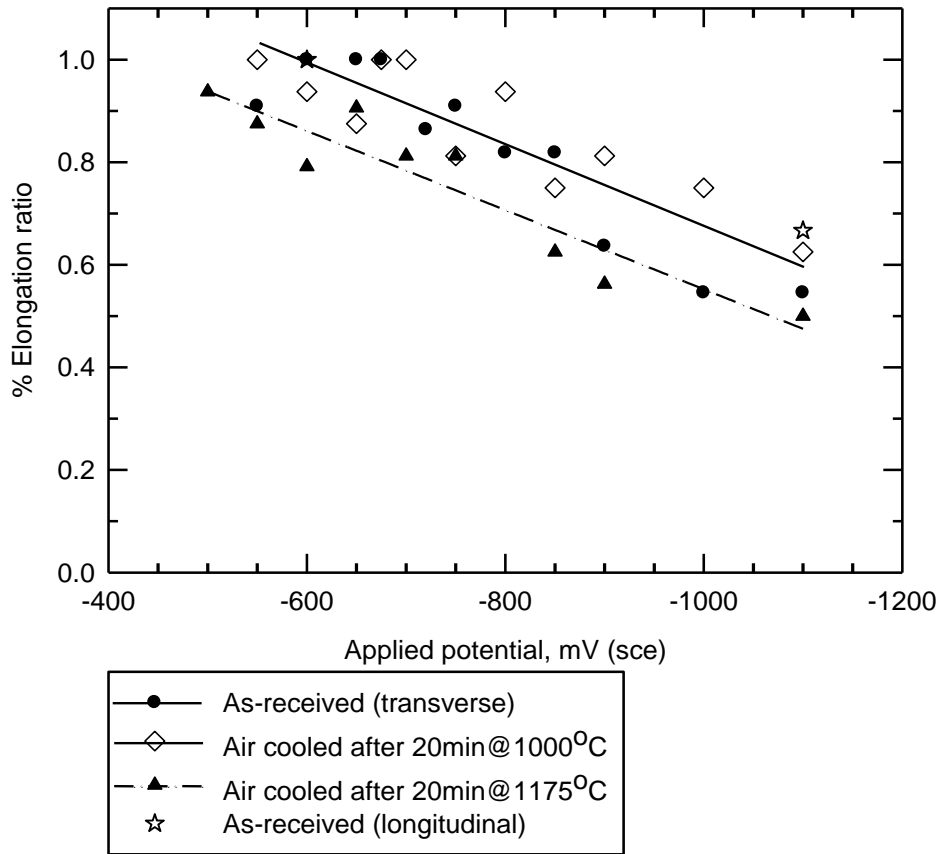


Figure 4-33. Variation of % elongation ratio (solution : silicone oil) with potential for the grade X100 steel

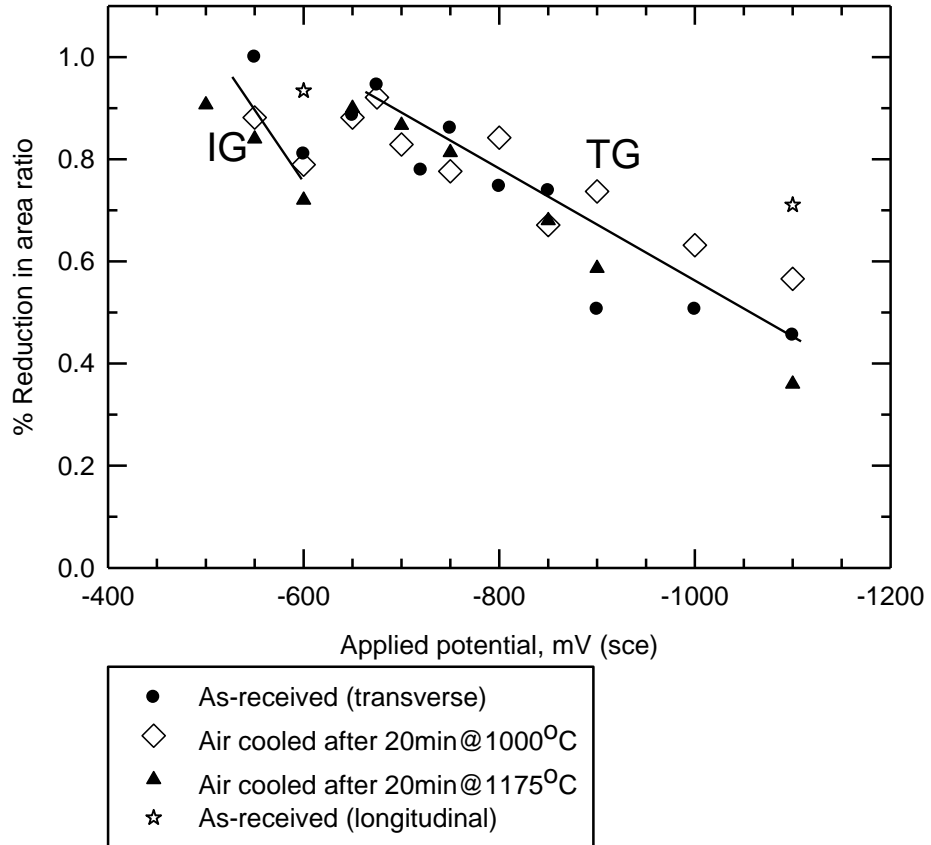
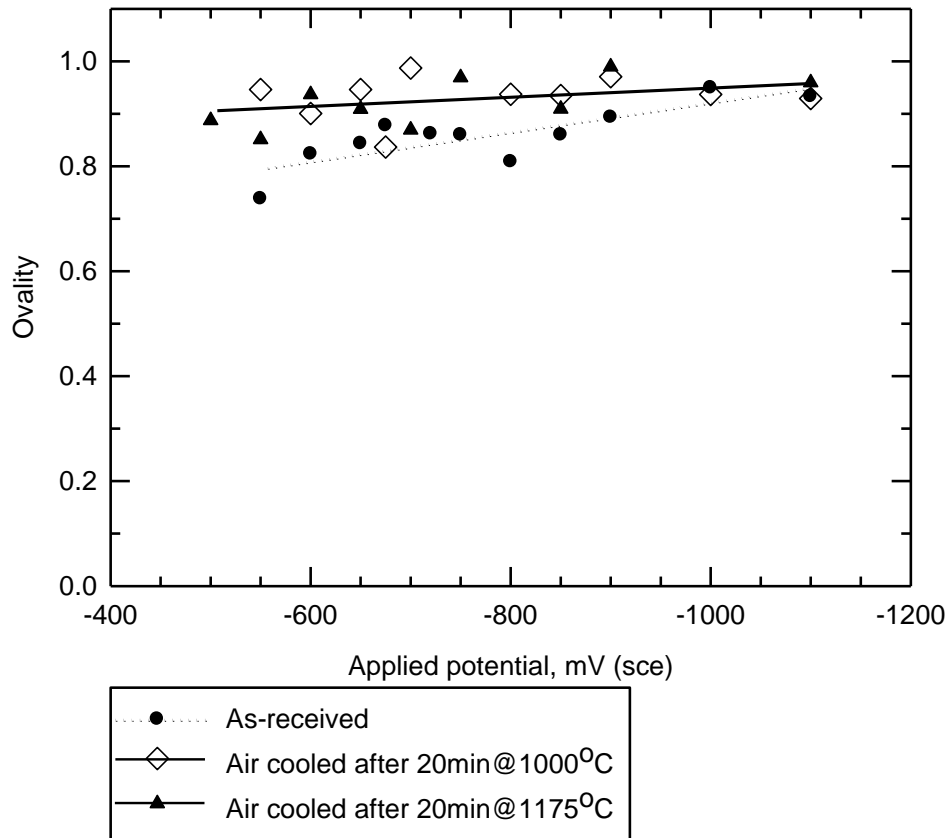


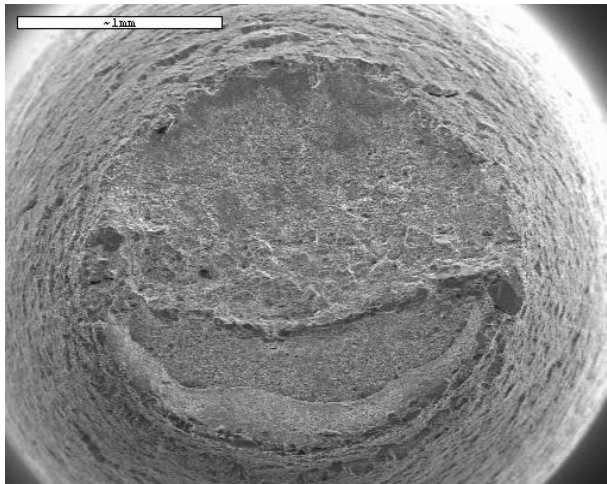
Figure 4-34. Variation of % reduction in area ratio (solution : silicone oil) with potential for the grade X 100 steel

Figure 4-35 also demonstrates that the ovality is more severe in the as-received than in the heat-treated specimens. A study of the microstructures of the fracture surfaces indicated that the grains in the heat-treated specimens are equiaxed and non-banded, whereas the grains of the as-received specimens are elongated and banded. The study also revealed that the longer diameter of the ovality is parallel to the direction of grain elongation/banding, the major direction of rolling.



**Figure 4-35. Effect of heat treatment on fracture surface ovality**

Figure 4-36 shows a fracture surface with an ovality ratio of 0.86. A representative unloaded microstructure of the fracture surface is that of the ‘LT’ face and a low magnification micrograph of the face is shown in Figure 4-37. The low magnification microstructures of the ‘CT’ face is shown in Figure 4-38 and there is no banding in the ‘CL’ face. The combined effect of the ovality and banding on crack growth in the ‘CL’ and ‘CT’ faces are shown in Figure 4-39 and Figure 4-40. Secondary cracks grow larger in the ‘CL’ face than in the ‘CT’ face. Although the applied stress is equal in all direction and the ‘CL’ face is not banded, the banding in the ‘LT’ face induces the secondary cracks in the non-banded face to propagate in the direction of the banding. This may suggest that the longitudinal growth of a SCC crack in pipelines is dominated by microstructural banding.



**Figure 4-36. Fracture surface of an as-received grade X100 specimen tested in the carbonate solution at 75°C and at an applied potential of – 720 mV (sce)**

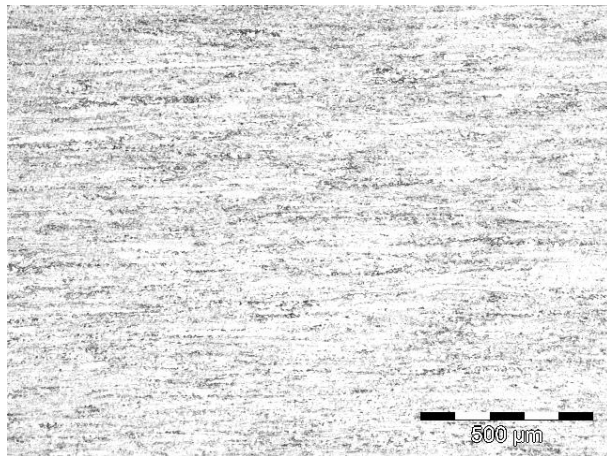


**Figure 4-37. A typical 'LT' face microstructure before loading**

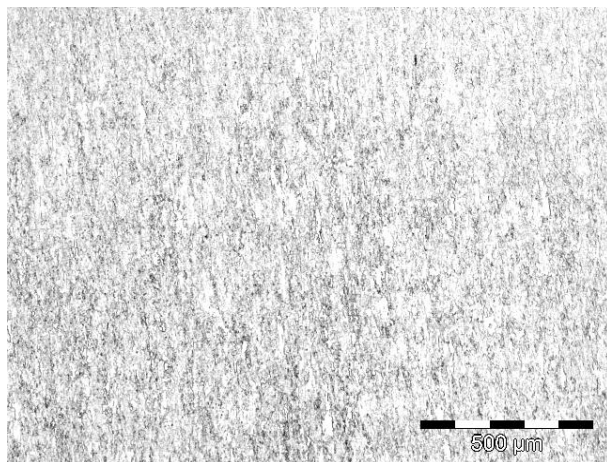


**Figure 4-38. A typical 'CT' face microstructure before loading**

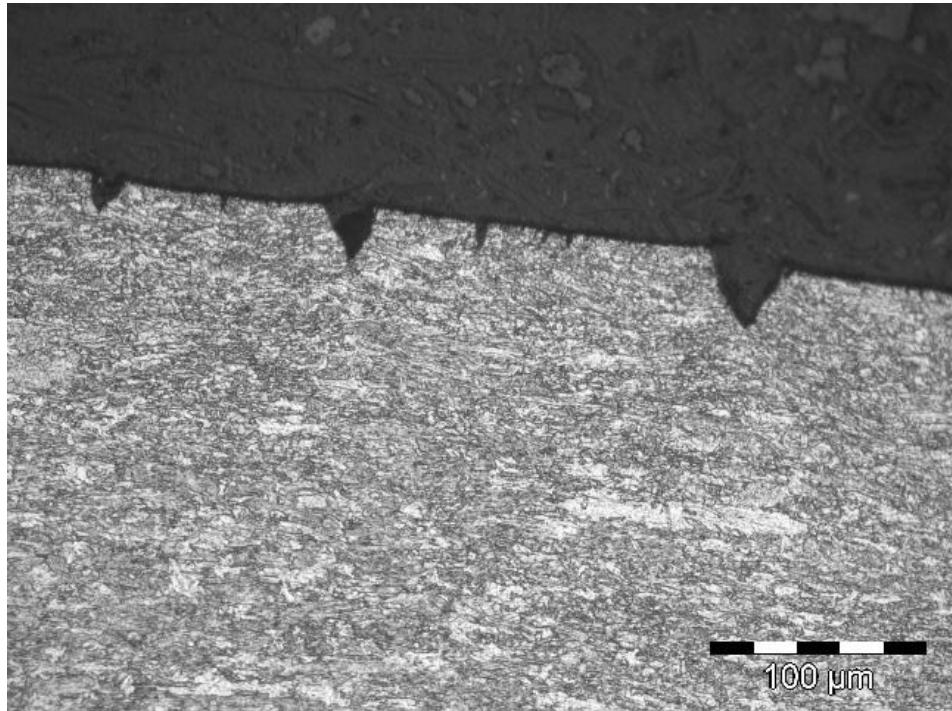


**Figure 4-39. Secondary cracks in the 'CL' face of the as-received X100 pipeline steel specimen tested in the carbonate solution at 75°C and an applied potential of -720 mV (sce).**

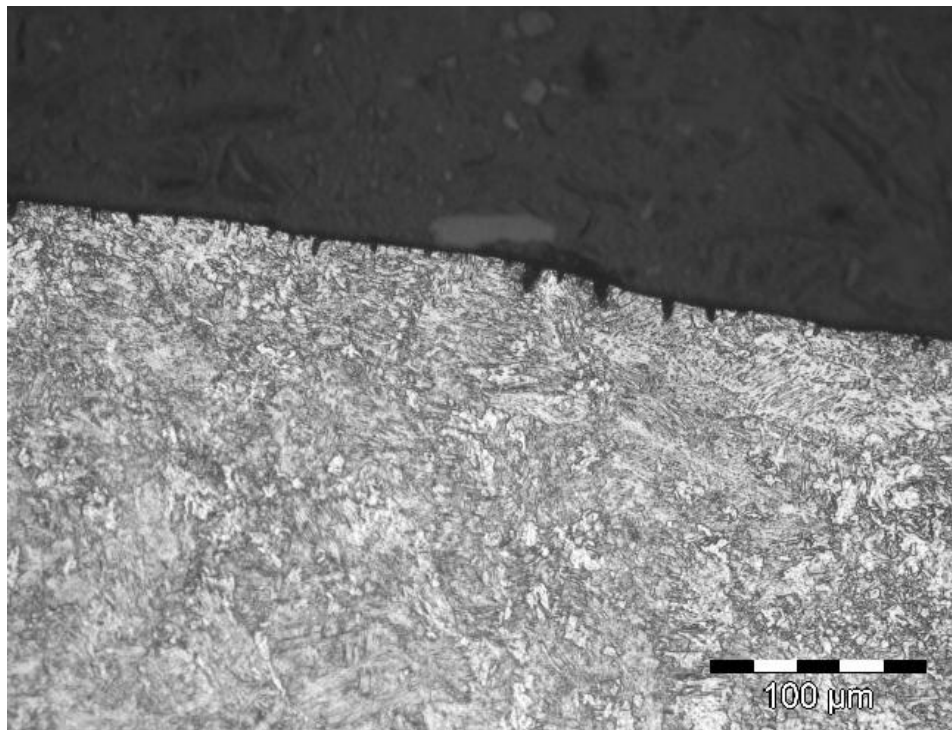


**Figure 4-40. Secondary cracks in the 'CT' face of the as-received X100 pipeline steel specimen tested in the carbonate solution at 75°C and an applied potential of -720 mV (sce).**

Figure 4-41 shows the % elongation of the as-received and the heat-treated specimens of the grade X100 alloy. The heat-treated specimens are much softer and ductile than the as-received. The specimens heat-treated at 1000°C are less susceptible when compared with those heat-treated at 1175°C as both have equal percent elongation in length (Figure 4-11).

Figure 4-42 compares the fracture stresses of the as-received and the heat-treated grade X100 alloy. The as-received is less susceptible than the heat-treated specimens, neglecting the ovality effect. The fracture stress plot agrees with the work of Wang and Atrens<sup>73</sup> on grade X65 steel that the lowest fracture stress in the IG SCC region was at the applied potential of – 600 mV (sce) and the fracture stress continues to decrease at potentials more negative than – 800 mV (sce). The comparison of the two fracture stresses plots demonstrates that the X100 is less susceptible to the carbonate solution than the grade X65 steel, although the method used in assessing the susceptibility was a linearly increasing stress test. The fracture stresses for the lower grade X65 across the studied potential range of – 550 mV to – 1000 mV fell below 550 MPa.

#### **4.2.4 Effect of serrations on the grade X100 steel**

All SSRTs conducted at a strain rate of  $2 \times 10^{-6}$ /s and a temperature of 75°C gave serrated load – time curves for the as-received material (Figure 3-14). The serrations are characterised by a series of sudden load drops followed by an increase with a slope similar to that of the elastic portion of the curve. The load drop in most cases starts just after the ultimate tensile load and its magnitude gradually increases to fracture. This phenomenon has been attributed to dynamic strain aging (DSA). The DSA process involves locking and unlocking of moving dislocation by solute atoms. The load must increase and when the dislocations are separated from the solute atoms there is load drop. This process occurs many times, causing the serrations in the stress-strain curve<sup>93, 107</sup>.

It has been shown that interstitial atoms like carbon and nitrogen interact with the strain field of dislocations in steel.



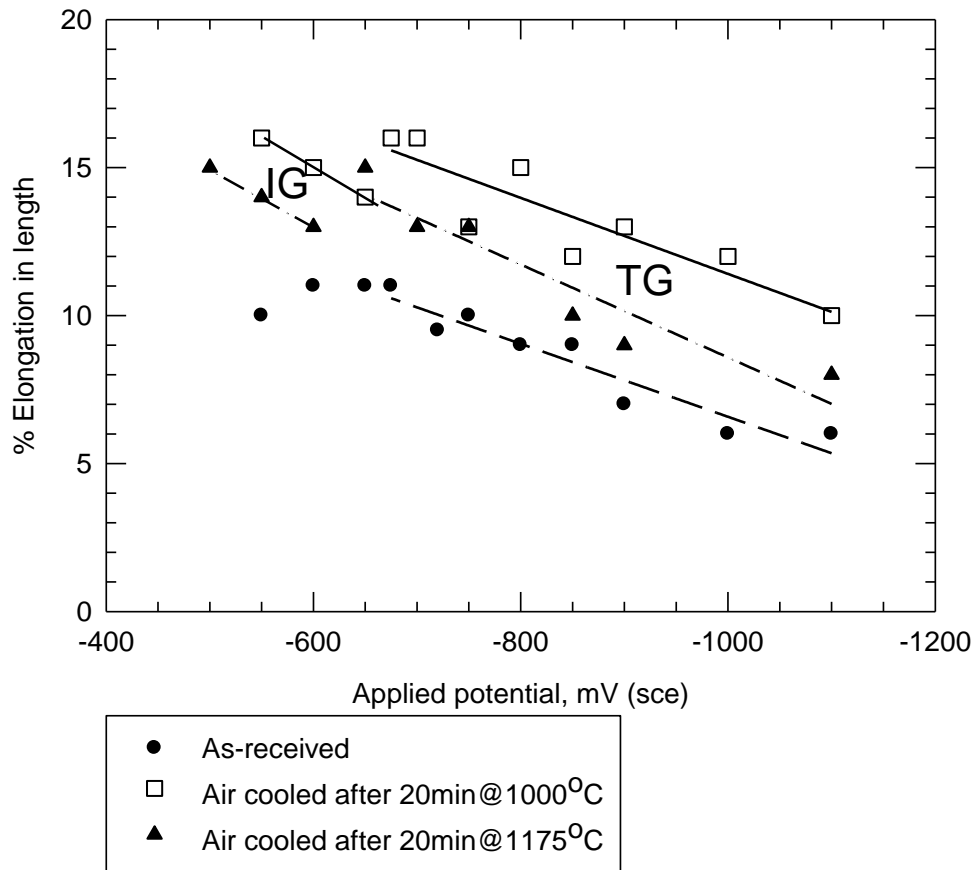


Figure 4-41. Variation of % elongation with potential for the grade X100

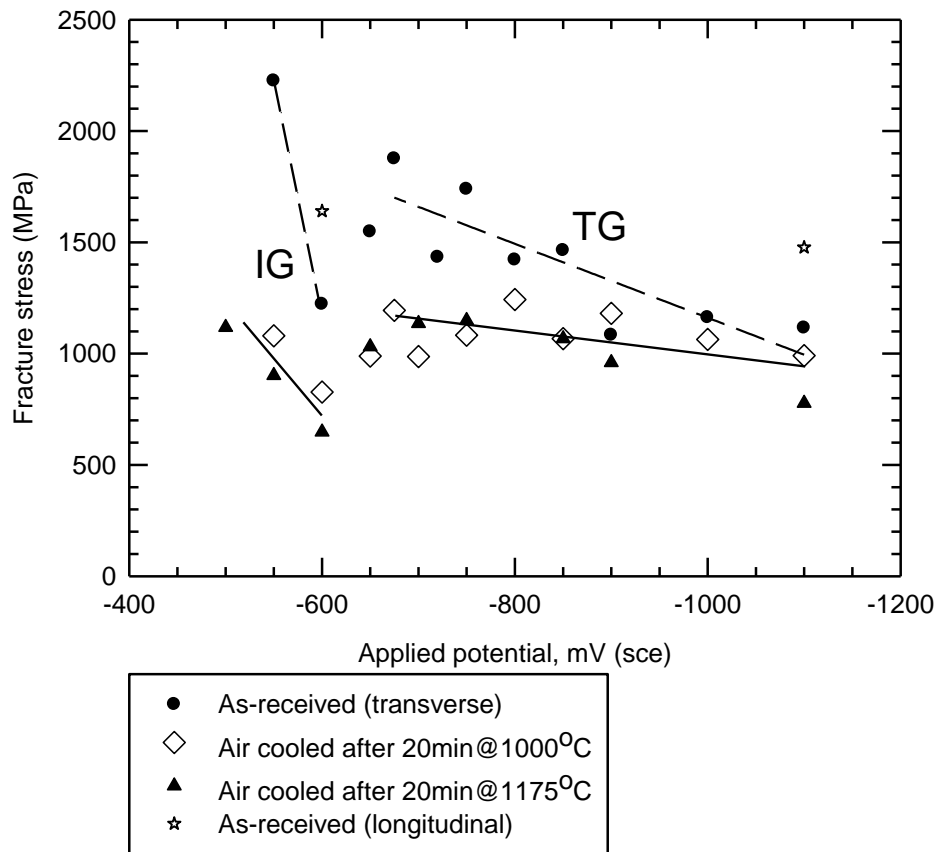


Figure 4-42. Variation of fracture stress with potential for the grade X100 steel

Dislocations can be locked in position by the formation of an interstitial atmosphere of either carbon or nitrogen in the vicinity of dislocations and may be freed by increasing stress or temperature causing further deformation<sup>107</sup>.

In an attempt to understand the cause of the serrations, a number of SSRTs were conducted to determine factors that affect the serrations. The results show that the serrations have nothing to do with whether tests were conducted in silicone oil or carbonate solution at 75°C since both give serrated flow curves. The magnitude of the load drop due to serrations increases with increasing temperature from 60 to 90°C and the phenomenon is thermally activated within this range and with activation energy of 39 KJ/mol (Figure 4-43) which is approximately half the activation energy of carbon and nitrogen diffusion in  $\alpha$ -iron (80 and 76 kJ/mol, respectively.)<sup>11</sup>. The serrations are also affected by strain rate (Figure 4-44). The size of the load drop due to serrations decreases as the strain rate increases. A test at a strain rate of  $3 \times 10^{-5}$ /s and a temperature of 75°C gave no serration which agrees with the thought that serration occurs at a matching combination of strain rate and temperature in a low carbon steel<sup>20</sup>. The serrations in the as-received material were completely removed by air cooling after 30 minutes at 600°C and the resulting microstructure is shown in Figure 4-45. This heat treatment removes carbon and possibly nitrogen out of solution and thus reduces the obstacles to dislocation within grains. The process of the removing carbon out of solution is quite noticeable at a slightly higher temperature of 700°C (Figure 4-46).

Figure 4-47 shows that removing the serrations increases the susceptibility of the alloy to secondary cracking in the carbonate solution at potentials more negative than – 800 mV (sce) but the degree to which the as-received (serrated) and the heat-treated (not serrated) embrittle is generally the same (Figure 4-48). Figure 4-49 compares the secondary and the primary crack velocities of the specimen heat-treated to remove serrations. The figure agrees with Figure 4-26 that the primary cracks are generally bigger than the secondary cracks and the two are the same within the potentials range – 700 to – 850 mV (sce). The increase in susceptibility to secondary cracking is because of change in microstructure as a result of the tempering which removes carbon out of solution and diffuses towards the grain boundaries (Figure 4-46).

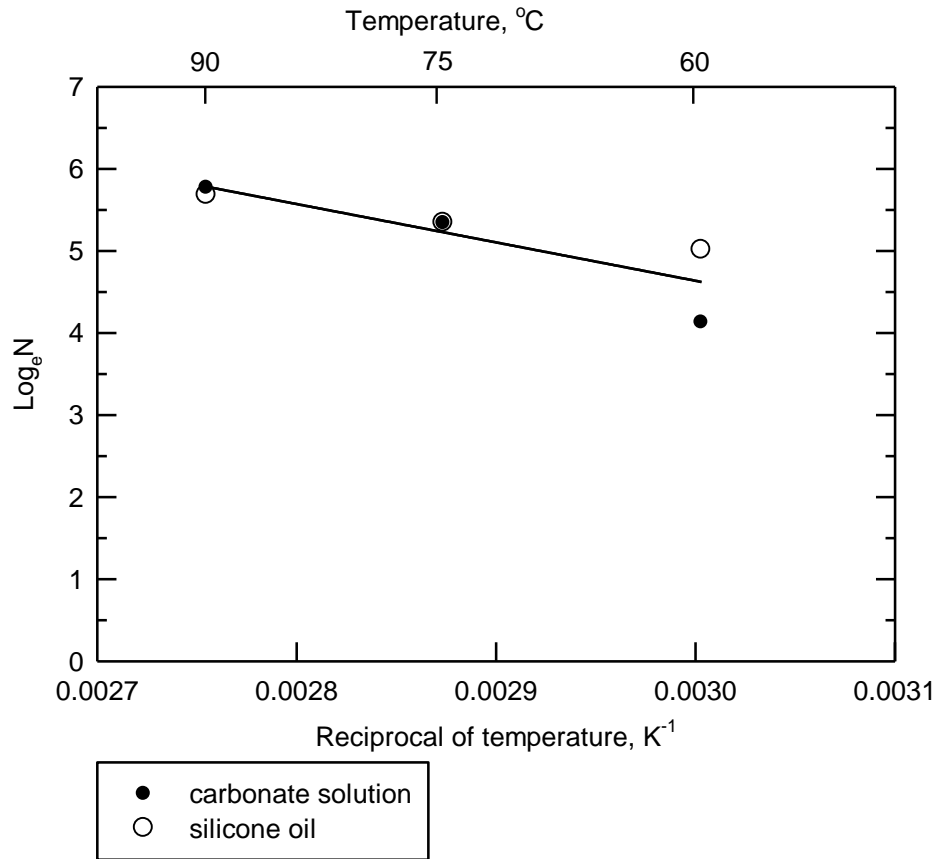


Figure 4-43. Variation of load (N, in Newton) drop due to serrations with test temperature. All tests in the carbonate solution were at an applied potential of  $-900$  mV (sce).

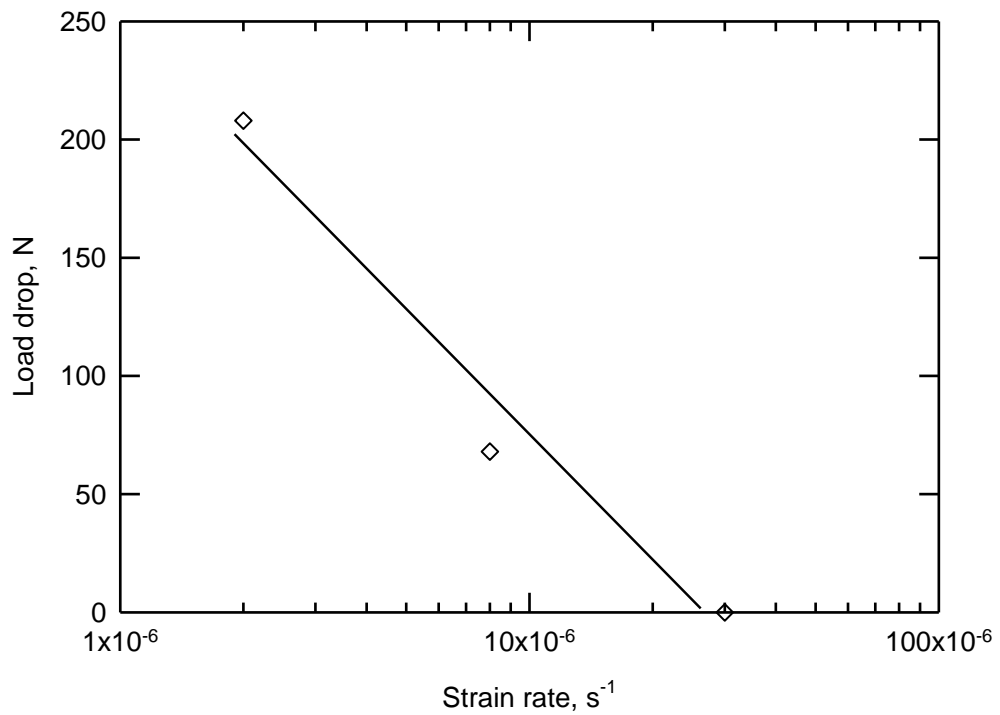
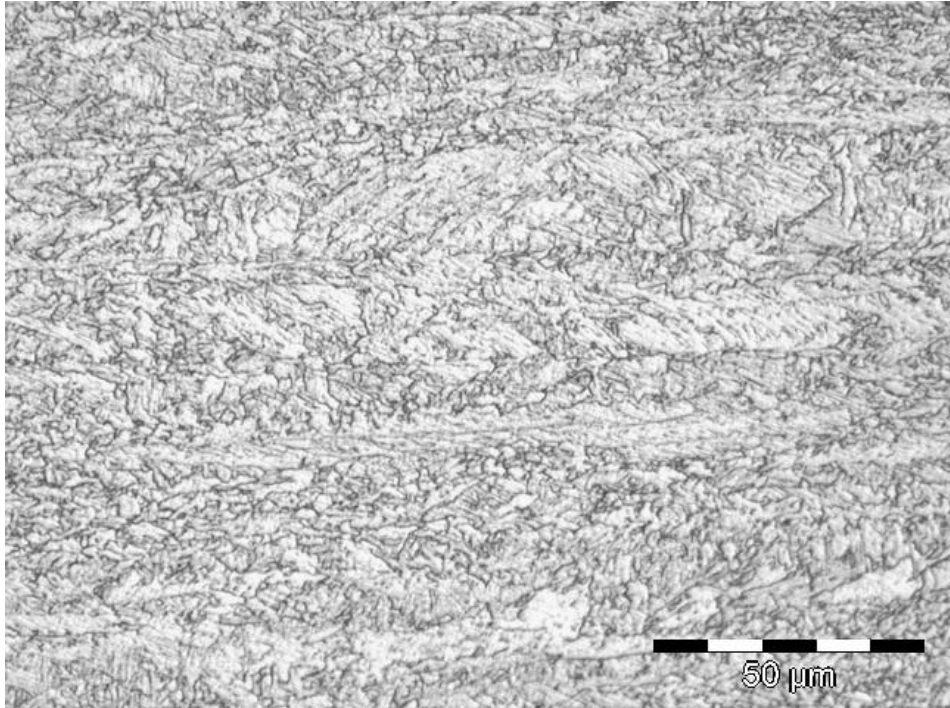
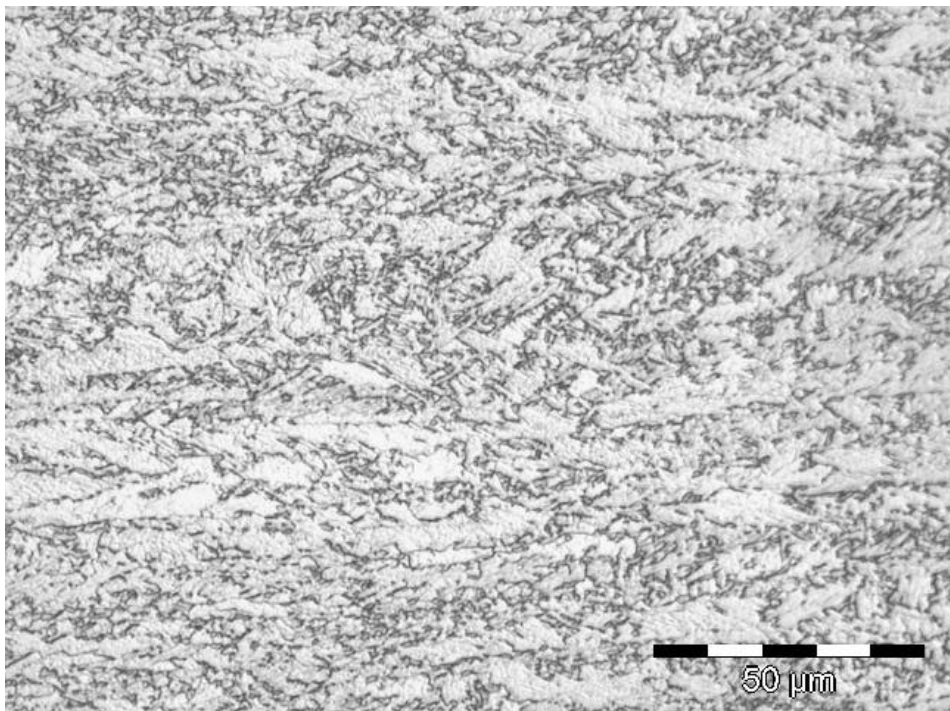


Figure 4-44. Effect of strain rate on load drop due to serrations for tests in the carbonate solution at  $75^{\circ}\text{C}$  and an applied potential of  $-900$  mV (sce)



**Figure 4-45. 'LT' face microstructure of a grade X100 specimen air cooled after 30 min. at 600°C**



**Figure 4-46. 'LT' face microstructure of grade X100 specimen air cooled after 30 min at 700°C**

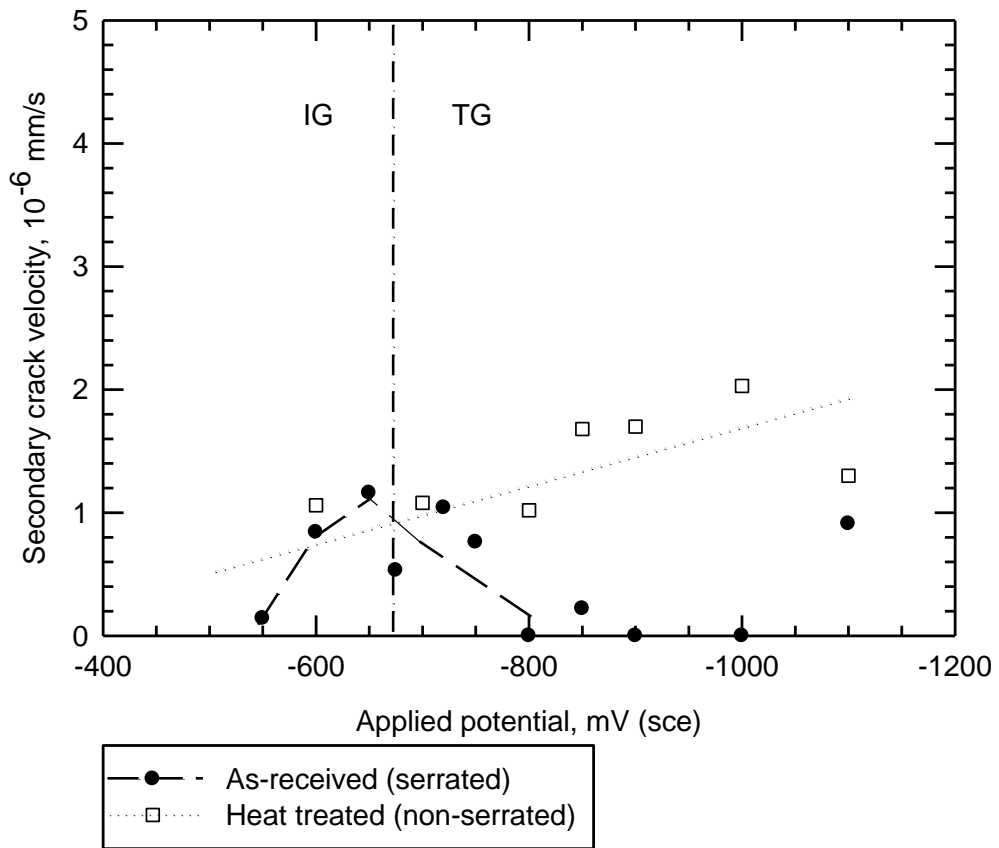


Figure 4-47. Crack velocities of the as-received grade X100 compared with that of specimens air cooled after 30min at 600°C

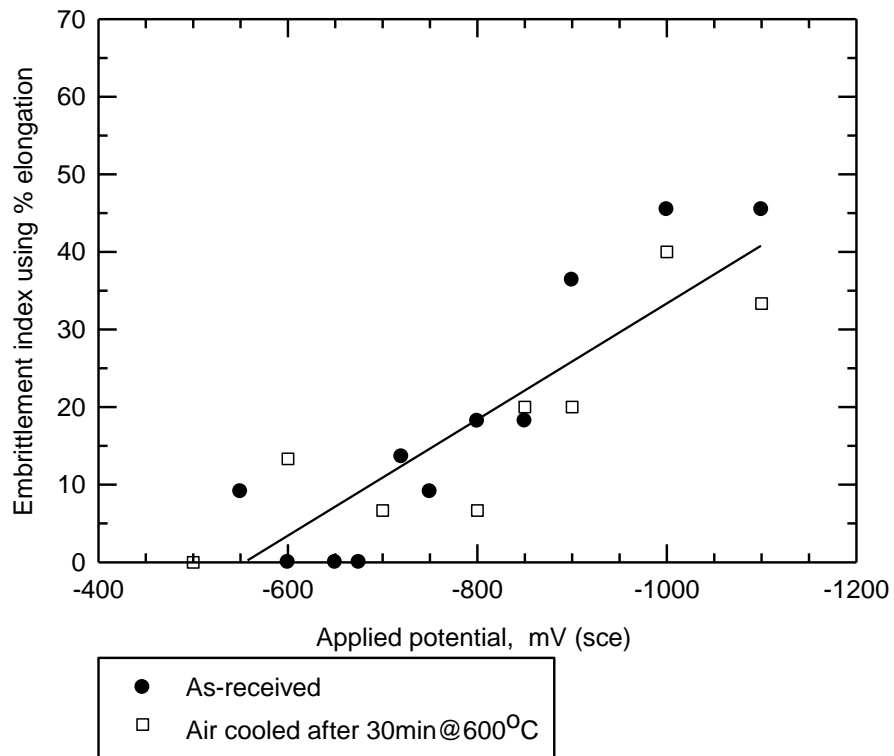


Figure 4-48. Variation of embrittlement index (% elongation) with potential of the as-received grade X100 compared with that of specimens air cooled after 30min at 600°C

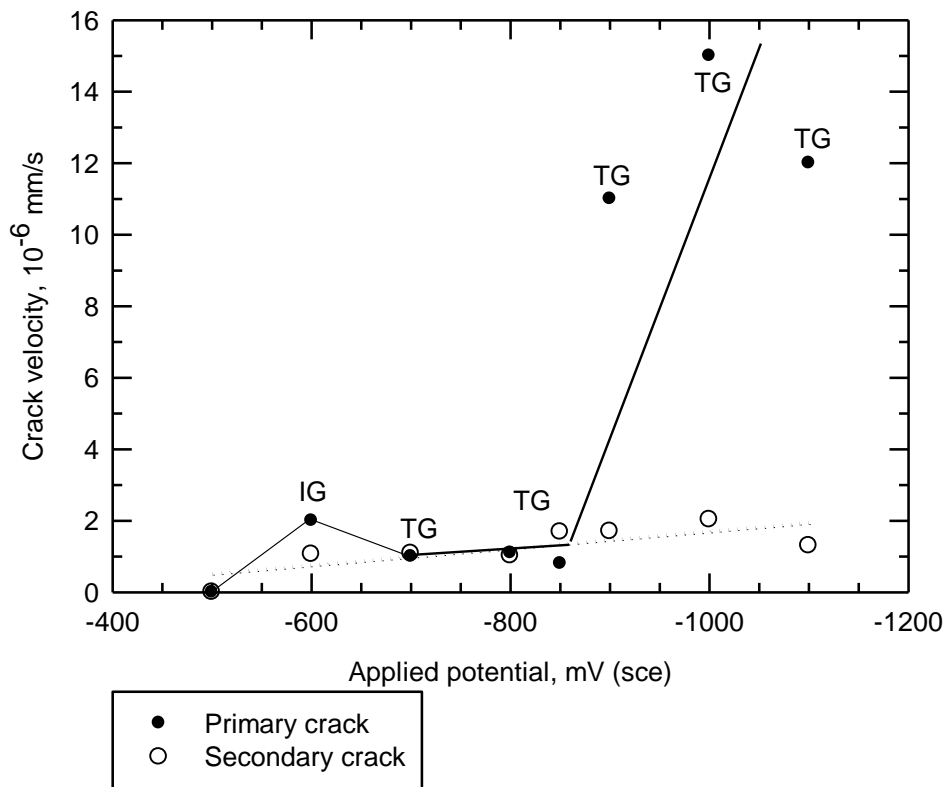


Figure 4-49. Variation of primary and secondary crack velocities with potential for the heat treated (air cooled after 30min at 600°C) grade X100 pipeline steel in the carbonate solution at 75°C.

#### 4.2.5 Susceptibility of the as-received X80 and X100

The performance of the as-received X100 was compared with that of the API 5L, grade X80. The secondary crack velocities and the embrittlement indices measured using both the % elongation in length and the % reduction in area are shown in Figure 4-50, Figure 4-51 and Figure 4-52. The grade X100 behaved in a similar way to the X80 but it is slightly less susceptible to the carbonate solution within the SCC potential range (Figure 4-50). However, the embrittlement indices (Figure 4-51 and Figure 4-52) demonstrate that the grade X100 is less susceptible to the environment across the whole potential range studied.

#### 4.2.6 Susceptibility of the as-received X80 and its HAZ

Figure 4-53 compares the susceptibility of the as-received grade X80 parent metal and its seam-weld HAZ in the carbonate solution. The seam-weld HAZ is slightly

more susceptible between the potential range of  $-600$  to  $-1000$  mV (sce) whereas the embrittlement index (Figure 4-54) demonstrates that the susceptibilities of the parent metal and the seam-weld are almost the same. The fitted embrittlement index sharply rises from the potential of  $-500$  mV to  $-650$  mV (sce) and then continues to rise at a reduced gradient up to  $-1100$  mV (sce). The change in slope may be due to the change in cracking mode from IG to TG between the potentials of  $-600$  to  $-700$  mV (sce).

#### **4.2.7 SSRT in sodium nitrate**

Figure 4-55 shows IG cracks in an as-received grade X100 specimen tested in the nitrate solution at a potential of  $-350$  mV (sce). A maximum IG crack of  $117\ \mu\text{m}$  was recorded at this potential which is almost twice that recorded in the carbonate solution at a potential of  $-650$  mV (sce). This demonstrates that the alloy is more susceptible to IG cracking in the nitrate solution than in the carbonate solution. SSRTs in the two solutions indicate that the peaks for IG cracking in the respective solutions occur at the above mentioned two potentials.

Figure 4-56 compares the embrittlement indices of the grade X100 steel in the carbonate and the nitrate solution. The figure demonstrates that the alloy is more susceptible to the nitrate solution than the carbonate solution. Figure 4-57 also shows the embrittlement indices for the alloy in the two solutions which were calculated using % elongation and it agrees with the result shown in Figure 4-56.

The above three figures all suggest that the grade X100 steel is more susceptible to IG cracking and embrittlement in the nitrate than the carbonate solution. This agrees with a previous work<sup>81</sup> which compared the susceptibility of a pipeline steel to the two solutions in terms of current density and time to failure ratio.

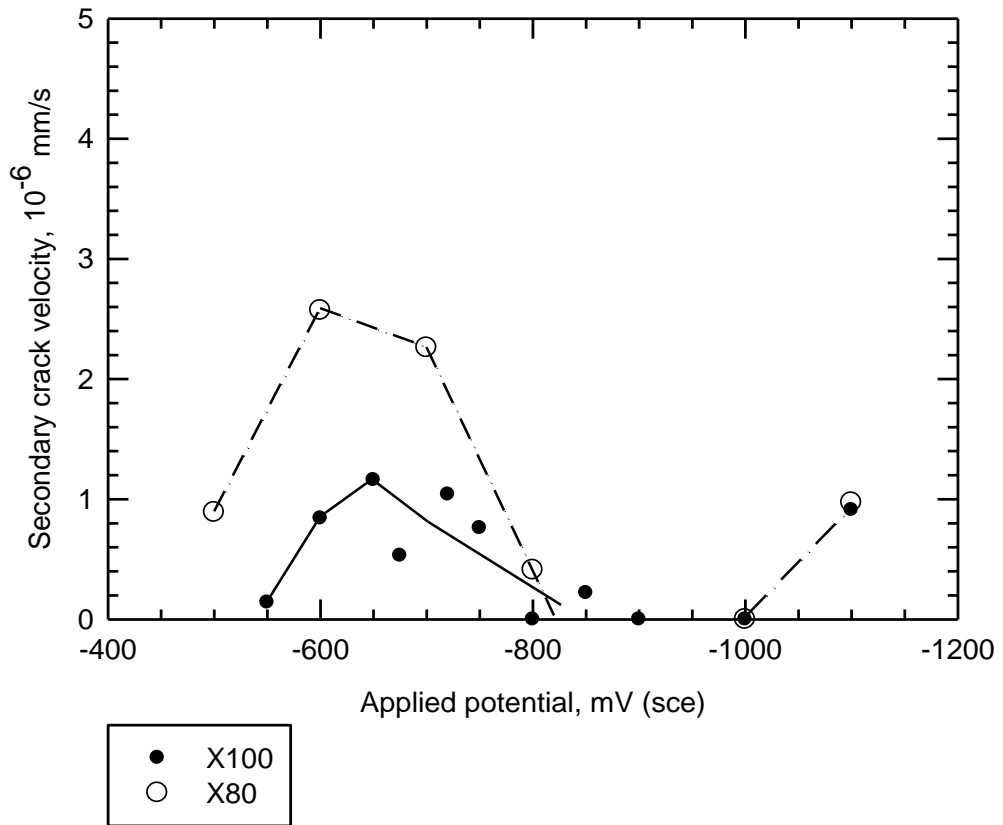


Figure 4-50. Crack velocities of the as-received X80 and X100

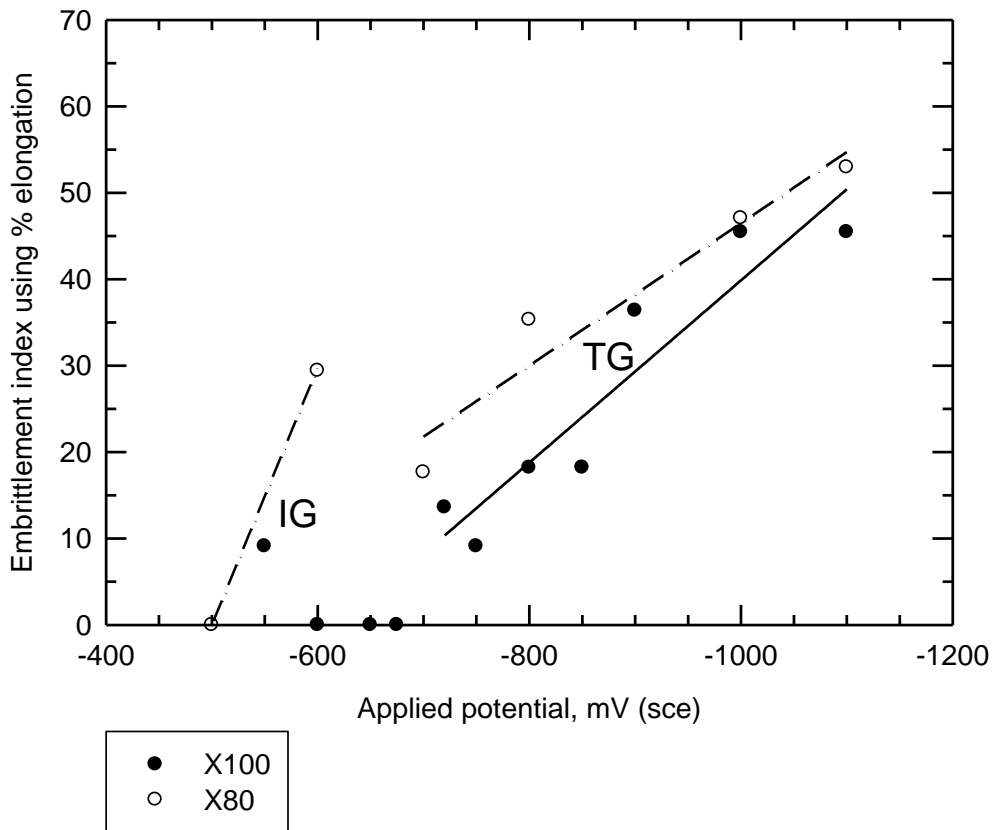


Figure 4-51. Variation of embrittlement index (% elongation) with potential for the as-received X80 and X100



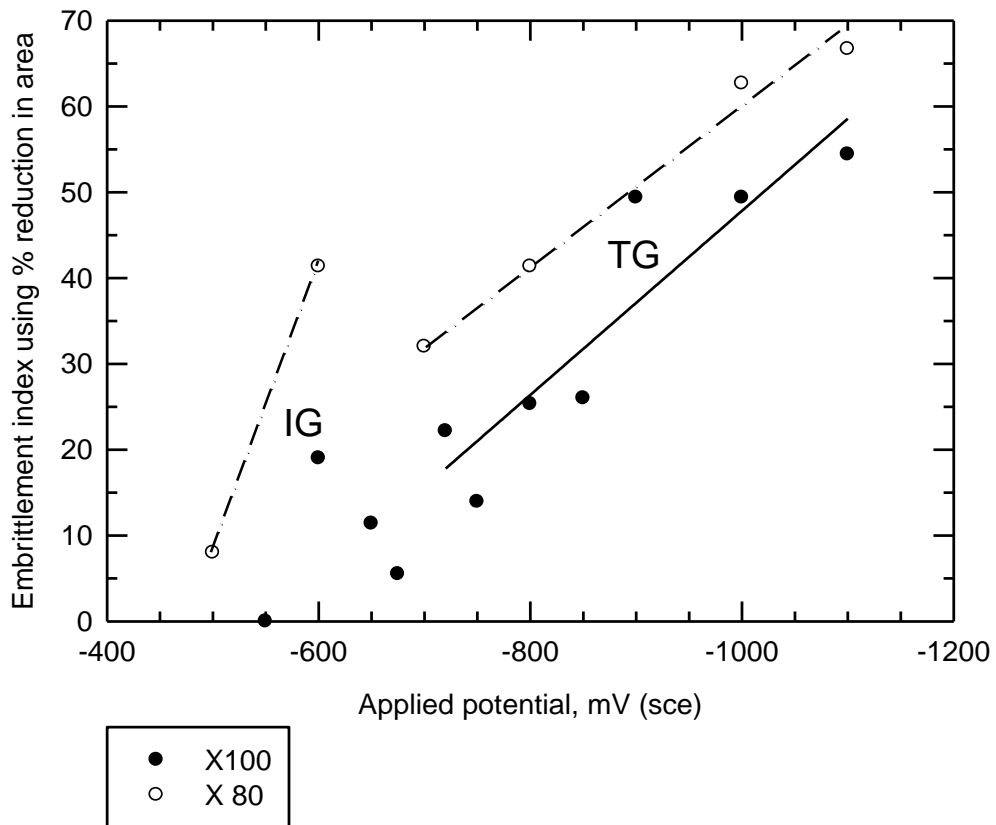


Figure 4-52. Variation of embrittlement index (% reduction in area) with potential for the as-received X80 and X100

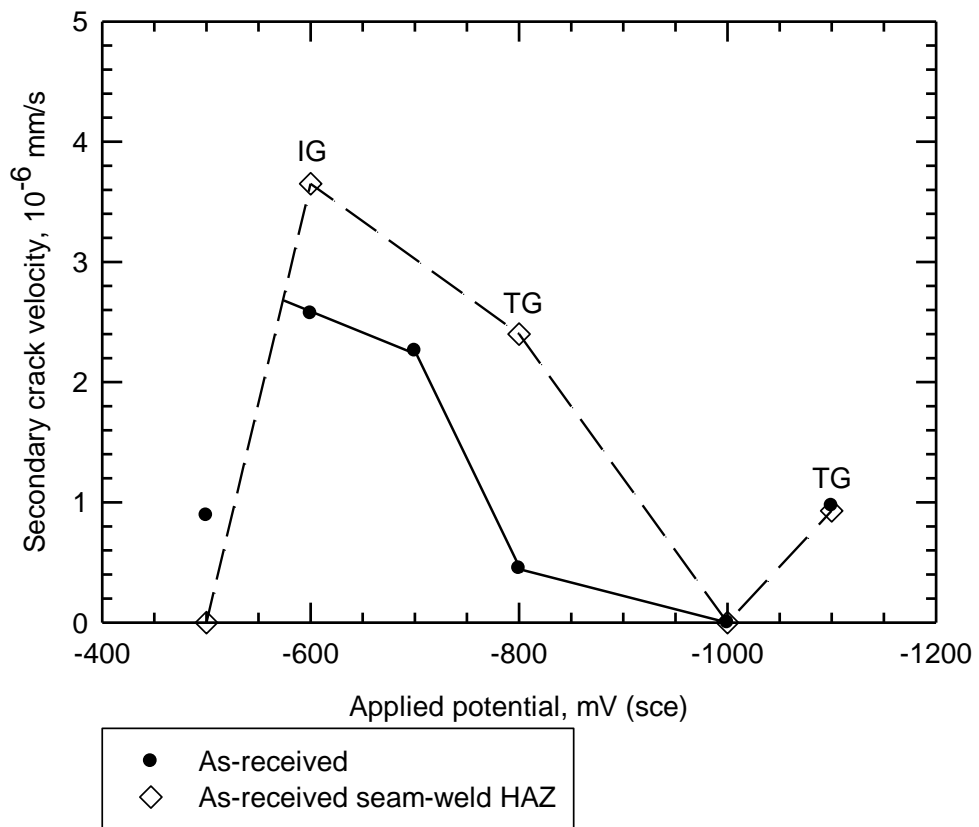


Figure 4-53. Crack velocities of as-received grade X80 compared with that of its seam-weld HAZ

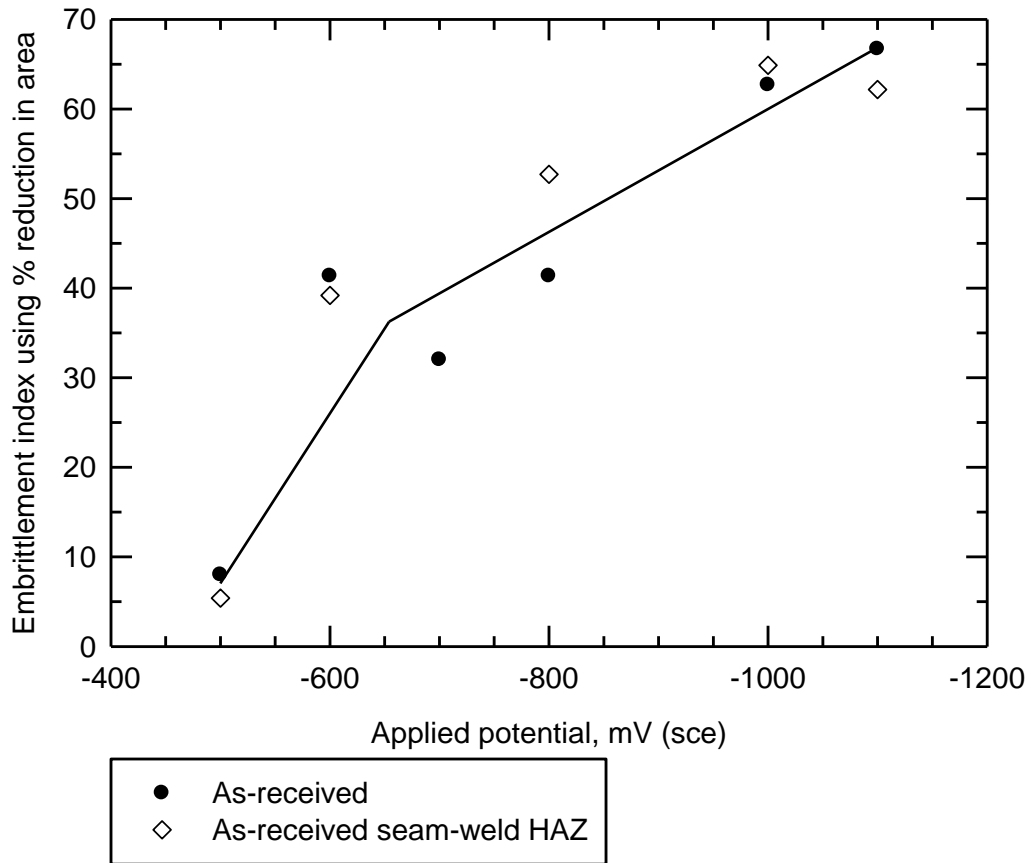


Figure 4-54. Variation of embrittlement index (% reduction in area) with potential for the as-received grade X80 compared with its seam-weld HAZ

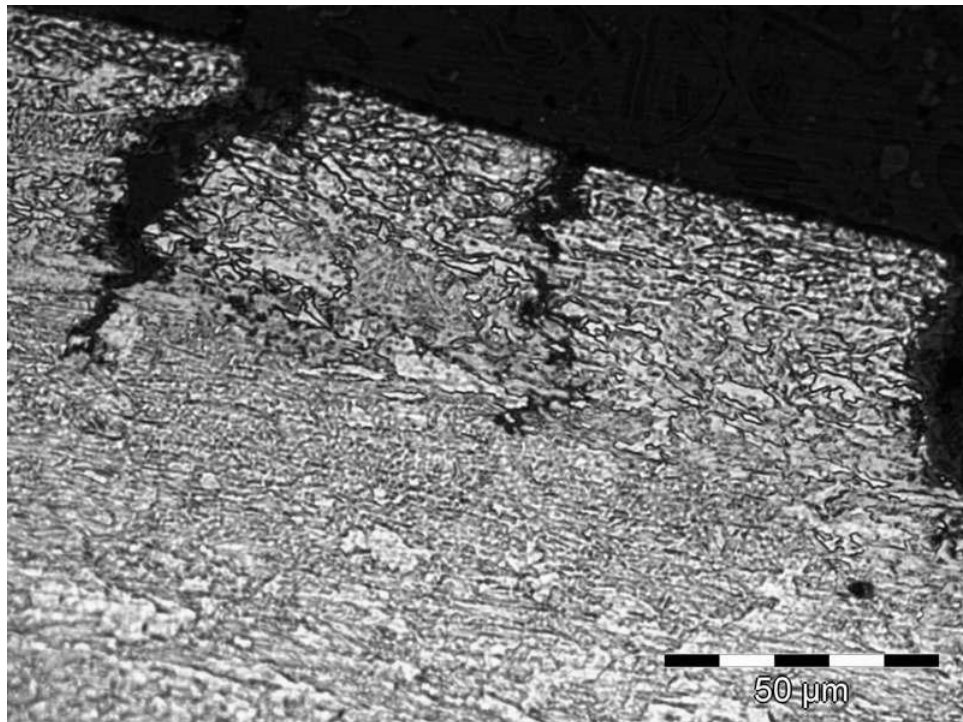


Figure 4-55. IG secondary cracks in an as-received grade X100 steel tested in 4 M sodium nitrate solution with 1 %  $K_2Cr_2O_7$  at 75°C and an applied potential of - 350 mV (sce)

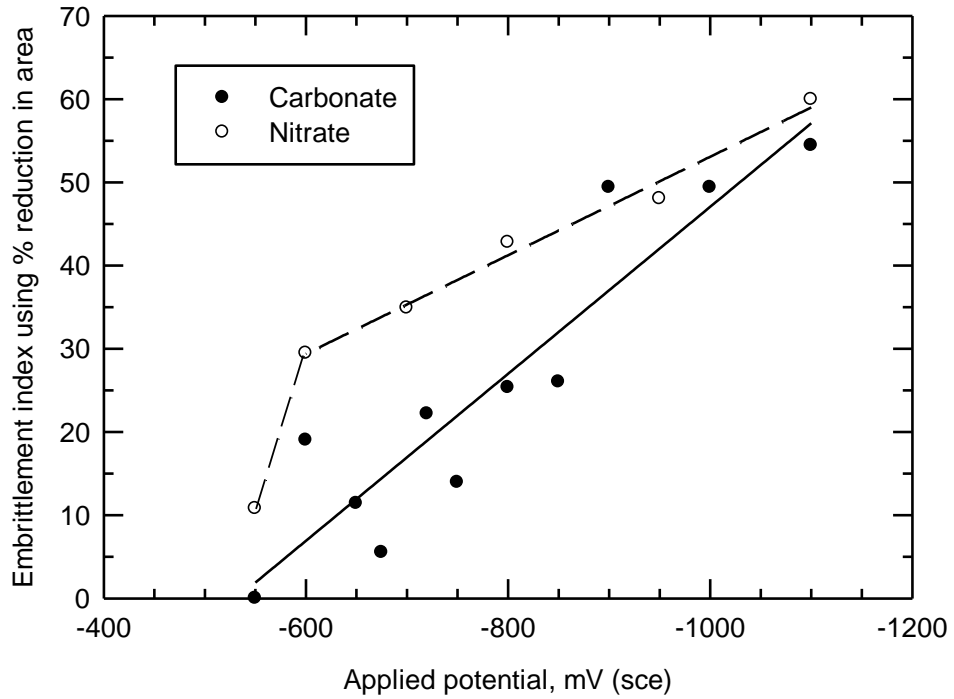


Figure 4-56. Variation of embrittlement index (% reduction in area) with potential of the as-received grade X100 tested in carbonate solution compared with that of the nitrate solution

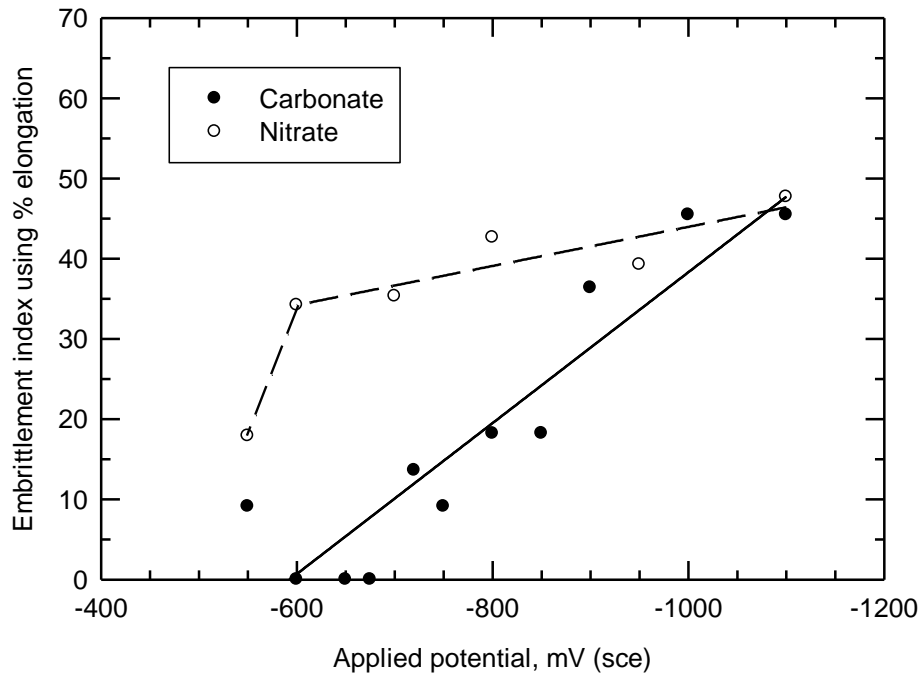


Figure 4-57. Variation of embrittlement index (% elongation) with potential of the as-received grade X100 tested in carbonate solution compared with that of the nitrate solution

## Chapter 5 : DISCUSSION

### 5.1 Introduction

The prime aim of this work was to compare the relative susceptibility of the as-received parent metal, weld and simulated HAZ microstructures of grades X80 and X100 pipeline steels to environment-assisted cracking (EAC). The research question in this aim is: what effect does the alteration to the as-received microstructures due to welding have on their susceptibility to EAC? The as-received microstructures are the products of controlled-rolling and accelerated cooling processes that are very difficult to achieve even with post-weld heat treatments. The microstructure of the grade X100 is very fine grained, consisting basically of carbide distributed in ferrite (Figure 3-3). However, such a microstructure in a steel of similar chemical composition and heat treatment has previously<sup>68, 108, 109</sup> been called acicular ferrite, especially when viewed in the 'LT' face. It is a product of fast cooling of austenite that has been heavily hot-rolled to a temperature close to the upper transformation temperature (~ 800°C for the grade X100 with the composition given in Table 3-2) and then rapidly cooled to a temperature just below the lower transformation temperature. The microstructure of the grade X80 is predominantly ferrite/pearlite microstructure (Figure 3-2).

The second aim was to compare the susceptibility to EAC of the as-received microstructure of the newly developed grade X100 with existing grades. This aim was set to determine whether the reduction in pearlite content, grain refinement and a micro-alloying coupled with accelerating cooling associated with the production of the as-received microstructure of the grade X100 led to a decrease in susceptibility to EAC.

The third aim of this work was to investigate the role of carbon and manganese in the formation and removal of microstructural banding in pipeline steels. This involves an investigation of the effect of banding on EAC. Pipeline steels are heavily hot-worked (controlled-rolling) to refine grain size and thus the average band spacing is reduced. This led to a hypothesis that the combined effect of the grain refinement and the

reduction in inter-band spacing may result in reducing the time and temperature required to remove segregation (banding) through diffusion.

## **5.2 Effect of potential on susceptibility to cracking**

Figure 4-24 indicates that the susceptibility to secondary cracking of both as-received and simulated HAZ microstructures varies with potential. Generally two modes of cracking were observed: film-associated SCC which occurs anodic to the free corrosion potential (FCP) and hydrogen associated cracking (hydrogen embrittlement) which occurs cathodic to the FCP. The film-associated SCC is also divided into IG and TG regions depending on the types of film (Table 4-3) involved in the process. Figure 4-24 also compares the susceptibility of the as-received microstructure with that of the two simulated microstructures shown in the Figure 4-23 whose microstructures are: typical pearlite/ferrite and Widmanstätten structure. The figure demonstrates that the heat treatment increases the susceptibility of the as-received microstructure to IG cracking. However, susceptibility of the three microstructures to secondary TG cracking in both the SCC and hydrogen associated secondary cracking is basically the same allowing for the scatter in the plot, although the as-received microstructure in this region relatively appeared to be less susceptible to secondary cracking. The variation of secondary crack velocity with potential indicates that the three microstructures are more susceptible to IG secondary cracking than hydrogen-associated cracking. However, Figure 4-26 and Figure 4-49 demonstrate that the susceptibility to the cracking at potentials more negative than  $-800$  mV (sce) is best measured by the primary crack from fracture surfaces; because generally in the TG region there are few secondary cracks (Figure 5-1) to allow measurement of susceptibility. The embrittlement index plot (Figure 4-32) agrees with primary crack velocity data and it shows that the microstructures are more susceptible to hydrogen embrittlement than SCC.

The increase in susceptibility is mainly due to the change in microstructure as a result of the heat treatment. The heat-treated microstructures have equiaxed grains whereas the as-received grains are highly elongated and deformed and such grains deflect the growth of IG cracks (Figure 4-1) and hence resist the growth of IG SCC crack. Another change to the as-received microstructure due to the heat treatment is

the removal of carbon from solution and the increase in the sizes of carbide precipitates and pearlite in the heat treated microstructures.

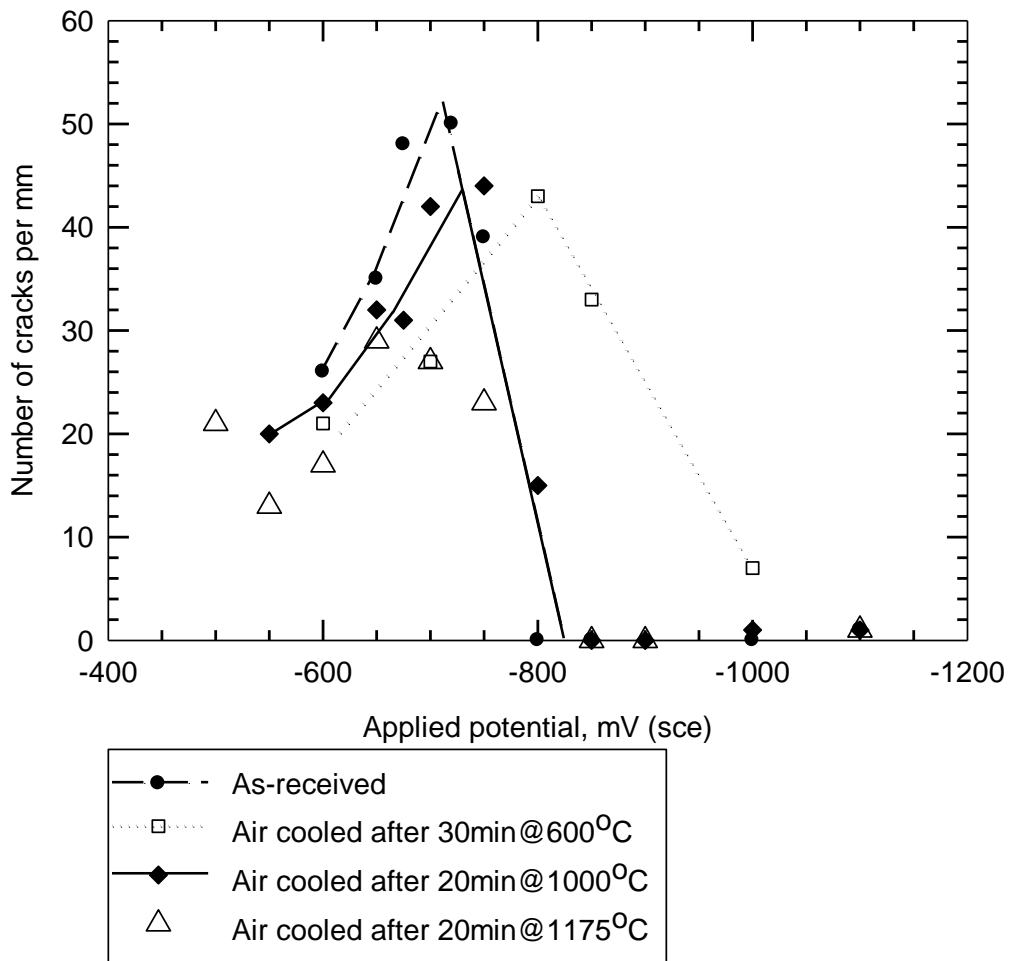


**Figure 5-1. Secondary crack frequency on the gauge length at more than 1 mm from the fracture surfaces measured from SSRT on the grade X100 pipeline steel in the 1 M sodium hydrogen carbonate / 0.5 M sodium carbonate solution at 75°C**

The above variation of susceptibility to cracking and embrittlement in the carbonate solution across the studied potential range is generally in agreement with the literature<sup>71, 74, 110, 111</sup>. SCC anodic to the FCP and hydrogen embrittlement, cathodic to the FCP is in agreement with works carried out in a number of steels<sup>71, 73, 74, 110, 111</sup>; annealed carbon steel with a pearlite/ferrite microstructure<sup>110</sup> tested at 90°C in which the susceptibility was measured in terms of % RA and the microstructure of the steel was found to be more susceptible to SCC than the cathodic potential hydrogen embrittlement. The susceptibility at the FCP was minimum; whereas the grade X100 microstructure embrittles at the FCP more than it does within the SCC potential

range. However, in the secondary crack velocity plot, the crack velocity is minimum at the FCP. In a number of heat-treated carbon steels both IG and TG cracks have been reported<sup>111</sup> in the carbonate solution at 95°C and the susceptibility at more cathodic potential to the SCC range was considered as hydrogen embrittlement. Similar conclusions were drawn for pipeline steels of: grade<sup>74</sup> X52, grade<sup>73</sup> X65 and grade<sup>71</sup> X70. The embrittlement index plot of the grade X100 agrees with that of the grade X70 whose microstructure was reported<sup>71</sup> as acicular ferrite. The peak of intergranular cracking (Figure 4-24) is at a potential of – 600 mV (sce) which agrees with previous work<sup>73</sup> on pipeline steel of lower grade X65.

This work has identified four types of film that are associated with the anodic susceptibility of the as-received microstructure of the grade X100 and the film appearance varies with potential (Table 4-3) within the SCC range. There are published works<sup>103, 106</sup> on the chemical composition of films associated with anodic SCC but such works did not show the variation of film morphology with potential and thus the association of a morphology with a particular mode of cracking. The change in the film morphology with potential might be connected to a variation in the relative composition of magnetite and siderite in the film. The pseudo-cubic film is the most conductive (judging from the fast sweep anodic polarization curve, Figure 4-18) and induces least secondary cracking. A proper characterisation of the film could provide more information on the understanding of the effect of film on SCC mechanisms. An investigation of the variation of film morphology with applied potential was conducted only on the as-received microstructure. For example IG cracks were observed at a potential of – 650 mV (sce) in both the as-received microstructure and ferrite/pearlite microstructure of the specimens heat treated at 1000°C whereas in the Widmanstätten structure TG cracks were observed. A previous report<sup>74</sup> has indicated that a shift in test temperature from 50°C to 75°C changed the mode of cracking from IG to TG in a single microstructure indicating that a temperature change is also a factor. The change in cracking mode at this potential due to a change in test temperature has been reported<sup>50</sup> but the change due to microstructure has been given little or no attention in the literature. Many researchers over the years have chosen a potential of – 650 mV (sce) alone to compare the susceptibility of a number microstructures<sup>3, 112-114</sup>. If this comparison of the three microstructures (Figure 4-24) had been carried out in this work at a

potential of  $-650$  mV (sce) the conclusion would have been directly opposite (the most susceptible microstructure would be the least susceptible). The best approach is to predict the most susceptible potential for each microstructure as demonstrated in the following literature<sup>63, 73, 75, 82, 110</sup>. Moreover, Wang and Atrens<sup>73</sup> indicated that the potential range for SCC varies with pipeline steel grade as well as temperature.

### **5.3 Effect of microstructure on susceptibility to IG SCC**

Figure 4-25 shows that the susceptibility to IG cracking depends more on microstructure than average grain size. It compares the susceptibility to IG cracking of four simulated HAZ microstructures and a seam weld. The four simulated microstructures are: a tempered region which is basically a ‘spheroidised’ structure where the tempering at  $600^{\circ}\text{C}$  has removed some carbon from solution; a partially austenitised region where enough carbon has come out of solution and coalesced to form spheroidised carbides; a zone of recrystallization where the microstructure underwent complete transformation and the deformed grains have fully recrystallised to an equiaxed shape; and the fourth simulated microstructure is the grain growth microstructure which basically consists of large grained Widmanstätten structure. The seam weld is comprised of weld metal, HAZ and the base metal.

Figure 4-25 demonstrates that: (1) the as-received microstructure is less susceptible than the heat-treated microstructures; (2) the as-received microstructure is also less susceptible when compared with the seam-weld HAZ microstructure and hence the welding heat increases the susceptibility of the as-received microstructure to IG cracking. This observation disagrees with the work of Mitsui et al.<sup>75</sup> which indicates that the susceptibility of the HAZ microstructure is less than that of the parent metal microstructure. The pearlite/ferrite distribution of the parent metal was improved by the welding making it less susceptible to IG SCC, whereas the fine grained and accelerated cooled, as-received microstructure of the grade X100 was worsened by welding making it more susceptible to IG SCC. The comparison of the as-received microstructure of the grade X80 and its seam-weld HAZ to IG cracking in the carbonate solution (Figure 4-53) agrees with the result of the grade X100 that the welding heat increases the susceptibility of the as-received microstructures to IG



cracking. This also agrees with the work ( in a low pH solution ) of Lu and Luo<sup>115</sup> that welding reduces the resistance of pipeline steels to SCC and the effect is more pronounced in higher strength steels (X70, X80 and X100)

#### **5.4 Susceptibility of grade X80 compared with that of X100**

Figure 4-50 demonstrates that the as-received microstructure of grade X100 is less susceptible to SCC than the as-received microstructure (fine-grained pearlite/ferrite) of the grade X80. The latter microstructure is more susceptible to embrittlement at potential cathodic to the SCC region (Figure 4-52). The two figures suggest that the microstructure of the grade X100 is generally less susceptible to cracking across the potential range studied. This agrees with the literature<sup>116</sup> that reduction in carbon content decreases susceptibility to SCC. Although, the grade X100 is harder and stronger than the grade X80, Figure 4-52 indicates that the latter is more susceptible to hydrogen embrittlement in the carbonate solution. This agrees with the work of Pussegoda and Tyson<sup>109</sup> who compared the resistance to hydrogen embrittlement of two microstructures with different hardness and yield strength and concluded that the harder and the stronger microstructure (refined acicular ferrite with approximately similar composition and heat treatment with the grade X100) was found to be less susceptible to hydrogen embrittlement. A similar conclusion was reached by Barsanti et al.<sup>117</sup> that hydrogen embrittlement of pipeline steels does not depend on their strength but rather on their microstructures. This agrees with the suggestion of Thompson and Bernstein<sup>118</sup> that strength is not a reliable indicator of susceptibility to hydrogen. The microstructure of the grade X80 is more pearlitic than the microstructure of the grade X100 and reduction in pearlite content (pearlite content directly depending on carbon content) has been linked with reduction in susceptibility to SCC<sup>3, 69, 115</sup>.

#### **5.5 Effect of carbon and manganese on banding**

Section 4.1.1 of this work indicates that pearlite band forms where manganese concentration is high and the best approach to measure the difference in the concentration of manganese in the bands of pearlite and ferrite using an EDX

microanalysis was found to be area analysis (Figure 4-4) when compared with spot analysis, line scan and elemental mapping.

This is in agreement with previous results<sup>33, 36, 90, 119</sup> that manganese segregation is associated with the formation of ferrite/pearlite banding in hypoeutectoid steels. In a slow cooling process carbon segregates to regions of higher manganese. This segregation in steels occurs during solidification and is then rolled into bands during hot working operations.

Mapping has been carried out with microradiography<sup>90</sup>. The area analysis gives a good average of the concentration of manganese in a band as the concentration varies even within a band (Figure 4-6). The presence of ferrite crystals even within a band of pearlite and slight peaks of manganese concentration<sup>120</sup> at grain boundaries of the grade X65 probably explains the scatter associated with line scans and spot analyses. In a spot analysis there is a possibility that the electron beam will strike a ferrite grain within a pearlite band. The limitation of the area and spot analysis is that the actual position of the bands must be known. The whole analysis is further complicated by the penetration of the electron beam into the sample making comparison of surface microstructure with elemental concentration difficult.

## **5.6 Effect of heat treatment on banding**

Sections 4.1.1.1 and 4.1.1.2 of this work indicate that banding formation and removal from the pipeline steel depends on heat treatment temperature, soak time and cooling rate. Slow cooling from austenitic temperatures gives intense banding (provided the average grain size is less than approximately twice the average band spacing) and the intensity decreases with increasing cooling rates. Banding is completely removed by quenching or air cooling from a higher temperature (Figure 4-7). The fast cooling suppresses the diffusion of carbon from the region of low manganese concentration to the region of higher manganese concentration during the transformation temperature interval between the  $A_{r3}$  and the end of pro-eutectoid ferrite formation. Band removal by homogenisation of manganese through diffusion requires a longer time and a higher temperature than for carbon (Figure 4-8 and Table 4-2). A nearly

complete homogenisation of manganese was achieved by furnace cooling after 5 hours at 1175°C and this removed pearlite banding completely through grain growth. The average grain size was refined by air cooling after 20 minutes at 950°C without the return of pearlite banding (Figure 5-2).

The above observation is broadly consistent with the major trends in the literature and as to the removal of banding through quenching or air cooling from higher temperature agrees with the findings of Wilms<sup>39</sup> and Großerlinden et al.<sup>121</sup>.

The homogenisation of manganese through high temperature diffusion agrees with the literature<sup>37, 38, 90</sup> but in this work homogenisation was achieved at a lower temperature than ever reported in the literature<sup>37, 90</sup>. Homogenisation at temperatures greater than 1200°C may result in overheating the steel and for this, the removal of banding above this temperature was considered impractical<sup>90</sup>. Unlike the previous, work this research re-examined band removal through high temperature homogenisation followed by normalisation with a third heat treatment involving furnace cooling after 20 minutes at 1000°C. Widely-spaced traces of bands reappeared (Figure 5-3) indicating that the homogenisation is not complete. In a slow cooling process very little difference in concentration of manganese favours segregation of carbon but the threshold difference has not been established.

The finding above was applied to grade X100 steel produces similar results although its average band spacing is narrower when compared with that of the grade X65 steel. Contrary to the previous claim that banding is not noticeable in steels with carbon content less than 0.1 %<sup>36</sup>, grade X100 is banded although it contains less than 0.1 % carbon but it contains more manganese (1.8 %) than the non-banded steel reported in the literature which contains 0.35 % manganese.

It can be concluded from the above discussion that the key to band removal is reduction of average band spacing and knowing the actual diffusion coefficient of manganese in steels. Homogenization is required because pearlite bands increase the susceptibility of steels to hydrogen-induced cracking<sup>121</sup>.

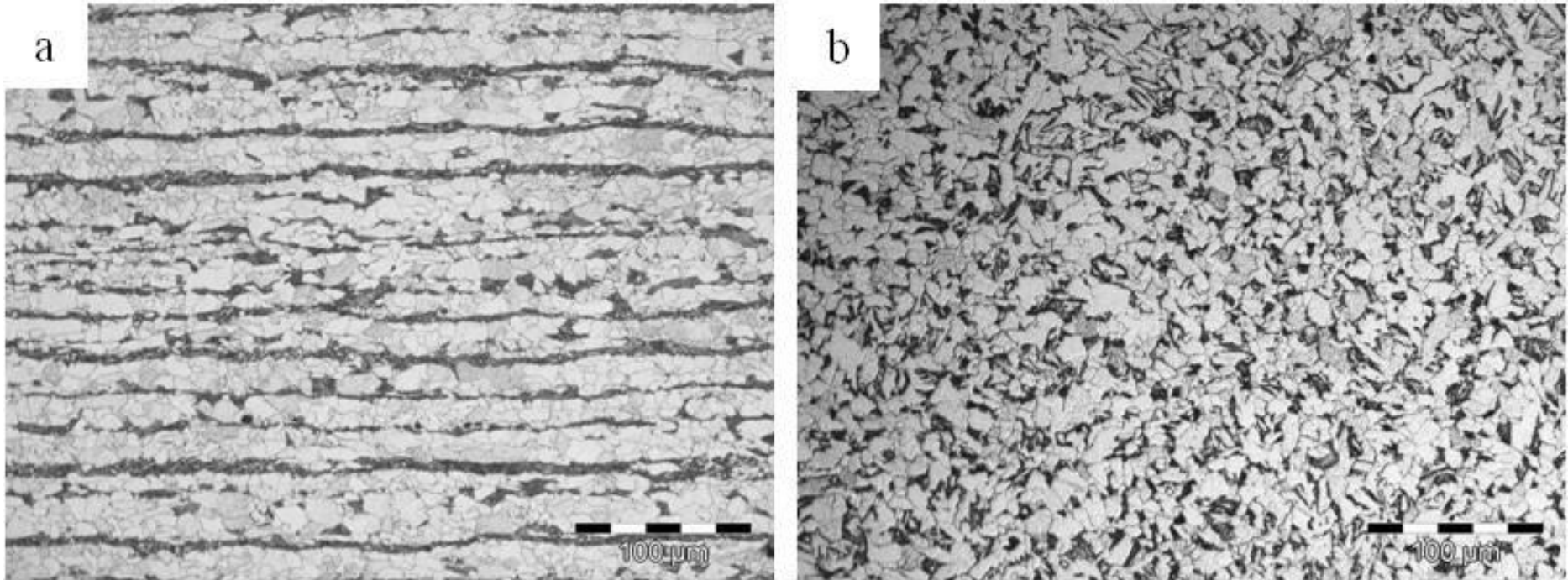
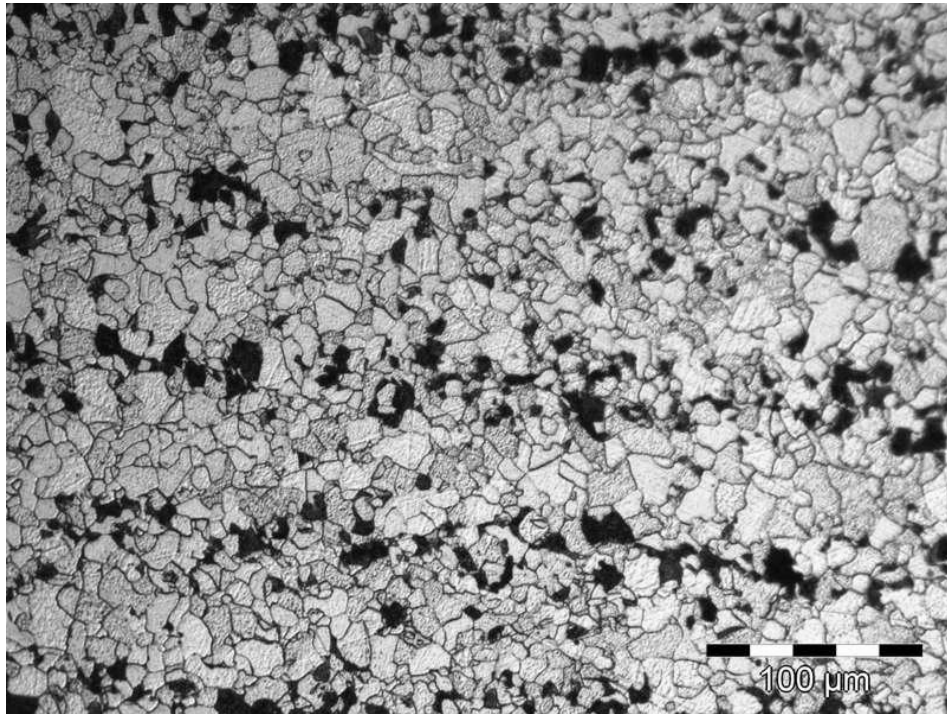


Figure 5-2. (a) Banding in the as-received grade X65 steel (b) was removed by furnace cooling after 5 hours at 1175°C and then air cooled after 20 minute at 950°C



**Figure 5-3. Furnace cooled after 5 hours at 1175°C, then air cooled after 20 minute at 950°C and again furnace cooled after 20 minutes at 1000°C**

### **5.7 Effect of banding on ductility**

Figure 4-36 demonstrates the effect of banding on fracture surface ovality. The ovality is more severe in the as-received material than in the heat treated specimens because the rolling effect has been greatly removed by the annealing. The grains are equiaxed and the carbon distribution is fairly uniform because of air cooling from higher temperatures.

It is pearlite bands that contribute to the ovality but not the segregation of the manganese. The pearlite/ferrite banding creates a layered arrangement of hard and soft regions and during cross-sectional reduction; it is easier to squeeze the softer ferrite bands than the pearlite bands. So, the reduction in area is greater in a direction perpendicular to banding than parallel to it. Therefore, the elimination of the segregation is important to the removal of directionality or isotropy in tensile ductility. Banding causes directionality in tensile ductility. It reduces reduction in area but has little effect on elongation.

## 5.8 Effect of banding on stress corrosion cracking

Figures 4-39 and 4-40 together demonstrate the effect of banding on the propagation of stress corrosion cracking. Banding in the “LT” face induces cracks to grow larger and parallel to it direction in the non banded “CL” face.

The effect of banding and elongated inclusions on subcritical hydrogen-induced cracking is well established<sup>40, 41, 122, 123</sup>. In this study, for the first time the direct effect of banding on high pH SCC is reported; more particularly, the alignment or elongation of the cracks parallel to the direction of the banding. Some cracks due to hydrogen-induced cracking have been shown to be associated with the phase boundary between ferrite and pearlite<sup>41</sup>.

This finding suggests that the longitudinal growth of EAC cracks in seam welded pipe is dominated by microstructural banding rather than hoop stress. Figure 5-4 shows cracks<sup>124</sup> run perpendicular to hoop stress indicating that the crack growth is dominated by microstructure rather than direction of application of the principal stress and it is more likely that the curved surface of the drum is the rolling plane of the welded sheet. Figure 5-5 shows EAC crack morphology in spirally welded pipes.

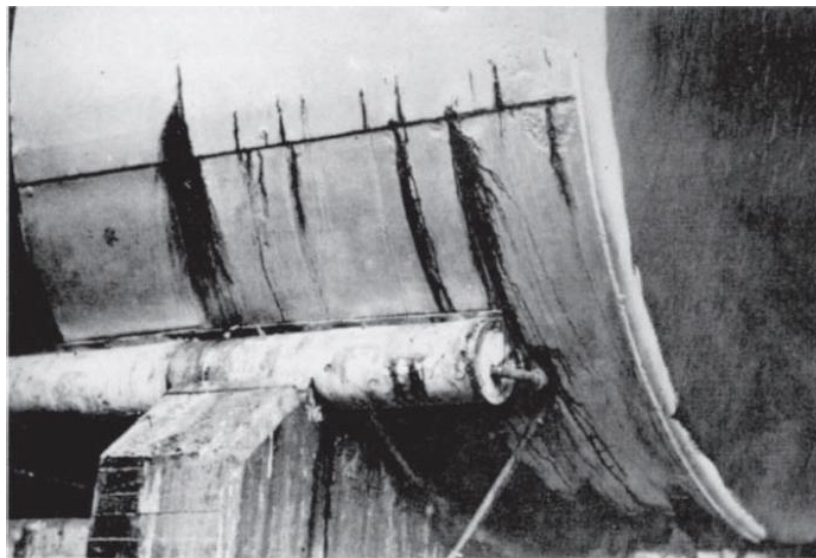
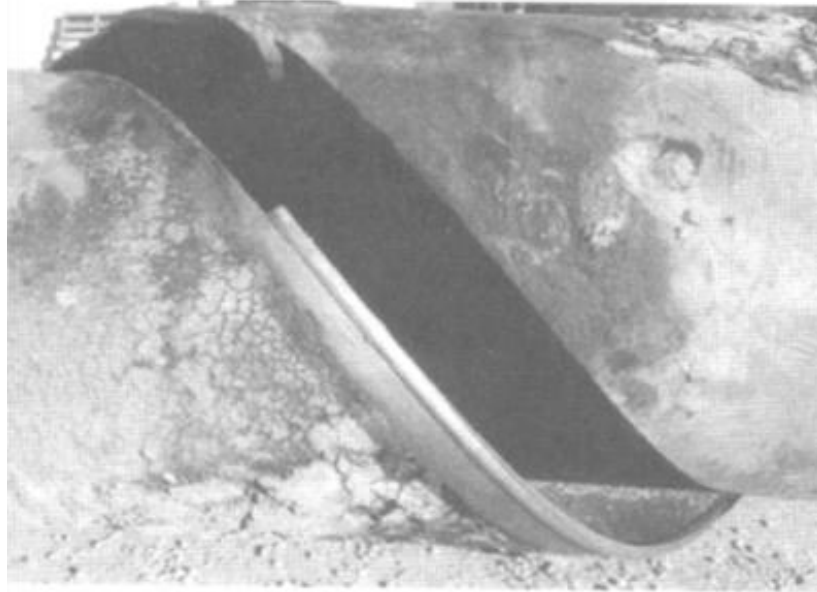


Figure 5-4. Stress corrosion cracks in the shell of a coal gas liquor recirculating tank<sup>124</sup>



**Figure 5-5. Crack morphology in spirally-welded pipe<sup>125</sup>**

How far the crack is away from the spiral welding has not been established from the source at time of compiling this report. The crack is likely to be connected with microstructure. SCC cracks near branch connections have been oriented in a circular pattern concentric with branch connection reinforcement<sup>55</sup>. The growth of these cracks was attributed to the influence of secondary stresses associated with the branch connections. The stresses are sufficiently large to influence the orientation of the cracks.

## Chapter 6 : CONCLUSIONS

1. The as-received microstructure of the grade X100 steel is less susceptible to intergranular (IG) stress corrosion cracking (SCC) when compared with both the simulated heat-affected zone (HAZ) microstructures and the as-received seam weld HAZ microstructures and also less susceptible than the as-received microstructure of the grade X80.
2. Four types of film morphology associated with anodic SCC on the as-received microstructure of the grade X100 were identified at 75°C. The four morphologies are: flat and smooth, flat but textured, nodular and pseudo-cubic. Film structure appears to be associated with a particular mode of failure. The flat film morphologies are associated with IG cracking whereas the nodular and pseudo-cubic morphologies are associated with transgranular cracking (TG). The pseudo-cubic film gives less secondary cracking when compared with both the flat and the nodular films morphologies.
3. Within a potential range of – 500 to – 1100 mV (sce) in the carbonate solution the susceptibility to secondary cracking is divided into two regions. IG and TG regions. The susceptibility to secondary cracking varies with microstructure in the IG region whereas in the TG region, the susceptibility to secondary cracking of the as-received microstructure of the grade X100 and two simulated HAZ microstructures is the same. The two simulated microstructures are the zones of re-crystallization and of grain growth. Hydrogen embrittlement results in little secondary cracks.
4. Slow strain rate tests on the as-received microstructure of the grade X100 at 75°C give a serrated load-extension curve. The serrations at 75°C and a strain rate of  $2 \times 10^{-6}$ /s were removed by air cooling after 30 minutes at 600°C (simulated tempered region of HAZ). This heat treatment increases the susceptibility to secondary cracking at potentials more negative than – 800 mV (sce) when compared with the as-received microstructure. The removal



of the serrations and the increase in susceptibility is due to removal of carbon from solution as a result of the heat treatment.

5. The most susceptible potential to IG SCC varies slightly with microstructure. Comparing the susceptibility of two microstructures, at an applied potential of  $-650$  mV (sce), with the same chemical composition but different phase distribution: pearlite/ferrite and Widmanstätten structure. IG cracks were observed on the former microstructure whereas in the latter TG cracks were found. The IG secondary crack velocity is approximately twice the value of the TG crack velocity. However, at an applied potential of  $-600$  mV (sce), the cracking in both microstructures are IG and the most susceptible microstructure is the Widmanstätten structure. This conclusion reinforces the importance of assessing the susceptibility to IG SCC over a potential range.
6. The best parameter to assess susceptibility to environment-assisted cracking (EAC) is the combination of primary crack velocity and embrittlement index.
7. The result for energy dispersive X-ray analysis (EDX) indicates that the concentration of manganese in pearlite bands is slightly higher than that in ferrite band. Although the difference in concentration of manganese between the two phases is small it is sufficient to cause segregation of carbon during slow cooling. The area analysis gives good average of the concentration of manganese in a band when compared with a spot analysis or a line scan.
8. Furnace cooling after 5 hours at  $1175^{\circ}\text{C}$  eliminated banding in the grade X65 pipeline steel but increased the average grain size. This was refined without the return of banding by air cooling after 20 minutes at  $950^{\circ}\text{C}$ . Thus banding was removed at a low temperature. Banding in a longitudinal section causes SCC cracks to grow larger and parallel to the rolling direction in the plane of the rolling even though the rolling plane is not banded. This conclusion suggests that the longitudinal growth of SCC cracks in seam welded pipes is influenced by microstructural banding.

## FURTHER WORK

Research often raises more questions than answers and from this work a few of the major areas worthy of further study are as follows:

1. Further investigation on the change in cracking mode from IG to TG in the SCC potential region would be of interest. The change in cracking mode is associated with a change in film morphology. The determination of the film properties and the relative composition of siderite and magnetite in the film associated with each mode of cracking may explain the mechanism involved in the change in cracking mode and the role of film composition in the process;
2. The mechanism of the occurrence of serrations, their disappearance as a result of removing carbon from solution and the subsequent increase in susceptibility to secondary cracking deserve further investigation;
3. Compare the performance of the banded and the non-banded microstructure of the X65 after cathodic charging to assess change in susceptibility to hydrogen embrittlement;
4. Determine the threshold difference in concentration of manganese required to cause segregation of carbon during slow cooling;
5. Determine whether the homogenisation of carbon is sufficient to remove directionality in ductility measurement (% RA)

## REFERENCES:

1. Hudson, M. G. Welding of X100 linepipe. PhD thesis, Cranfield University, 2004, p. 4.
2. Parkins, R. N. A review of stress corrosion cracking of high pressure gas pipelines, Corrosion2000, NACE: Houston, 2000; paper number:00363.
3. Asahi, H.; Kushida, T.; Kimura, M.; Fukai, H.; Okano, S., Role of microstructures on stress corrosion cracking of pipeline steels in carbonate-bicarbonate solution. *Corrosion* **1999**, 55, (7), 644-652
4. Charles, E. A.; Parkins, R. N., Generation of stress corrosion cracking environments at pipeline surfaces. *Corrosion* **1995**, 51, (7), 518-527.
5. Parkins, R. N.; Fessler, R. R., Stress corrosion cracking of high-pressure gas transmission pipelines. *Materials in Engineering Applications* **1978**, 1, 80-96.
6. Wang, J. Q.; Atrens, A., SCC initiation for X65 pipeline steel in the high pH carbonate/bicarbonate solution. *Corrosion Science* **2003**, 45, (10), 2199-2217.
7. Jones, D. A., *Principles and prevention of corrosion*. Macmillan: Singapore, 1992; pp. 235-236, 266 and 437.
8. Christman, T. K.; Beavers, J. A., Cause of stress-corrosion cracking in pipe. *Oil and Gas Journal* **1987**, 85, (1), 40-43.
9. Argent, C., MSc Pipeline engineering corrosion module. In Newcastle University: Newcastle upon Tyne, 2004.
10. Brandt, D. A.; Warner, J. C., *Metallurgy Fundamentals*. Goodheart-Willcox: Tinley Park, Ill., 2005; pp.137 and 140.
11. Bhadeshia, H. K. D. H.; Honeycombe, R. W. K., *Steels : microstructure and properties*. 3rd edition; Elsevier: Oxford, 2006; pp. 8-13, 30, 41 and 300.
12. Clark, D. S.; Varney, W. R., *Physical metallurgy for engineers*. 2nd ed.; Van Nostrand: Princeton, N. J., 1962; p. 1.
13. Rollason, E. C., *Metallurgy for Engineers*. 4th ed.; Edward Arnold A division of Hodder & Stoughton: London, 1973; pp. 94-95, 110 and 154.
14. Merriman, A. D., *A concise encyclopaedia of metallurgy*, Macdonald & Evans Ltd: London, 1965; pp. 51 and 57-58.

15. Palmer, A. C.; King, R. A., *Subsea Pipeline Engineering*. PennWell Corporation: Tulsa, Oklahoma, 2004; pp. 27-48, 57, 62-63 and 106-107.
  
16. Obinata, T. In *An introductory review of the effects of steelmaking practice on the development of high strength steels for pipeline*, Steels for line pipe and pipeline fittings, London, 1981; The Metals Society: London, 1981; pp. 185-191.
  
17. Prosser, K., MSc Lecture Notes on Materials and Fabrications. In Newcastle University, UK: 2006.
  
18. Sage, A. M. In *A review of the physical metallurgy of high strength, low alloy line pipe and pipe fitting steels*, Steels for line pipe and pipeline fittings, London, 1981; London, 1981; pp. 39-50.
  
19. Shackelford, J. F., *Introduction to materials science for engineers*. 6th , International ed ed.; Pearson Education International Pearson Education Ltd.: 2005; pp. 74,87,134,138,151,165-166,193-198, 199 and 295.
  
20. Leslie, W. C., *The physical metallurgy of steels*. Hemisphere Publishing Corporation: London, 1981; pp.169 and 172-177.
  
21. Hertzberg, R. W., *Deformation and fracture mechanics of engineering materials*. John Wiley & Sons, Inc: Toronto, 1996; p. 123.
  
22. Tamura, I.; Ouchi, C.; Tanaka, T.; Sekine, H., *Thermomechanical processing of high strength low alloy steels* Butterworths: London, 1988; p. v.
  
23. Hillenbrand, H. G., Niederhoff, K., Amoris, E., Perdix, C., Streisselberger, A., Zeislmaier, U.; , Development of linepipe in grades up to X100. *Europipe technical literature* **1999**.
  
24. Denys, R., *Development of Large-Diameter Pipe in Grade X100 (State-Of-The-Art Report from the Manufacturer's Point of View)* Elsevier Science B. V.: 2000; Vol. 1, p 469 - 482.
  
25. Ishikawa, N.; Endo, S.; Muraoka, R.; Kondo, J. In *Design concepts and mass production of high strength UOE line pipes*, Rio de Janeiro, Brazil, 2001; American Society of Mechanical Engineers: Rio de Janeiro, 2001; pp 63-70.
  
26. Tamehiro, H.; Terada, Y. *Metallurgical Design of X100 Line Pipe*; Nippon Steel Corporation: August, 1994.
  
27. Pickering, F. B., *Micro Alloying 75*. Union Carbide Corporation: Washington, 1977; p. 3.

28. Hillenbrand, H.-G.; Gras, M.; Kalwa, C. In *Development and production of high strength pipeline steels*, Orlando, FL, United states, 2001; Minerals, Metals and Materials Society: Orlando, FL, United states, 2001; pp. 543-569.
29. Race, J.; Peet, S., Assessment of corrosion in low toughness pipe material. In *Corrosion2002*, NACE: Houston, 2002; paper No. 02088.
30. Institute, A. P., Specification for Line Pipe. In 2004; Vol. API Specification 5L, p. 9.
31. *Metals handbook*. 9 ed.; 1985; Vol. 9, p. 2.
32. Krauss, G., Solidification, Segregation, and Banding in Carbon and Alloy Steels. *Metallurgical and Materials Transactions B: Process Metallurgy and Materials Processing Science* **2003**, 34, (6), 781-792.
33. Thompson, S. W.; Howell, P. R., Factors influencing ferrite/pearlite banding and origin of large pearlite nodules in a hypoeutectoid plate steel. *Materials Science and Technology* **1992**, 8, (9), 777-784.
34. Verhoeven, J. D., Review of microsegregation induced banding phenomena in steels. *Journal of Materials Engineering and Performance* **2000**, 9, (3), 286-296.
35. Lyman, T., *Metals handbook - Metallography, structures and phase diagrams*. 8 ed.; American Society of Metals: Ohio, 1973; Vol. 8, p. 93.
36. Samuels, L. E., *Optical microscopy of carbon steels*. American Society for Metals: Ohio, 1980; pp. 127-131.
37. Grange, R. A., Effect of Microstructural Banding in Steel. *Metallurgical and Materials Transactions A: Physical Metallurgy and Materials Science* **1971**, 2, 417-26.
38. Spitzig, W. A., Effect of sulfide inclusion morphology and pearlite banding on anisotropy of mechanical properties in normalised C-Mn steels. *Metallurgical Transactions A (Physical Metallurgy and Materials Science)* **1983**, 14A, (2), 271-283.
39. Wilms, G. R., Note on hardness changes in tempering mild steel. *Journal of the Australian Institute of Metals* **1975**, 20, (3), 168-169.
40. Elboudjaini, M.; Sastri, V. S.; Perumareddi, J. R., Studies on Inhibition of Hydrogen-Induced Cracking of Linepipe steels. *Corrosion* **2006**, 62, (1).
41. Hardie, D.; Charles, E. A.; Lopez, A. H., Hydrogen embrittlement of high strength pipeline steels. *Corrosion Science* **2006**, 48, 4378-4385.

42. Hardie, D.; Murray, T. I. In *The effect of hydrogen upon the tensile ductility of high strength maraging steel*, Mechanism of environment sensitive cracking of materials, University of Surrey, Guildford, 1977; Swann, P. R.; Ford, F. P.; Westwood, A. R. C., Eds. The Metals Society: University of Surrey, Guildford, 1977; pp. 459-470.
43. Chen, J. The effects of specimen geometry on the susceptibility to stress corrosion cracking (SCC) of steels. PhD, Newcastle University, Newcastle upon Tyne, 2002, pp. 9, 12-19 and 84
44. Parkins, R. N., Stress-corrosion cracking. *Metallurgical Reviews* **1964**, 9, (35), 201-260.
45. Zhou, S. Environment sensitive fracture of ferritic steels in aqueous  $\text{CO}_2/\text{HCO}_3^-/\text{CO}_3^{2-}$  solutions. PhD, University of Newcastle upon Tyne, Newcastle upon Tyne, 1991, p. 3.
46. Parkins, R. N., *Corrosion Processes*. Applied Science Publishers: London, 1982; p. 271.
47. Kane, R. D., *Environmentally assisted cracking: predictive methods for risk assessment and evaluation of materials, equipment and structures*. ASTM: Orlando, 2000; pp. 289-290.
48. Jones, R. H.; Ricker, R. E., Mechanism of stress-corrosion cracking. In *Stress-corrosion cracking, materials performance and evaluation*, Jones, R. H., Ed. ASM International: 1992; pp. 1-40.
49. Davies, D. H.; Burstein, G. T., Effect of bicarbonate on the corrosion and passivation of iron. *Corrosion* **1980**, 36, (8), 416-422.
50. Parkins, R. N.; Zhou, S., The stress corrosion cracking of C-Mn steel in  $\text{CO}_2\text{-HCO}_3^-\text{-CO}_3^{2-}$  solutions. I: stress corrosion data. *Corrosion Science* **1997**, 39, (1), 159-173.
51. Turnbull, A., Modelling of environment assisted cracking. *Corrosion Science* **1993**, 34, (6), 921-960.
52. Staehle, R. W., Lifetime prediction of materials in environments. In *Uhlig's Corrosion Handbook* Revie, R. W., Ed. John Wiley & Sons London, 2000; p. 32.
53. Fang, B. Y.; Atrens, A.; Wang, J. Q.; Han, E. H.; Zhu, Z. Y.; Ke, W., Review of stress corrosion cracking of pipeline steels in "low" and "high" pH solutions. *Journal of Materials Science* **2003**, 38, (1), 127-132.
54. Wenk, R. L. *5th Symp. on line pipe research, Catalog No. L30174*; Arlington, VA, 1974; p. T-1.

55. Parkins, R. N. *Overview of intergranular stress corrosion cracking research activities*; Report No. PR-232-9401; Arlington, 1994; pp. 6, 8 and 11.
56. Revie, R. W., *Ullrich's corrosion handbook*. 2 ed.; John Wileys & Sons Inc.: 2000; pp. 201 and 1110 to 1111.
57. Jones, R. H., *Stress corrosion cracking, materials performance and evaluation*. ASM International: 1992; pp. 1-40 and 363-415.
58. Sedriks, A. J., *Stress Corrosion Cracking Test Methods*. National Association of Corrosion Engineers: Houston, 1990; pp. 3-8 and 17.
59. Sprowls, D. O., Evaluation of stress-corrosion cracking. In *Stress corrosion cracking, materials performance and evaluation*. Jones, R. H., Ed. ASM International: 1992; pp. 363-415.
60. Kane, R. D., Testing for environmentally assisted cracking. In *Ullrich's corrosion handbook*, 2 ed.; Revie, R. W., Ed. John Wiley and Sons: 2000; pp. 1109-1128.
61. ASTM-E-399, Standard test method for plane-strain fracture toughness of metallic materials. In ASTM: Philadelphia, PA, 1972.
62. Ugiansky, G. M.; Payer, J. H., *Stress Corrosion Cracking-The Slow Strain-Rate Technique*. ASTM: Philadelphia, 1979; pp. 5-24.
63. Ackland, B. G.; Cherry, B. W., Stress corrosion cracking in the weld metal, heat affected zone and base metal of a line pipe weld - Awra contract 65. *Australian Welding Research* **1982**, 11, 48-54.
64. Belhimer, E. Stress corrosion cracking of pipeline steels and pure iron in a sodium carbonate-sodium bicarbonate solution. PhD thesis, University of Newcastle upon Tyne, 1987, p. 40.
65. Craig Jr., H. L., *Stress Corrosion-New Approaches*. ASTM: Philadelphia, 1976; p 91.
66. Parkins, R. N., Stress corrosion spectrum. *British Corrosion Journal* **1972**, 7, 15-28.
67. Uhlig, H. H., In *Physical metallurgy of stress corrosion fracture* Rhodin, T. N., Ed. Interscience: New York, 1959; p. 1.
68. Koh, S. U.; Jung, H. G.; Kang, K. B.; Park, G. T.; Kim, K. Y., Effect of microstructure on hydrogen-induced cracking of linepipe steels. *Corrosion* **2008**, 64, (7), 574-585.

69. Parkins, R. N., Mechanistic aspects of intergranular stress corrosion cracking of ferritic steels. *Corrosion* **1996**, 52, (5), 363-374.
70. Christman, T. K. *Evaluation of stress-corrosion cracking resistance of newly developed grade X70 and X80 line pipe steels*; NG-18 Report No. 173; Pipeline Research Committee of the American Gas Association: Columbus, Ohio, 1988.
71. Li, G.; Zhang, G.; Zhou, J.; Huang, C.; Yang, W., Characteristics and Mechanism of High pH Stress Corrosion Cracking of Pipeline Steel X70. *Key Engineering Materials* **2007**, 353-358, 219-222.
72. Stikma, J.; Bradford, S. A., Stress corrosion cracking of dual-phase steel in carbonate / bicarbonate solutions. *Corrosion* **1985**, 41, (8), 446-450.
73. Wang, Z. F.; Atrens, A., Initiation of stress corrosion cracking for pipeline steels in a carbonate-bicarbonate solution. *Metallurgical and Materials Transactions A: Physical Metallurgy and Materials Science* **1996**, 27 A, (9), 2686-2691.
74. Rebak, R. B.; Xia, Z.; Safruddin, R.; Szklarska-Smialowska, Z., Effect of solution composition and electrochemical potential on stress corrosion cracking of X-52 pipeline steel. *Corrosion* **1996**, 52, (5), 396-405.
75. Mitsui, H.; Takahashi, R.; Asano, H.; Taniguchi, N.; Yui, M., Susceptibility to Stress Corrosion Cracking for Low-Carbon Steel Welds in Carbonate-Bicarbonate Solution. *Corrosion* **2008**, 64, (12), 939-948
76. Jackson, V. The effect of notching and specimen orientation on the susceptibility to hydrogen embrittlement of X80 and X100 pipeline steels. MSc, Newcastle University, 2003, p. 23.
77. Vander Voort, G. F., *Metallography principles and practice*. McGraw-Hill Book Company: New York, 1984; pp. 350-353 and 450-451
78. ASTM, Standard Test Methods for Determining Average Grain Size, ASTM International: 2004.
79. Mathers, G., Hardness testing part 1. *Connect, the magazine of TWI* January/February, 2005, pp. 4-5.
80. Sutcliffe, J. M.; Fessler, R. R.; Boyd, W. K.; Parkins, R. N., Stress corrosion cracking of carbon steel in carbonate solution. *Corrosion* **1972**, 28, (8), 313-320.
81. Parkins, R. N., Predictive approaches to stress corrosion cracking failure. *Corrosion Science* **1980**, 20, (2), 147-166.



82. Pilkey, A. K.; Lambert, S. B.; Plumtree, A., Stress corrosion cracking of X-60 line pipe steel in a carbonate-bicarbonate solution. *Corrosion* **1995**, 51, (2), 91-96.
83. Staehle, R. W.; Hochmann, J.; McCright, R. D.; Slater, J. E., *Stress Corrosion Cracking and Hydrogen Embrittlement of Iron Base Alloys*. NACE: 1977; Vol. NACE-5, pp. 601-624.
84. Henthorne, M.; Parkins, R. N., Some aspects of the influence of structure upon stress-corrosion cracking and grain boundary corrosion in mild steels. *British Corrosion Journal* **1967**, 2, 186-192.
85. Parkins, R. N.; Slattery, P. W.; Poulson, B. S., The Effect of Alloying Additions to Ferritic Steels upon Stress Corrosion Cracking Resistance. *Corrosion* **1981**, 37, (11), 650-664.
86. ASTM, Standard Reference Test Method for Making Potentiostatic and Potensiodynamic Anodic Polarisation Measurement; ASTM International: 2004.
87. Lyman, T., *Metals handbook*. The American Society for Metals: 1948; p. 730.
88. El-yazgi, A. A. The effect of hydrogen on the mechanical behaviour of duplex stainless steel. PhD, Newcastle University, Newcastle upon Tyne, 1995, p. 110.
89. Desforges, C. D.; Duckworth, W. E.; Ryan, T. F. J. N., *Manganese in Ferrous Metallurgy*. Manganese Centre: Norwich, Gt. Britain, 1976; p. 8.
90. Lavender, J. D.; Jones, F. W., Investigation on banding. *Journal of the Iron and Steel Institute* **1949**, 163, (Part 1), 14-17.
91. Wells, C.; Mehl, R. F., Rate of diffusion of manganese in gamma iron in low-carbon and high-carbon manganese steels. *American Institute of Mining and Metallurgical Engineers -- Transactions -- Iron and Steel Division* **1941**, 145, 315-327.
92. ASTM, Standard Practice for Slow Strain Rate Testing to Evaluate the Susceptibility of Metallic Materials to Environmentally Assisted Cracking. *G129 - 00*, ASTM: Philadelphia, 2006.
93. Dieter, G. E., *Mechanical Metallurgy*. SI metric Edition ed.; McGraw-Hill Book Company: London, 1988; pp. 280 and 202.
94. Chescoe, D.; Goodhew, P. J., *The operation of transmission and scanning electron microscopes*. Oxford University Press: Oxford, 1990; p. 2.

95. Hillenbrand, H. G.; Schwaab, P., Quantitative determination of the microstructure of high strength structural steels for correlation with their mechanical properties. *Materials Science and Engineering* **1987**, 94, 71-78.
96. Tucker, M. E., *Techniques in sedimentology*. Blackwell Scientific Publications: Oxford, 1988; pp. 191-228.
97. Dudgeon, B. A. Hydrogeochemistry of seepage entering deep tunnels in crystalline rock: Cruachan powder station, Scotland. PhD, Newcastle University, Newcastle upon Tyne, 2005, pp. 73-73.
98. Cullity, B. D.; Stock, S. R., *Elements of X-ray diffraction*. Prentice Hall: Upper Saddle River, New Jersey, 2001; p. 95.
99. CPDS, Joint Committee on Powder Diffraction Standards, 1994.
100. Holdstock, R. The Susceptibility of X100 Fine-Grained High-Strength Pipeline Seamweld to Hydrogen Embrittlement. MSc Thesis, Newcastle University, 2003.
101. Al-Azri, H. Investigation of the effect of heat treatment on high strength steel X65, X80 and X100. MSc, Newcastle University, Newcastle upon Tyne, 2008.
102. Ikewete, C. I. Effect of heat treatment on pipeline steel microstructure. MSc, Newcastle University, Newcastle upon Tyne, 2007.
103. Parkins, R. N.; Zhou, S., The stress corrosion cracking of C-Mn steel in CO<sub>2</sub>-HCO<sub>3</sub><sup>-</sup>-CO<sub>3</sub><sup>2-</sup> solutions. II: Electrochemical and other data. *Corrosion Science* **1997**, 39, (1), 175-191.
104. Anozie, E. O. The susceptibility of high grade pipeline steel, X100, to stress corrosion cracking in nitrate environment. MSc, Newcastle University, Newcastle upon Tyne, 2010.
105. Parkins, R. N.; Markworth, A. J.; Holbrook, J. H.; Fessler, R. R., Hydrogen gas evolution from cathodically protected surfaces. *Corrosion* **1985**, 41, (7), 389-397.
106. Parkins, R. N.; O'Dell, C. S.; Fessler, R. R., Factors affecting the potential of galvanostatically polarized pipeline steel in relation to SCC in CO<sub>3</sub><sup>2-</sup>-HCO<sub>3</sub><sup>-</sup> solutions. *Corrosion Science* **1984**, 24, (4), 343-374.
107. Cottrell, A. H., *An introduction to metallurgy*. Edward Arnold Ltd.: London, 1967; p. 392.
108. Park, G. T.; Koh, S. U.; Jung, H. G.; Kim, K. Y., Effect of microstructure on the hydrogen trapping efficiency and hydrogen induced cracking of linepipe steel. *Corrosion Science* **2008**, 50, (7), 1865-1871.

109. Pussegoda, L. N.; Tyson, W. R. *Relationship between microstructure and hydrogen susceptibility of some low carbon steels*, Moran, WY, USA, 1981; Metall Soc of AIME: Moran, WY, USA, 1981; pp. 349-360.
110. Sutcliffe, J. M.; Fessler, R. R.; Boyd, W. K.; Parkins, R. N., Stress corrosion cracking of carbon steel in carbonate solutions. *Corrosion* **1972**, 28, (8), 313-320.
111. Poulson, B., The fractography of the stress corrosion cracking in carbon steels. *Corrosion Science* **1975**, 15, 469-477.
112. Parkins, R. N.; Belhimer, E.; Blanchard, W. K., Stress corrosion cracking characteristics of a range of pipeline steels in carbonate-bicarbonate solution. *Corrosion* **1993**, 49, (12), 951-966.
113. Danielson, M. J.; Jones, R. H.; Dusek, P. In *Effect of microstructure and microchemistry on the SCC behaviour of archival and modern pipeline steels in a high pH environment*, Corrosion2001, NACE: Houston, 2001; paper No. 01211.
114. Danielson, M. J.; Jones, R. H.; Krist, K., Effect of microstructure and microchemistry on the SCC behaviour of pipeline steels in a high pH environment In *Corrosion2000*, NACE: Houston, 2000; paper No. 00359.
115. Lu, B. T.; Luo, J. L., Relationship between yield strength and near-neutral pH stress corrosion cracking resistance of pipeline steels - An effect of microstructure. *Corrosion* **2006**, 62, (2), 129-140.
116. Parkins, R. N., Stress-corrosion cracking of mild steels in nitrate solution. *Iron and Steel Institute -- Journal* **1952**, 172, (Part 2), 149-162.
117. Barsanti, L.; Cabrini, M.; Pastore, T.; Spinelli, C. In *Effect of microstructure on the hydrogen-embrittlement behaviour of HSLA steels under cathodic protection*, Environment-induced cracking of metals, Alberta, 2004; Shipilov, S. A.; Jones, R. H.; Olive, J.-M.; Rebak, R. B., Eds. Elsevier: Alberta, 2004; pp. 279-289.
118. Thompson, A. W.; Bernstein, I. M. *Microstructure and hydrogen embrittlement*, Moran, WY, USA, 1981; Metall Soc of AIME: Moran, WY, USA, 1981; pp 291-308.
119. Kirkaldy, J. S.; von Destinon-Forstmann, J.; Brigham, R. J., Simulation of banding in steels. *Canadian Metallurgical Quarterly* **1962**, 1, 59-81.
120. Wang, J. Q.; Atrens, A.; Cousens, D. R.; Nockolds, C.; Bulcock, S., Boundary characterization of X65 pipeline steel using analytical electron microscopy. *Journal of Materials Science* **1999**, 34, (8), 1711-1719.
121. GroBterlinden, R.; Kawalla, R.; Lotter, U.; Pircher, H., Formation of pearlitic banded structures in ferritic-pearlite steels. *Steel Research*. **1992**, 63, 331-36.

122. Pollock, W. J.; Ryan, N. E.; Nankivell, J. F., Relationship between banding and susceptibility to environment-assisted cracking in a quenched and tempered low alloy steel. *Corrosion Science* **1982**, 22, (3), 215-229.

123. Skarra, R. M. Susceptibility to hydrogen embrittlement of pipeline steels. MSc, Newcastle University, Newcastle upon Tyne, 2009.

124. Parkins, R. N.; Usher, R., The stress-corrosion cracking of mild steel in coal gas liquors. *Journal of Applied Chemistry* **1959**, 9, pp. 445-456.

125. Cottis, R. A.; Graham, M. J.; Lindsay, R.; Lyon, S. B.; Richardson, J. A.; Scantlebury, J. D.; Stott, F. H., *Shreir's Corrosion*. fourth ed.; Elsevier: Oxford, 2010; Vol. 2, pp. 925-926.